

Search for the Standard Model Higgs boson decaying
to a Tau lepton pair in proton-proton collisions using
the CMS detector at the LHC

*A thesis submitted for the degree of
DOCTOR OF PHILOSOPHY (Science)*

in

Physics (Experiment)

by

Atanu Modak

Department of Physics

UNIVERSITY OF CALCUTTA

May, 2016

Title: *Search for the Standard Model Higgs boson decaying to a Tau lepton pair in proton-proton collisions using the CMS detector at the LHC*

Abstract

The Standard Model (SM) of particle physics describes matter constituents and their interactions and has been extensively verified by several collider and non-collider experiments with great success. The only missing piece predicted in the SM was the Higgs boson which provides mass to elementary particles. Recently at the Large Hadron Collider (LHC) at CERN, a SM-like Higgs boson has been discovered at $125 \text{ GeV}/c^2$ by the Compact Muon Solenoid (CMS) and A Toroidal LHC ApparatuS (ATLAS) experiments in the bosonic $H \rightarrow \gamma\gamma$ and $H \rightarrow ZZ$ decay modes. This thesis presents a search for the SM Higgs boson produced in association with a W boson in the $WH \rightarrow \mu\tau_h\tau_h$ and $WH \rightarrow \mu\mu\tau_h$ channels, where in the first channel both the τ leptons from the fermionic $H \rightarrow \tau\tau$ mode decay hadronically (τ_h) while in the second channel one of the τ leptons decays to a muon (μ). Both the channels are dominated by background events where several objects in the final state may be mis-identified. A sophisticated, data-driven background estimation technique has been developed for the analysis. The results were obtained using data collected by the CMS detector which corresponds to an integrated luminosity of 5, 19.5 and 2.1 fb^{-1} at $\sqrt{s} = 7, 8$ and 13 TeV respectively. No excess in event yield has been observed over the predicted background and a confidence limit is set on the SM Higgs cross section. The observed limit is compatible both with SM Higgs and background-only (no Higgs) hypotheses. More data is needed to improve sensitivity of the associated production process, as WH production cross section at the LHC is almost an order of magnitude lower than the dominant Gluon-Gluon production at $125 \text{ GeV}/c^2$. In addition to performing analysis of current data it is also equally important to prepare the detector for future LHC running. The LHC is scheduled for a major luminosity upgrade, known as High Luminosity LHC or HL-LHC, during 2022 and is expected to deliver an instantaneous luminosity of $5 \times 10^{34} \text{ cm}^{-2} \text{ s}^{-1}$ which is ~ 5 times higher than the current value. This upgrade would increase the LHC mass reach by 20-30 % and enable us to measure the Higgs self-coupling, probe its tensor structure, and also look for rare and Beyond SM processes. In this context, a Level-1 trigger algorithm for electrons has been designed including the tracker information to counter the many-fold increase in event rate to improve the selectivity of the trigger and maintain physics performance similar to the present level. The present CMS detector does not process tracker information at Level-1. A Principal Component Analysis (PCA) based track fitter has been developed to reconstruct tracks at Level-1 with high efficiency which is expected to perform within the Level-1 latency required by HL-LHC. An emulation of the algorithm is also performed using integer based fixed point representation which will be implemented on the proposed FPGA based hardware.

To
My Parents

Acknowledgements

It has been a tremendous ride and I am extremely thankful to my supervisors, Subir da and Suchandra di, for their open hearted support, wisdom and guidance. I surely could not have wished for any better supervisors to work under. Their infectious enthusiasm and friendly attitude will continue to inspire me all along. I am certainly going to miss working with them.

I would like to thank Sunanda da for his guidance and the opportunity he provided me to work in Saha-Kolkata CMS group. I still remember the chat over skype we had when I first approached him to join the group. He will always remain as an inspiration to me. I am grateful to Satyaki da for all those interactions and discussions to better understand the physics and educate myself. I sincerely thank Manoj da and Sukalyan da for their help and support during my tenure. I express my gratitude to Prof. Amit Ghosh, my Post M.Sc. project advisor, for coaxing me to join the CMS group. I am hugely indebted to my teachers at IIT Kanpur, Physics Department, especially Prof. Sudeep Bhattacharya and Prof Kaushik Bhattacharjee. I sincerely acknowledge my teachers at RKM Narendrapur for helping me instilling a strong sense of discipline while pursuing academic excellence. Finally, I am hugely grateful to all my primary and high school teachers, who have gone out of their way in guiding me, some of them have even gave me additional mentoring after school hours, and motivated me to pursue a career in academics. I was fortunate to have some great teachers like Deb-babu, Satyen da, Bhondal da in my early days of education.

Working in an active collaborative project, my heartfelt acknowledgement to the entire community of the CMS experiment. There are many people from the collaboration who have directly or indirectly influenced my work. I would like to especially thank Adrian, Giuseppe, Anders, Emmanuelle, Lorian, Fabrizio, Sebastien, Giacinto, Armin, Rosma and many others. I have learned a lot from the experts at CERN mainly through group meetings, many of whom I have never met personally but only know by their voice.

I am sincerely grateful to many people who have supported my education during my days of financial struggle. I would not have made this far without your kind support. My doctoral fellowship was funded by Department of Atomic Energy, India and I am extremely thankful for this opportunity. I will remain hugely indebted to INFN Pisa and INFN Bari for letting me use their computing facility, without which I could never have completed this thesis.

Even though I lacked in my socializing skills, I was fortunate enough to be gifted by amazing friends. I would like to thank my fellow batch mates - Kalyanmoy, SPA, Jayati, Prithwish, Sudip, Tapas, Swagata, Debarati and my school friends, for the sweet memories we made. I thankfully acknowledge the support I received from my juniors - Suvankar, Kuntal, Ashim, Sourav, Shamik, Arnab and Saswati. Thank you for all

the fun we had while working in 4102. I am grateful to my loving seniors - Nilu da, Sreemoyee di, Najmul da, Mahotsab da, Ajanta di and Saptaparni di. Finally I would like to thank my closest buddies, Parikshit and Rajani for their sheer presence in my life. You two have always inspired me to be a better person.

I would like to acknowledge my family - my parents, sister, brother-in law, my cute niece and my in-laws for being my ultimate support system. A mere 'thank you' will grossly undervalue my parents' strive to value my education above everything else. Finally, I thank my beautiful wife for her unconditional love and support. You are the best thing that could have happened to my life.

*Atanu Modak
Kolkata, India.*

Abstract

The Standard Model (SM) of particle physics describes matter constituents and their interactions and has been extensively verified by several collider and non-collider experiments with great success. The only missing piece predicted in the SM was the Higgs boson which provides mass to elementary particles. Recently at the Large Hadron Collider (LHC) at CERN, a SM-like Higgs boson has been discovered at $125 \text{ GeV}/c^2$ by the Compact Muon Solenoid (CMS) and A Toroidal LHC ApparatuS (ATLAS) experiments in the bosonic $H \rightarrow \gamma\gamma$ and $H \rightarrow ZZ$ decay modes. This thesis presents a search for the SM Higgs boson produced in association with a W boson in the $WH \rightarrow \mu\tau_h\tau_h$ and $WH \rightarrow \mu\mu\tau_h$ channels, where in the first channel both the τ leptons from the fermionic $H \rightarrow \tau\tau$ mode decay hadronically (τ_h) while in the second channel one of the τ leptons decays to a muon (μ). Both the channels are dominated by background events where several objects in the final state may be mis-identified. A sophisticated, data-driven background estimation technique has been developed for the analysis. The results were obtained using data collected by the CMS detector which corresponds to an integrated luminosity of 5, 19.5 and 2.1 fb^{-1} at $\sqrt{s} = 7, 8$ and 13 TeV respectively. No excess in event yield has been observed over the predicted background and a confidence limit is set on the SM Higgs cross section. The observed limit is compatible both with SM Higgs and background-only (no Higgs) hypotheses. More data is needed to improve sensitivity of the associated production process, as WH production cross section at the LHC is almost an order of magnitude lower than the dominant Gluon-Gluon production at $125 \text{ GeV}/c^2$. In addition to performing analysis of current data it is also equally important to prepare the detector for future LHC running. The LHC is scheduled for a major luminosity upgrade, known as High Luminosity LHC or HL-LHC, during 2022 and is expected to deliver an instantaneous luminosity of $5 \times 10^{34} \text{ cm}^{-2}\text{s}^{-1}$ which is ~ 5 times higher than the current value. This upgrade would increase the LHC mass reach by 20-30 % and enable us to measure the Higgs self-coupling, probe its tensor structure, and also look for rare and Beyond SM processes. In this context, a Level-1 trigger algorithm for electrons has been designed including the tracker information to counter the many-fold increase in event rate to improve the selectivity of the trigger and maintain physics performance similar to the present level. The present CMS detector does not process tracker information at Level-1. A Principal Component Analysis (PCA) based track fitter has been developed to reconstruct tracks at Level-1 with high efficiency which is expected to perform within the Level-1 latency required by HL-LHC. An emulation of the algorithm is also performed using integer based fixed point representation which will be implemented on the proposed FPGA based hardware.

List of Publications

1. “*Evidence for the 125 GeV Higgs boson decaying to a pair of τ leptons*”, **CMS Collaboration**, JHEP 1405 (2014) 104.
2. “*Evidence for the direct decay of the 125 GeV Higgs boson to fermions*”, **CMS Collaboration**, Nature Phys. 10 (2014).
3. “*Technical Proposal for the Phase-II Upgrade of the CMS*”, **CMS Collaboration**, CERN-LHCC-2015-10.

CMS Public and Internal Notes:

- “Search for SM Higgs boson in the $W^\pm H^0$ production in pp collisions at the CMS experiment, with $\tau^+\tau^-$ Higgs final state where τ decays hadronically” - CMS Analysis Note, CMS AN-2012-219 (internal).
- “Search for the standard model Higgs boson decaying to tau pairs produced in association with a W or Z boson with the CMS experiment in pp collisions at $\sqrt{s} = 7$ and 8 TeV” - CMS Physics Analysis Summary, CMS PAS HIG-2012-053 (public).
- “Search for a Standard Model Higgs boson decaying to tau pairs produced in association with a W or Z boson” - CMS Analysis Note, CMS AN-2013-187 (internal).
- “Search for the Standard-Model Higgs boson decaying to tau pairs in proton-proton collisions at $\sqrt{s} = 7$ and 8 TeV” - CMS Physics Analysis Summary, CMS PAS HIG-2013-004 (public).
- “Search for the standard model Higgs boson decaying to a pair of hadronically decaying tau leptons produced in association with a W boson” - CMS Analysis Note, CMS AN-2013-234 (internal).
- “Fake rate estimation in WH events with Higgs boson decaying into a di-tau pair at 13 TeV” - CMS Analysis Note, CMS AN-2016-046 (internal).
- “Use of tracking in the CMS L1 trigger for the phase-2 upgrade” - CMS Detector Note, CMS DN-2014-002 (internal).

Contents

1	Introduction	1
1.1	Context	1
1.2	Thesis Content	3
2	The Standard Model of Particle Physics	7
2.1	Introduction	7
2.2	The Gauge Symmetry Group of the Standard Model	8
2.2.1	$U(1)$ QED Theory	9
2.2.2	$SU(3)$ QCD Theory	10
2.2.3	$SU(2)_L \otimes U(1)_Y$ Electro-Weak Theory	12
2.3	Spontaneous Symmetry Breaking	14
2.4	The Higgs Mechanism	16
2.5	Higgs Production at the Large Hadron Collider	19
3	The CMS Detector at the LHC	23
3.1	The Large Hadron Collider	23
3.2	The CMS Detector	27
3.2.1	The CMS Magnet	28
3.2.2	Tracking Detector	29
3.2.3	Electromagnetic Calorimeter	32
3.2.4	Hadron Calorimeter	34
3.2.5	Muon Detector	37
3.2.6	Trigger System	38
4	Search for the Standard Model Higgs boson	44
4.1	Introduction	44
4.2	$WH \rightarrow \mu\tau_h\tau_h$ Analysis	46
4.2.1	Data and Monte Carlo Samples	46
4.2.2	Pile-Up Reweighting	51

4.2.3	Baseline Selection	52
4.2.4	Background Estimation	65
4.2.5	Systematics	79
4.2.6	Results and Limits	84
4.3	WH $\rightarrow\mu\mu\tau_h$ Analysis	86
4.3.1	Baseline Selection	87
4.3.2	Background Estimation	88
4.3.3	Systematics	95
4.3.4	Results and Limits	97
5	Level 1 Track Trigger with Electron	101
5.1	Introduction	101
5.2	Trigger Primitive	103
5.2.1	Stub	104
5.2.2	Tracklet	105
5.3	Tracks at Level 1	106
5.4	Electron Triggers	110
5.4.1	Calorimeter Electrons	110
5.4.2	L1EGamma object to Stub Matching	111
5.4.3	Isolation Requirement on L1EGamma object to Stub Matching	117
5.4.4	Efficiency and Rate Reduction with L1EGamma object to Stub Matching	117
5.4.5	L1EGamma object to Track Matching	119
5.4.6	Isolation Requirement on L1EGamma object to Track Matching	121
5.4.7	Efficiency and Rate Reduction with Electron Track Matching	127
5.5	Alternative Scenario	128
5.5.1	Performance with Tilted Tracker Design	129
5.5.2	Performance with 5 Layer Outer Tracker	131
6	Associative Memory based Tracking at Level 1 Trigger	136
6.1	Introduction	136
6.2	Associative Memory based Pattern Recognition	138
6.3	Principal Component Analysis Track Fitter	141
6.3.1	Integer based algorithm	145
7	Conclusion and Scope	149

Introduction

1.1 Context

The quest to understand the nature and naturally occurring phenomena leads to the development of the field of Physics which aims at describing the nature in terms of visible matter content of the universe and how they interact with each other. There are four different basic forces in nature: strong, electromagnetic, weak and gravitational, ordered according to their relative strength. The Standard Model (SM) [1-3] of particle physics deals with the fundamental particles in nature and their interactions. It describes the strong, weak and electromagnetic forces. The gravitational interaction cannot be described by the model. Figure 1.1 shows the elementary particles which are of two kinds, lepton and quark and the gauge bosons which act as the mediator of forces. The SM of particle physics is arguably the most rigorously tested theory ever. In the past decades, several collider and non-collider experiments performed searches for particles as

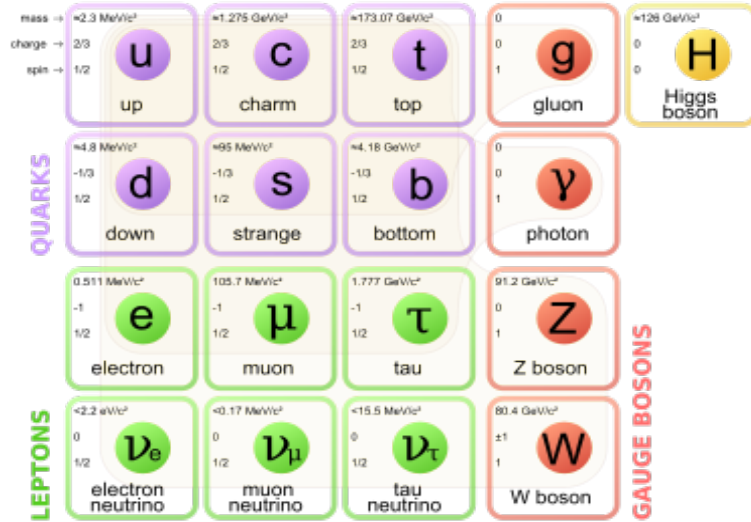


Figure 1.1: The Standard Model particles are shown in a nutshell

predicted by the SM. All the particles of the theory have been found with the exception of the Higgs boson, which appears in the theory as a consequence of the spontaneous electro-weak symmetry breaking [4–6] process.

The Large Hadron Collider (LHC) experiment at CERN, Geneva, is the largest and most powerful accelerator complex ever built. A Toroidal LHC Apparatus (ATLAS) [7] and the Compact Muon Solenoid (CMS) [8], are the two general purpose experiments at the LHC. The main emphasis of the experiments is to look for the electro-weak symmetry breaking [4–6]. mechanism. In 2012, ATLAS and CMS announced the discovery [9, 10] of a Higgs-like particle in the bosonic $H \rightarrow \gamma\gamma$ [11] and $H \rightarrow ZZ$ [12] decay channels using 7 & 8 TeV data (Run-1). However, it is equally important to establish the fermionic coupling of the Higgs boson to confirm its nature. One of the primary aims of the thesis is to look into the fermionic decay mode of the SM Higgs. τ leptons provide a handle to probe the $H \rightarrow \tau\tau$ decay which is one of the main accessible decay channels to establish the fermionic coupling of the Higgs boson. However, dealing with the τ leptons in CMS is very challenging because of the complex decay nature of the τ leptons in the hadronic

background. Analysis of the $H \rightarrow \tau\tau$ channel is divided into various sub-channels to cover the entire $\tau\tau$ decay modes. The LHC has become operational again from end of 2015 after a two year long shutdown, and is delivering collision data at $\sqrt{s} = 13$ TeV at the start-up which is eventually expected to increase to 14 TeV (Run-2).

1.2 Thesis Content

The doctoral thesis is divided into several parts. Chapter 2 briefly discusses the Standard Model of particle physics and the Higgs mechanism. The production of Higgs boson at the LHC energy and its decay modes are discussed to set the perspective of the analyses carried out. The LHC and the experiments are introduced in Chapter 3, focusing on the Compact Muon Solenoid (CMS). A brief description of detector design and layouts is presented.

Chapter 4 deals with the search for the SM Higgs boson in $\tau\tau$ decay mode produced in association with a W boson, which further decays to a highly energetic muon. Two distinct sub-channels have been studied, one where both the τ leptons from the Higgs boson decay hadronically and the other where one of the τ leptons from the Higgs boson decays leptonically, e.g.

- $WH \rightarrow W(\mu) + (H \rightarrow \tau\tau) \rightarrow W(\mu) + H \rightarrow \tau_h\tau_h$
- $WH \rightarrow W(\mu) + (H \rightarrow \tau\tau) \rightarrow W(\mu) + H \rightarrow \mu\tau_h$.

At higher energy and luminosity of Run-2 the associated $H \rightarrow \tau\tau$ channels are expected to become more sensitive and hence more relevant.

The LHC is planning for a luminosity upgrade during 2022 when it is expected to deliver p-p collisions at an instantaneous luminosity of $5 \times 10^{34} \text{cm}^{-2} \text{s}^{-1}$, known as High Luminosity LHC (HL-LHC). This upgrade would increase the LHC mass reach by 20-30 % and allow one to measure the Higgs boson self-coupling and probe its tensor structure, and also look for rare and Beyond SM processes. To cope with the HL-LHC conditions, several components of the CMS detector need to be upgraded. Chapters 5 and 6 deal with the tracker and trigger upgrades of the CMS detector. Chapter 5 discusses electron trigger at Level-1 that uses tracker information from upgraded detector to reduce event rate. Chapter 6 presents the technicalities of an approach for track reconstruction at L1 using the Associative Memory based pattern recognition. An emulation of floating and fixed point representations of a Principal Component Analysis track fitter have been introduced.

Chapter 7, summarises the work presented in the thesis and discusses about further scope of the work in future.

Bibliography

- [1] S. L. Glashow, Partial Symmetries of Weak Interactions, Nucl. Phys. 22 (1961) 579.
- [2] S. Weinberg, A Model of Leptons, Phys. Rev. Lett. 19 (1967) 1264.
- [3] A. Salam, Elementary Particle Physics, N. Svartholm ed., Almquist and Wiksell, Stockholm (1968).
- [4] F. Englert and R. Brout, Broken symmetry and the mass of gauge vector mesons, Phys. Rev. Lett. 13 (1964) 321.
- [5] P. W. Higgs, Broken symmetries, massless particles and gauge fields, Phys. Lett. 12 (1964) 132.
- [6] P. W. Higgs, Broken symmetries and the masses of gauge bosons, Phys. Rev. Lett. 13 (1964) 508.
- [7] ATLAS Collaboration, “The ATLAS Experiment at the CERN Large Hadron Collider”, JINST 03 (2008) S08003.
- [8] CMS Collaboration, “The CMS Experiment at the CERN LHC”, JINST 03 (2008) S08004.
- [9] CMS Collaboration, “Observation of a new boson at a mass of 125 GeV with the CMS experiment at the LHC”, Phys. Lett. B 716 (2012) 30.
- [10] CMS Collaboration, “Observation of a new boson with mass near 125 GeV in pp collisions at $\sqrt{s} = 7$ and 8 TeV”, doi:10.1007/JHEP06(2013)081.
- [11] CMS Collaboration, “Observation of the diphoton decay of the Higgs boson and measurement of its properties”, doi:10.1140/epjc/s10052-014-3076-z.

- [12] CMS Collaboration, “Measurement of the properties of a Higgs boson in the four lepton final state”, doi:10.1103/PhysRevD.89.092007.

The Standard Model of Particle Physics

2.1 Introduction

The Standard Model [1-3] describes the visible matter in the universe and their interactions at the most fundamental level. There are two types of elementary particles: fermions and bosons. Fermions are spin $\frac{1}{2}$ particles and follow Pauli exclusion principle, where no two fermions can have the same quantum state. Bosons have integer spin and are allowed to have the same state. They act as the mediator of forces. There are in total of 12 known fermions, splited in 6 leptons and 6 quarks, further categorized in 3 generations according to their masses. Among the 6 leptons, $\begin{pmatrix} e \\ \nu_e \end{pmatrix}$ is the 1st genera-

tion, $\begin{pmatrix} \mu \\ \nu_\mu \end{pmatrix}$ is 2nd generation and $\begin{pmatrix} \tau \\ \nu_\tau \end{pmatrix}$ pair is the 3rd generation particles. Similarly, 6 quarks are divided into 3 generations as follows, $\begin{pmatrix} u \\ d \end{pmatrix}$, $\begin{pmatrix} c \\ s \end{pmatrix}$ and $\begin{pmatrix} t \\ b \end{pmatrix}$. Charged leptons and quarks can interact through electromagnetic interaction mediated by photon (γ). W and Z bosons are mediator of weak forces. Quarks which have color charge, participate in strong interaction mediated by gluons (g). Both γ and g are massless, whereas W and Z bosons which participate in weak interactions are massive. Figure 2.1 illustrates the interactions of SM particles. Two interacting particles are shown to be connected by a line, whereas the loops indicate a self coupling behavior of the particles.

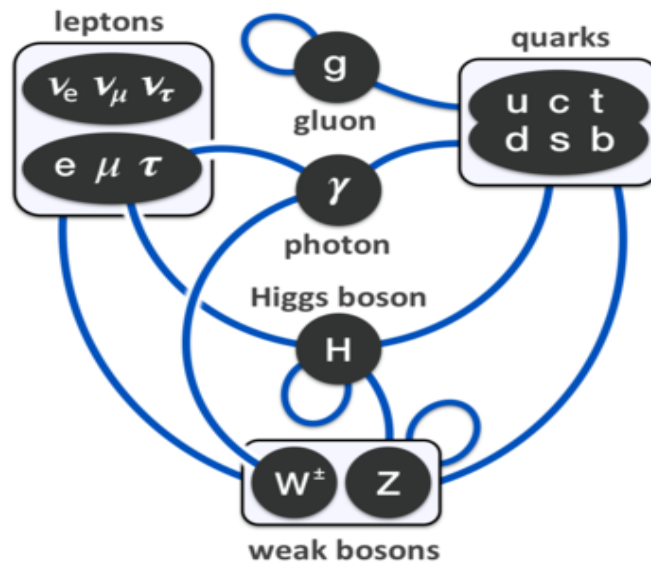


Figure 2.1: The SM Particles and their interactions.

2.2 The Gauge Symmetry Group of the Standard Model

A gauge theory is a quantum field theory with some internal symmetry that governs its dynamics. The Standard Model is described by Quantum Field Theory where every

particle is represented as a dynamical field $\psi(x)$ in the four dimensional space time (x). The dynamical field should respect the symmetry principles: spatial rotation, spatial translational and boosts of the reference frame. The gauge symmetry group of the Standard Model is represented by,

$$SU(3)_{color} \times SU(2)_{isospin} \times U(1)_{hypercharge}.$$

Quantum Chromodynamics (QCD) describes the interactions of the colored quarks and gluons under the sub-group $SU(3)_{color}$. Gluons (g) are basically the 8 generators of the $SU(3)_{color}$ sub-group. The sub-group $SU(2)_{isospin} \times U(1)_{hypercharge}$ describes the electro-weak interactions, where $SU2$ provides 3 generators corresponding to the weak nuclear interactions and $U(1)$ provides 1 generator for electromagnetic interactions.

2.2.1 $U(1)$ QED Theory

When the local gauge transformation,

$$\psi(x) \rightarrow e^{i\alpha(x)}\psi(x), \quad (2.1)$$

where $\alpha(x)$ phase factor depends on space-time coordinates, is imposed on the free Lagrangian of the fermions,

$$\mathcal{L} = i\bar{\psi}\gamma^\mu\partial_\mu\psi - m\bar{\psi}\psi \quad (2.2)$$

and the covariant derivative is constructed as,

$$D_\mu \equiv \partial_\mu - ieA_\mu, \quad (2.3)$$

where A_μ transforms under

$$A_\mu \rightarrow A_\mu + \frac{1}{e} \partial_\mu \alpha, \quad (2.4)$$

the gauge invariant QED Lagrangian reads as

$$\mathcal{L} = \underbrace{\bar{\psi}(i\gamma^\mu \partial_\mu - m)\psi}_{free} + \underbrace{e\bar{\psi}\gamma^\mu A_\mu\psi}_{int} - \underbrace{\frac{1}{4}F_{\mu\nu}F^{\mu\nu}}_{kinetic}, \quad (2.5)$$

where

$$F_{\mu\nu} = \partial_\mu A_\nu - \partial_\nu A_\mu \quad (2.6)$$

is the gauge invariant field strength tensor. A mass term $\frac{1}{2}mA_\mu A^\mu$ in 2.5 is prohibited by gauge invariance. So, simply by requiring a natural local phase invariance on the free fermion Lagrangian, an interacting field theory of QED is achieved with a massless gauge field A_μ (photon).

2.2.2 $SU(3)$ QCD Theory

In a similar manner, the idea of $U(1)$ gauge invariance is translated to the phase transformations on quark color fields described by $SU(3)$ group. If q_1, q_2 and q_3 represent the three color fields corresponding to a quark flavor, then the free Lagrangian is given by,

$$\mathcal{L}_{free} = \bar{q}_j(i\gamma_\mu \partial_\mu - m)q_j, \quad (2.7)$$

where $j \equiv 1, 2, 3$. It has to be invariant under local $SU(3)$ phase transformation in the color space,

$$q(x) \rightarrow Uq(x) \equiv e^{i\alpha_a(x)T_a}q(x), \quad (2.8)$$

where U is an arbitrary 3×3 matrix parameterized as $e^{i\alpha_a(x)T_a}$. T_a with $a = 1 \rightarrow 8$ are the generators of the group. The group is non-abelian since not all the generators commute with each other. The matrices T_a are traceless and obey the following commutation

relation,

$$[T_a, T_b] = if_{abc}T_c, \quad (2.9)$$

where f_{abc} are the structure constants of $SU(3)$ group. Under an infinitesimal $SU(3)$ transformation,

$$q(x) \rightarrow [1 + i\alpha_a(x)T_a]q(x) \quad (2.10)$$

and

$$\partial_\mu q \rightarrow (1 + i\alpha_a T_a)\partial_\mu q + iT_a q \partial_\mu \alpha_a \quad (2.11)$$

In order to keep \mathcal{L}_{free} invariant under these transformations, a covariant derivative of the form

$$D_\mu = \partial_\mu + igT_a G_\mu^a, \quad (2.12)$$

where G_μ^a transforms as

$$G_\mu^a \rightarrow G_\mu^a - \frac{1}{g}\partial_\mu \alpha_a - f_{abc}\alpha_b G_\mu^c \quad (2.13)$$

is constructed. The final $SU(3)$ invariant QCD Lagrangian reads as

$$\mathcal{L} = \underbrace{\bar{q}(i\gamma^\mu \partial_\mu - m)q}_{free} - \underbrace{g(\bar{q}\gamma^\mu T_a q)G_\mu^a}_{interaction} - \underbrace{\frac{1}{4}G_{\mu\nu}^a G_a^{\mu\nu}}_{kinetic}, \quad (2.14)$$

where $G_{\mu\nu}^a$ field stress tensor is given by

$$G_{\mu\nu}^a = \partial_\mu G_\nu^a - \partial_\nu G_\mu^a - gf_{abc}G_\mu^b G_\nu^c. \quad (2.15)$$

So, by demanding $SU(3)$ local gauge invariance on the \mathcal{L}_{free} Lagrangian, the Lagrangian corresponding to the interacting colored quark and gluon fields in Eq. 2.14 is achieved. Just like the photon, local gauge invariance requires the gluons to be massless. The kinetic energy term in Eq. 2.14 is not purely kinetic, but includes an induced self-interaction between the gauge bosons (gluons). This is a unique feature of the non-abelian gauge group and reflects the fact that the gluons themselves carry color charge.

2.2.3 $SU(2)_L \otimes U(1)_Y$ Electro-Weak Theory

Both photons and gluons are required to be massless by the gauge invariance principle in QED and QCD. A similar approach does not really fit in for the weak nuclear interactions, where the associated gauge bosons (W^\pm, Z) are actually massive ($\sim 100\text{GeV}$). It is not possible to add a mass term in the Lagrangian by hand and break the symmetry, because that would make the theory unrenormalizable. To describe weak interactions, a more elaborated structure is needed since there are several fermionic flavors and different properties for left and right handed fields; moreover, the left-handed fermions should appear in doublets, and the presence of massive gauge bosons W^\pm and Z in addition to the photon is essential.

$SU(2)$ is the simplest group with doublet representation. An additional $U(1)$ group is required to include the electromagnetic interactions. So the obvious symmetry group for electro-weak interactions should have a form of $SU(2)_L \otimes U(1)_Y$, where L stands for left-handed fermions and Y is the hypercharge. It is worth mentioning that the $U(1)_Y$ is not exactly the electromagnetic symmetry group $U(1)_{EM}$. $U(1)_{EM}$ is actually hidden inside $SU(2)_L \otimes U(1)_Y$. For plainness, let's consider only the first generation of quarks,

$$\psi_1(x) = \begin{pmatrix} u \\ d \end{pmatrix}_L \quad \psi_2(x) = u_R \quad \psi_3(x) = d_R \quad (2.16)$$

or leptons

$$\psi_1(x) = \begin{pmatrix} \nu_e \\ e^- \end{pmatrix}_L \quad \psi_2(x) = \nu_{eR} \quad \psi_3(x) = e_R^- \quad (2.17)$$

Like in the QED and QCD cases, the free Lagrangian can be written as,

$$\mathcal{L}_{free} = \sum_{j=1}^3 i\bar{\psi}_j(x)\gamma^\mu\partial_\mu\psi_j(x), \quad (2.18)$$

which is invariant under global transformation in flavor space,

$$\begin{aligned}
\psi_1(x) &\rightarrow e^{iy_1\beta} U_L \psi_1(x) \\
\psi_2(x) &\rightarrow e^{iy_2\beta} \psi_2(x) \\
\psi_3(x) &\rightarrow e^{iy_3\beta} \psi_3(x),
\end{aligned} \tag{2.19}$$

where $SU(2)_L$ transformation

$$U_L \equiv e^{i\frac{\sigma_i}{2}\alpha^i} \quad (i = 1, 2, 3) \tag{2.20}$$

only operates on the doublet field $\psi_1(x)$. σ_i 's are Pauli matrices and generator of the $SU(2)$ group. There is no mass term in the Lagrangian because that would spoil the symmetry transformation because right-handed fields do not transform and the following term,

$$\begin{aligned}
m\bar{\psi}\psi &= \frac{1}{4}m\bar{\psi}(1 - \gamma^5)(1 - \gamma^5)\psi + \frac{1}{4}m\bar{\psi}(1 + \gamma^5)(1 + \gamma^5)\psi \\
&= m\bar{\psi}_R\psi_L + m\bar{\psi}_L\psi_R
\end{aligned} \tag{2.21}$$

is not gauge invariant. Now if the Lagrangian is required to be invariant under local $SU(2)_L \otimes U(1)_Y$, i.e., with $\alpha^i \equiv \alpha^i(x)$ and $\beta \equiv \beta(x)$, in the QED analogous way the covariant derivatives can be constructed as

$$\begin{aligned}
D_\mu\psi_1(x) &\equiv [\partial_\mu + ig\widetilde{W}_\mu(x) + ig'y_1B_\mu(x)]\psi_1(x) \\
D_\mu\psi_2(x) &\equiv [\partial_\mu + ig'y_2B_\mu(x)]\psi_2(x) \\
D_\mu\psi_3(x) &\equiv [\partial_\mu + ig'y_3B_\mu(x)]\psi_3(x),
\end{aligned} \tag{2.22}$$

where $\widetilde{W}_\mu(x) \equiv \frac{\sigma_i}{2}W_\mu^i(x)$ and B_μ denote the $SU(2)_L$ and $U(1)_Y$ gauge fields respectively and transform as,

$$\begin{aligned}
B_\mu(x) &\rightarrow B_\mu(x) - \frac{1}{g'}\partial_\mu\beta(x) \\
\widetilde{W}_\mu(x) &\rightarrow U_L(x)\widetilde{W}_\mu(x)U_L^\dagger(x) + \frac{1}{g}\partial_\mu U_L(x)U_L^\dagger(x).
\end{aligned} \tag{2.23}$$

The Lagrangian

$$\mathcal{L} = \sum_{j=1}^3 i\bar{\psi}_j(x)\gamma^\mu D_\mu\psi_j(x) \quad (2.24)$$

is invariant under local $SU(2)_L \otimes U(1)_Y$ transformation and the properly normalized kinetic Lagrangian can be shown as,

$$\mathcal{L}_{kinetic} = -\frac{1}{4}B_{\mu\nu}B^{\mu\nu} - \frac{1}{4}W_{\mu\nu}^i W_i^{\mu\nu}, \quad (2.25)$$

where $B_{\mu\nu}$ and $W_{\mu\nu}^i$ are field strength tensors

$$\begin{aligned} B_{\mu\nu} &\equiv \partial_\mu B_\nu - \partial_\nu B_\mu \\ W_{\mu\nu}^i &\equiv \partial_\mu W_\nu^i - \partial_\nu W_\mu^i - g\epsilon^{ijk}W_\mu^j W_\nu^k. \end{aligned} \quad (2.26)$$

As $W_{\mu\nu}^i$ contains a quadratic field term, the Lagrangian $\mathcal{L}_{kinetic}$ gives rise to cubic and quartic self-interactions of the gauge fields.

So, $SU(2)_L \otimes U(1)_Y$ presents a unified theory of electro-weak interactions but the basic problem remains. The gauge bosons and fermions are still massless as can be seen from the Lagrangian in Eq. 2.24 and Eq. 2.25. This is known as the mass problem.

2.3 Spontaneous Symmetry Breaking

As it has already been argued, the mass term can not be put by hand in the Lagrangian to protect the renormalizability of the theory. In order to generate masses, the symmetry has to be broken spontaneously [4–6]. Consider a simple Lagrangian for scalar particles,

$$\mathcal{L} \equiv T - V = \frac{1}{2}(\partial_\mu\phi)^2 - \left(\frac{1}{2}\mu^2\phi^2 + \frac{1}{4}\lambda\phi^4\right), \quad (2.27)$$

with $\lambda > 0$, where \mathcal{L} is required to be invariant under $\phi \rightarrow -\phi$. Two possible forms of the potential V are shown in Figure 2.2.

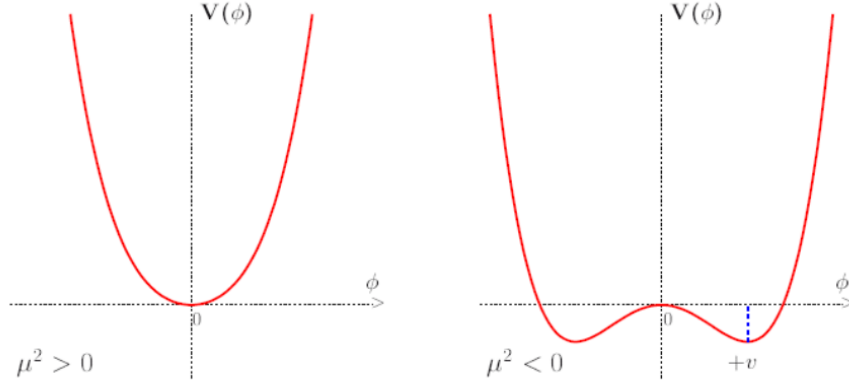


Figure 2.2: One dimension potential $V(\phi)$ for different signs of μ^2

- $\mu^2 > 0$: It represents a self-interacting scalar field with mass μ . The vacuum corresponds to $\phi = 0$.
- $\mu^2 < 0$: In this case the relative sign between the kinetic energy T and the ϕ^2 term is positive. So the mass term has got a wrong sign. Unlike the previous case, here the scalar field ϕ has two minima at $\phi = \pm v$, where $v = \sqrt{(-\mu^2/\lambda)}$.

For the second scenario, the field ϕ can be expanded around the minima as,

$$\phi(x) = v + \eta(x), \quad (2.28)$$

where $\eta(x)$ represents the quantum fluctuation around the minima. Now substituting Eq. 2.28 in the Lagrangian in Eq. 2.27 yields,

$$\mathcal{L}' = \frac{1}{2}(\partial_\mu \eta)^2 - \lambda v^2 \eta^2 - \lambda v \eta^3 - \frac{1}{4} \lambda \eta^4 + \text{constant}. \quad (2.29)$$

In Eq. 2.29, the field η has a mass term with correct sign,

$$m_\eta = \sqrt{(2\lambda v^2)} = \sqrt{-2\mu^2} \quad (2.30)$$

The higher order term in η indicates that the field is self-interacting in nature.

The most surprising part is that the Lagrangian \mathcal{L} in Eq. 2.27 and \mathcal{L}' in Eq. 2.29 are equivalent. Choosing the right vacuum is important while doing the perturbative expansion. This way of generating a mass term is known as **Spontaneous Symmetry Breaking**. In the Lagrangian \mathcal{L}' of the scalar field ϕ , the reflection symmetry $\phi \rightarrow -\phi$ is apparently broken by the choice of the ground state $\phi = +v$. The fact that there are massless excitations associated with the SSB mechanism is a completely general result, known as the Goldstone theorem. If a Lagrangian is invariant under a continuous symmetry group G , but the vacuum is only invariant under a subgroup $H \subset G$, then there must exist as many massless spin-0 particles (Nambu-Goldstone bosons) as broken generators (i.e., generators of G which do not belong to H).

2.4 The Higgs Mechanism

The Higgs mechanism [4–6] helps to avoid massless particles in the theory. Consider spontaneous breaking of a local $SU(2)$ gauge symmetry of the Lagrangian,

$$\mathcal{L} = (\partial_\mu \phi)^\dagger (\partial^\mu \phi) - \mu^2 \phi^\dagger \phi - \lambda (\phi^\dagger \phi)^2, \quad (2.31)$$

where ϕ is an $SU(2)$ doublet of complex scalar field,

$$\phi = \begin{pmatrix} \phi_a \\ \phi_b \end{pmatrix} = \frac{1}{\sqrt{2}} \begin{pmatrix} \phi_1 + i\phi_2 \\ \phi_3 + i\phi_4 \end{pmatrix}. \quad (2.32)$$

The local $SU(2)$ transformation can be written as,

$$\phi \rightarrow e^{i\alpha_a(x)\tau_a/2}\phi. \quad (2.33)$$

It can be shown that given the covariant derivative,

$$D_\mu = \partial_\mu + ig\frac{\tau_a}{2}W_\mu^a \quad (2.34)$$

and an infinitesimal gauge transformation,

$$\phi(x) = (1 + i\alpha(x).\tau/2)\phi(x), \quad (2.35)$$

the three gauge fields corresponding to the three generators of the $SU(2)$ group transform as,

$$W_\mu \rightarrow W_\mu - \frac{1}{g}\partial_\mu\alpha - \alpha \times W_\mu. \quad (2.36)$$

The gauge invariant Lagrangian can be shown as,

$$\mathcal{L} = (\partial_\mu\phi + ig\frac{1}{2}\tau.W_\mu\phi)^\dagger(\partial^\mu\phi + ig\frac{1}{2}\tau.W^\mu\phi) - V(\phi) - \frac{1}{4}W_{\mu\nu}.W^{\mu\nu}, \quad (2.37)$$

where

$$V(\phi) = \mu^2\phi^\dagger\phi + \lambda(\phi^\dagger\phi)^2 \quad (2.38)$$

and

$$W_{\mu\nu} = \partial_\mu W_\nu - \partial_\nu W_\mu - gW_\mu \times W_\nu. \quad (2.39)$$

When $\mu^2 > 0$, the Lagrangian describes a system of four scalar particles, each of mass μ , interacting with three massless gauge bosons. But the scenario with $\mu^2 < 0$ and $\lambda > 0$ is particularly interesting, where the field has degenerate vacuum along the circle as shown in Figure 2.3.

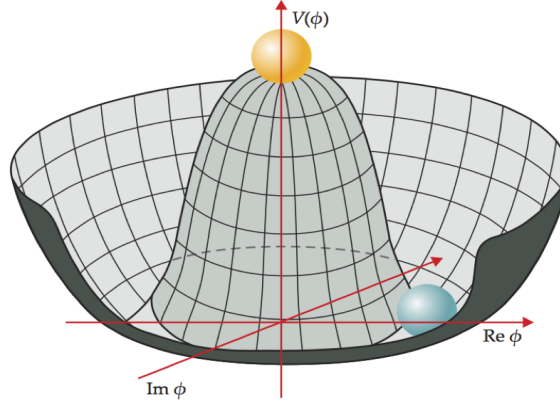


Figure 2.3: Higgs potential $V(\phi)$ for complex field ϕ when $\mu^2 < 0$

The minima can be chosen as,

$$\phi_1 = \phi_2 = \phi_4 = 0, \quad \phi_3^2 = -\frac{\mu^2}{\lambda} \equiv v^2 \quad (2.40)$$

and the field $\phi(x)$ is expanded around this vacuum

$$\phi_0 \equiv \frac{1}{\sqrt{2}} \begin{pmatrix} 0 \\ v \end{pmatrix}, \quad (2.41)$$

as

$$\phi(x) = \frac{1}{\sqrt{2}} \begin{pmatrix} 0 \\ v + h(x) \end{pmatrix}, \quad (2.42)$$

where $h(x)$ is the quantum fluctuation around the minima. If the field $\phi(x)$ in the Lagrangian in Eq. 2.37 is substituted by Eq. 2.42, out of the four scalar fields only the Higgs field remains. Parameterizing the fluctuations from the vacuum ϕ_0 in terms of real fields $\theta_1, \theta_2, \theta_3$ and h can be written as,

$$\phi(x) = e^{i\tau \cdot \theta(x)/v} \begin{pmatrix} 0 \\ \frac{v+h(x)}{\sqrt{2}} \end{pmatrix} \quad (2.43)$$

It is argued that the three massless Goldstone boson fields $\theta(x)$ are *eaten up* by the gauge fields W_μ^a and become massive. The masses of the fields are deduced by simply

substituting ϕ_0 of Eq. 2.41 in the Lagrangian in Eq. 2.37 and found to be of the form,

$$\begin{aligned} \left| ig\frac{1}{2}\tau.W_\mu\phi \right|^2 &= \frac{g^2}{8} \left| \begin{pmatrix} W_\mu^3 & W_\mu^1 - iW_\mu^2 \\ W_\mu^1 + iW_\mu^2 & W_\mu^3 \end{pmatrix} \begin{pmatrix} 0 \\ v \end{pmatrix} \right|^2 \\ &= \frac{g^2 v^2}{8} [(W_\mu^1)^2 + (W_\mu^2)^2 + (W_\mu^3)^2]. \end{aligned} \quad (2.44)$$

These terms can be compared with mass term of a boson, $\frac{1}{2}M^2 B_\mu^2$ with $M = \frac{1}{2}gv$. So, finally the Lagrangian describes three massive gauge fields (W^\pm, Z) and one massive scalar h (Higgs boson). The same Higgs doublet that generates W^\pm and Z masses, is also sufficient to produce masses to the fermions. This technique of mass generation was introduced by several people at the same time during 1950-60 and known as the Higgs mechanism. In the SM the mass of the Higgs boson is a free parameter and it couples to the fermions proportional to their masses. This property makes the Higgs boson an elusive particle to search. The most readily experimentally detectable particles are light fermions which couple to the Higgs boson only very weakly.

2.5 Higgs Production at the Large Hadron Collider

In the Large Hadron Collider, the production mechanism of the SM Higgs boson are coming the Feynman diagrams shown in Figure 2.4. The main production mechanism is the gluon-gluon fusion process, where the Higgs boson is produced from two initial state gluons mediated by virtual heavy fermions (mainly top quark) that couple to the Higgs boson. The second dominant contribution comes from the vector boson fusion (VBF) process, where the Higgs boson is produced at tree level by two vector bosons, leaving a distinct signature of two high energy quarks with a large gap in rapidity between them. VBF production rates are an order of magnitude lower than the dominant mode. Higgs bosons produced in association with a W or a Z boson via the Higgs-strahlung

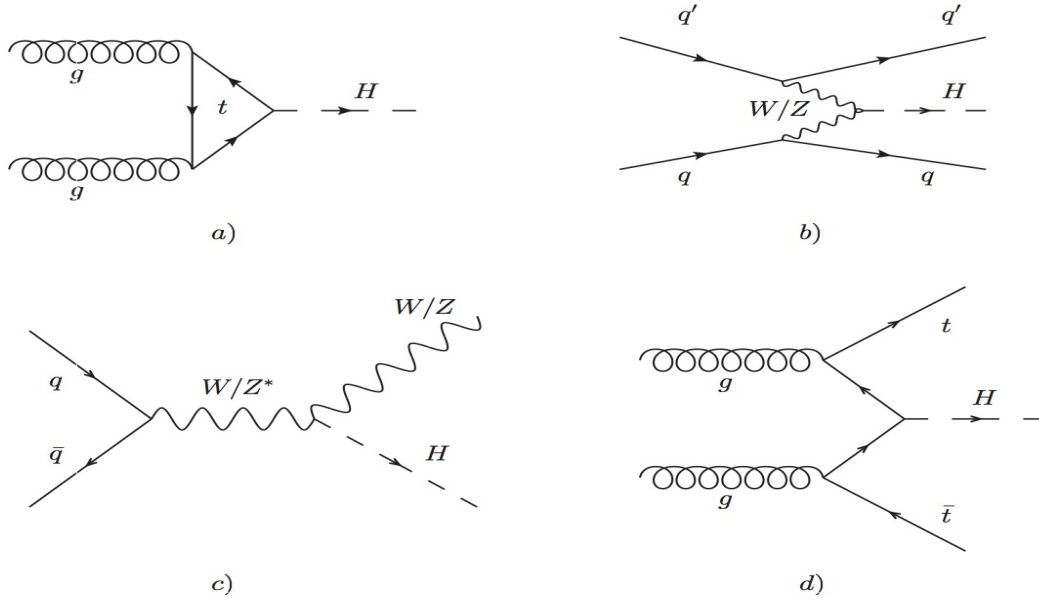


Figure 2.4: Production modes of the SM Higgs boson at the LHC

process has a rate that is roughly another factor of 2 smaller at Higgs boson mass $\sim 125 \text{ GeV}/c^2$. Lastly, the Higgs boson can be produced in association with a top quark and an anti-top quark, with a rate that is roughly another order of magnitude smaller than Higgs-strahlung. While the mass of the Higgs boson is a free parameter in the SM, its couplings to the massive vector bosons, Yukawa couplings to fermions, decay branching fractions and production cross sections in proton-proton collisions are fully defined and well understood theoretically [7]. The cross-sections of the various production modes at $\sqrt{s} = 7 \text{ TeV}$ are shown in Figure 2.5 (left). Once produced, the Higgs boson can decay into fermion or gauge boson pairs. Figure 2.5 (right) is showing the branching fraction of the SM Higgs boson as a function of its mass. In the low mass range $110 < M < 140 \text{ GeV}/c^2$, the dominant decay mode comes from $b\bar{b}$ followed by $\tau\tau$. Direct $H \rightarrow b\bar{b}$ searches are not possible because of the overwhelmingly large di-jet background, that is why $H \rightarrow \tau\tau$ searches play a pilot role in establishing the fermionic coupling of the Higgs boson. Figure 2.6 is summarizing the decay fraction of a $125 \text{ GeV}/c^2$ SM Higgs boson and there is a significant 6 % contribution coming from

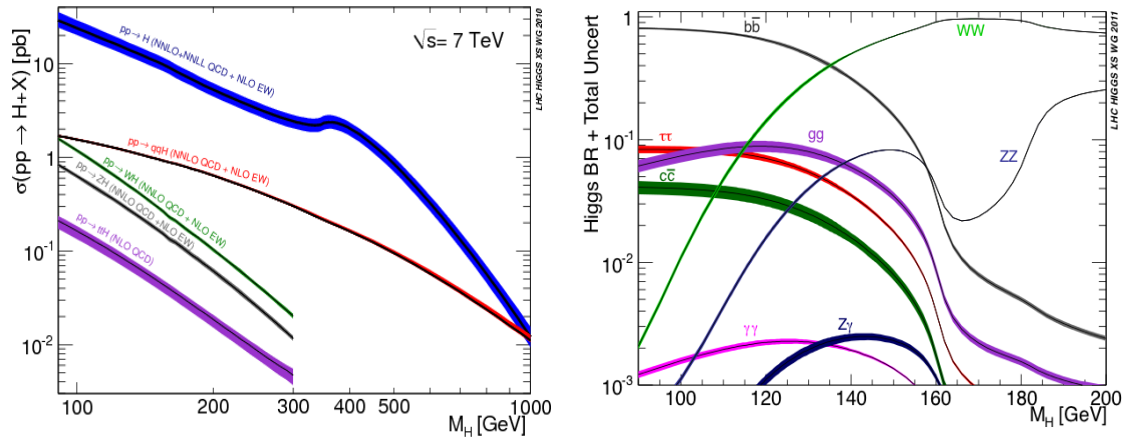


Figure 2.5: **Left:** Cross section of various production modes of the SM Higgs boson at $\sqrt{s}=7$ TeV at the LHC, **Right:** Branching ratio of the SM Higgs boson.

the $\tau\tau$ mode.

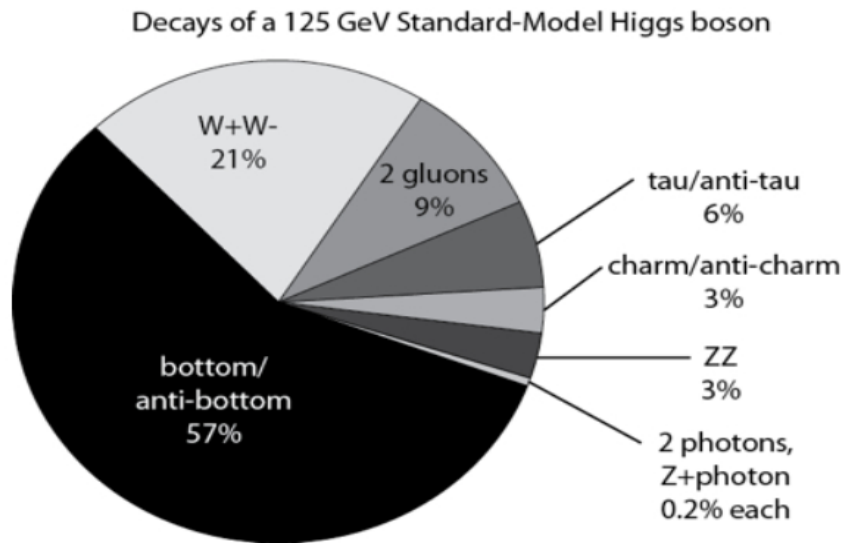


Figure 2.6: Decay fraction of a $125 \text{ GeV}/c^2$ SM Higgs boson

Bibliography

- [1] S. L. Glashow, Partial Symmetries of Weak Interactions, Nucl. Phys. 22 (1961) 579.

-
- [2] S. Weinberg, A Model of Leptons, *Phys. Rev. Lett.* 19 (1967) 1264.
 - [3] A. Salam, *Elementary Particle Physics*, N. Svartholm ed., Almqvist and Wiksell, Stockholm (1968).
 - [4] F. Englert and R. Brout, Broken symmetry and the mass of gauge vector mesons, *Phys. Rev. Lett.* 13 (1964) 321.
 - [5] P. W. Higgs, Broken symmetries, massless particles and gauge fields, *Phys. Lett.* 12 (1964) 132.
 - [6] P. W. Higgs, Broken symmetries and the masses of gauge bosons, *Phys. Rev. Lett.* 13 (1964) 508.
 - [7] LHC Higgs Cross Section Working Group, *Handbook of LHC Higgs Cross Sections: Inclusive Observables*, CERN-2011-002 (2011) arXiv:hep-ph/1101.0593.

The CMS Detector at the LHC

3.1 The Large Hadron Collider

The Large Hadron Collider (LHC) [1] experiment at CERN, Geneva is the largest and most powerful accelerator in the world. This technology miracle provides the platform to perform particle physics experiments to explore the nature of the fundamental forces and the mysteries of nature.

High energy proton beams circulate in opposite directions in the LHC tunnel and collide at four points along the tunnel where four different detector complexes are situated, namely ATLAS [2], CMS [3], ALICE [4] and LHCb [5]. ATLAS and CMS are two general purpose detectors to study Standard Model and Beyond Standard Model physics, with a

special emphasis on electro-weak symmetry breaking mechanism. ALICE and LHCb are built for specific physics interests like Quark-Gluon plasma and B-physics, respectively.

Figure 3.1 shows the schematic of the LHC accelerator complex. To create the two high energy proton beams, protons are first accelerated in the Linac2 linear accelerator and then transferred to the Proton Synchrotron Booster where they are accelerated to 1.4 GeV. They are then transferred to the Proton Synchrotron (PS) ring where they get arranged into bunches spaced 25 or 50 ns apart, and accelerated further to 26 GeV. The proton beams are then transported to the Super Proton Synchrotron (SPS), accelerated to 450 GeV and finally injected into the LHC tunnel. Eight radio frequency (RF) resonating cavities are responsible for accelerating the proton beams to the final center of mass energy through a field gradient of 5.5 MV/m increasing the energy of the beams by 16 MeV per turn.

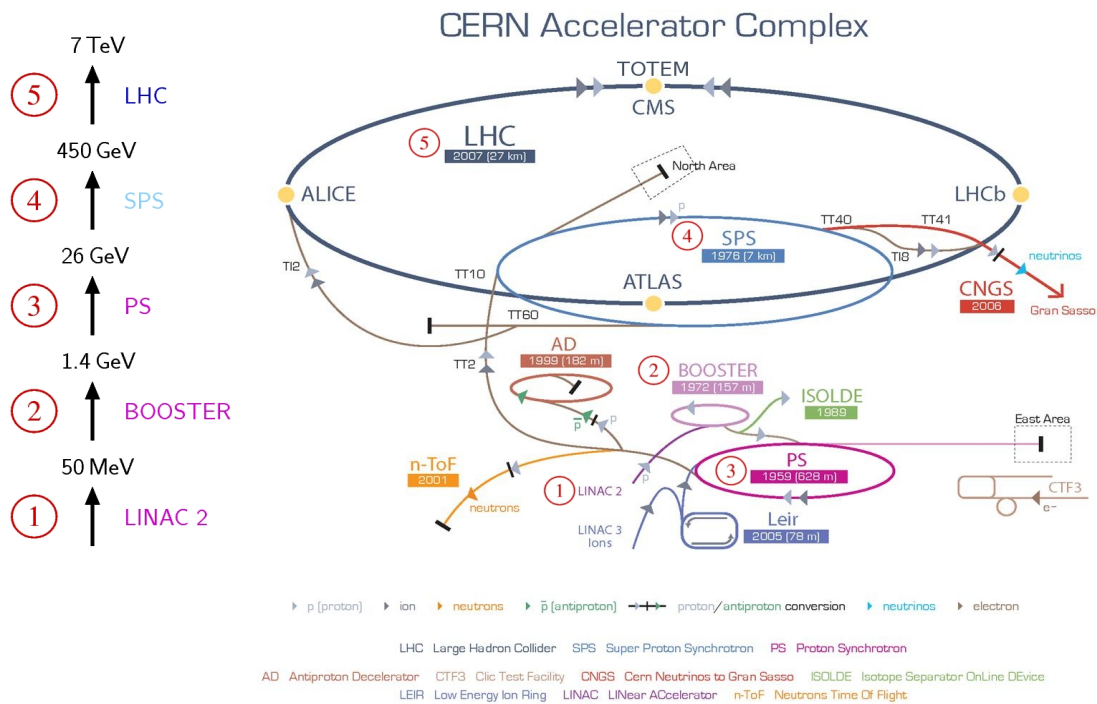


Figure 3.1: A schematic view of the CERN LHC Accelerator Complex

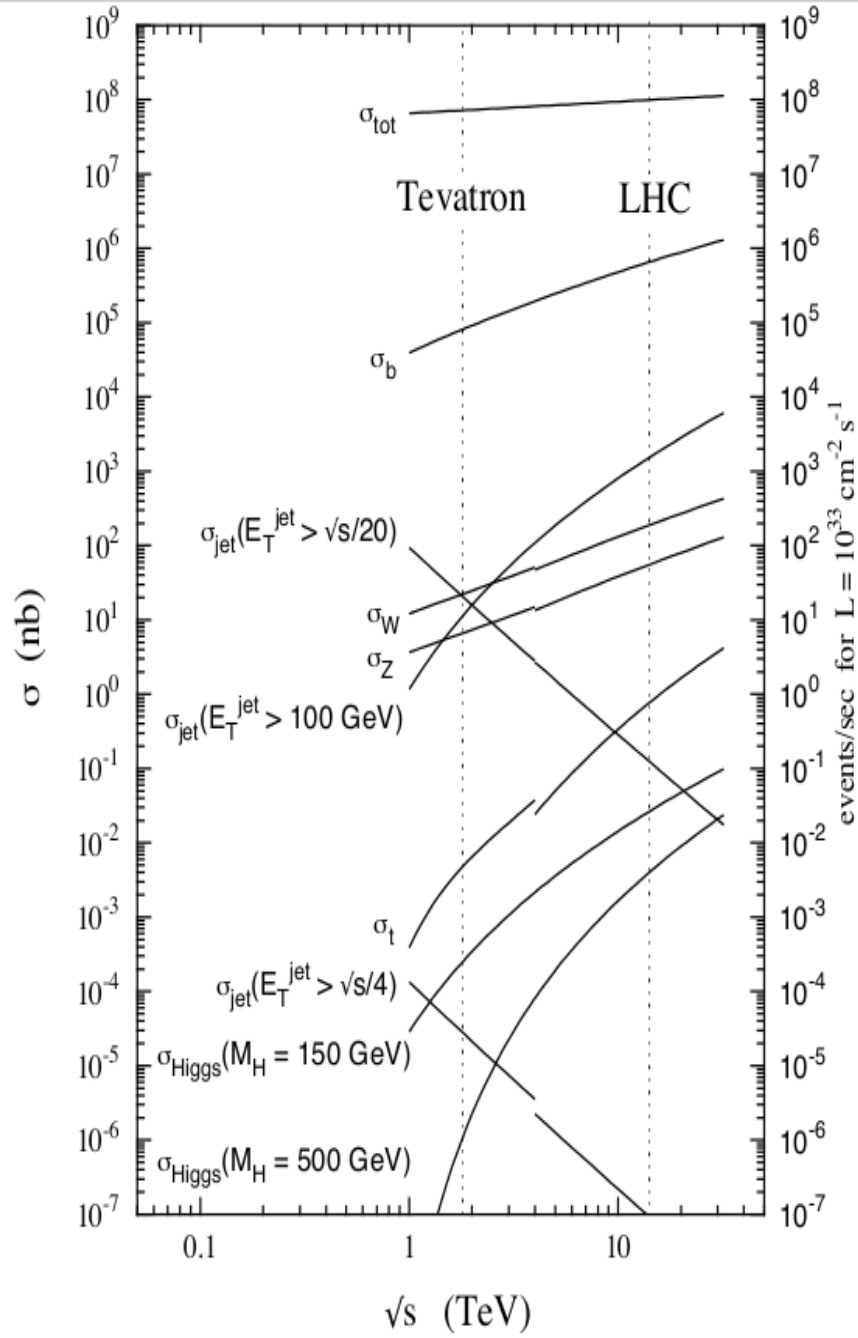
The designed instantaneous luminosity of $10^{34} \text{cm}^{-2} \text{s}^{-1}$ is expected to be reached with beams consisting of 2808 bunches with 10^{11} protons per bunch. The instantaneous luminosity is given by

$$L = \frac{N_p^2 n_b f_{rev} \gamma_r}{4\pi \epsilon_n \beta^*} F, \quad (3.1)$$

where

- N_p is the number of protons per bunch,
- n_b is the number of bunches per beam,
- f_{rev} is the revolution frequency,
- γ_r is the relativistic gamma factor,
- ϵ_n is the normalized transverse beam emittance,
- β^* is the value of the beta function at the collision point which relates to the transverse size of the beams at the interaction point,
- F is the geometric factor due to the crossing angle of the two beams.

The LHC physics programme aims at exploring rare processes at unexplored energy scales. These events of interest are hidden by a huge rate of inelastic, non-diffractive collisions with a total cross section of about 60 mb. A comparison of the cross sections for different processes at the Tevatron and the LHC is depicted in Figure 3.2. It shows, for example, that the cross section for the SM Higgs Physics is several order of magnitude lower than the QCD or electro-weak background processes.

Figure 3.2: Cross sections as a function of collision energy \sqrt{s}

3.2 The CMS Detector

The CMS detector at the Large Hadron Collider experiment at CERN is a gigantic apparatus which surrounds one of the four collision points of the LHC. The detector can be thought of as a cylindrical onion comprising several co-axial detector layers. The final state particles in each collision leave their traces in the sub-detector layers while flying off. The overall layout of the CMS is shown in Figure 3.3. The backbone of

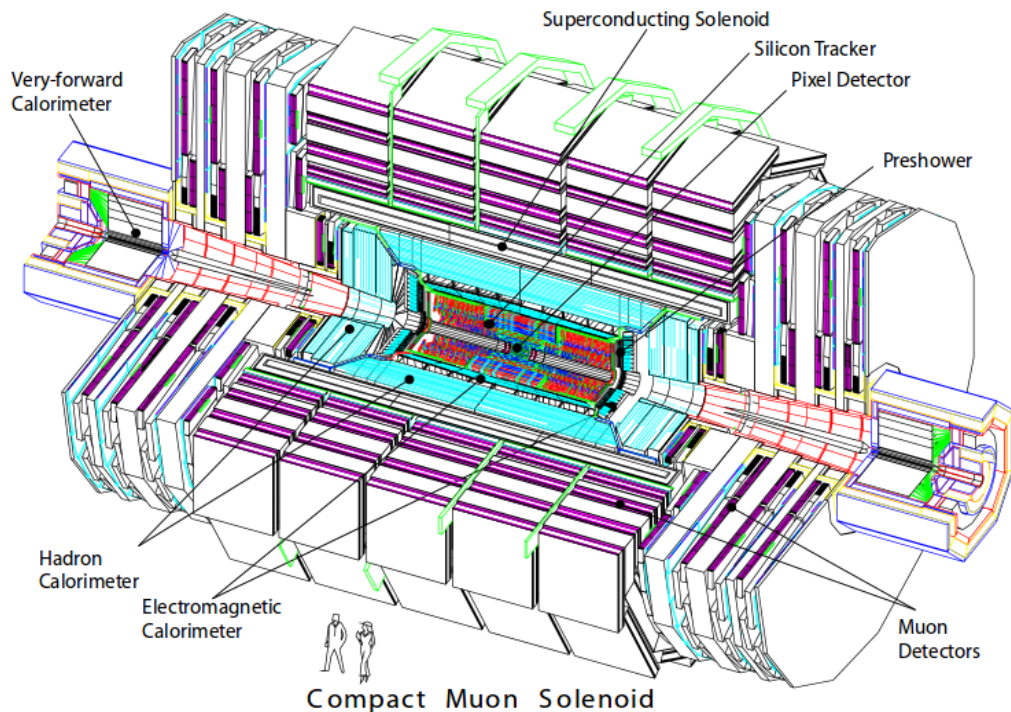


Figure 3.3: The Layout of the CMS Detector

the CMS detector is a superconducting solenoid which provides a magnetic field of 3.8 Tesla and also acts as a support structure. Within the field volume, starting from the interaction point, is a silicon tracker, a lead tungstate crystal calorimeter (ECAL) and a brass/scintillator hadron calorimeter (HCAL). Muons are measured in gas-ionization detectors embedded in the steel flux-return yoke outside the solenoid. Disc like endcap

modules and extensive forward calorimeters complement the coverage provided by the barrel detectors. Figure 3.4 shows a transverse slice of the CMS detector. A more

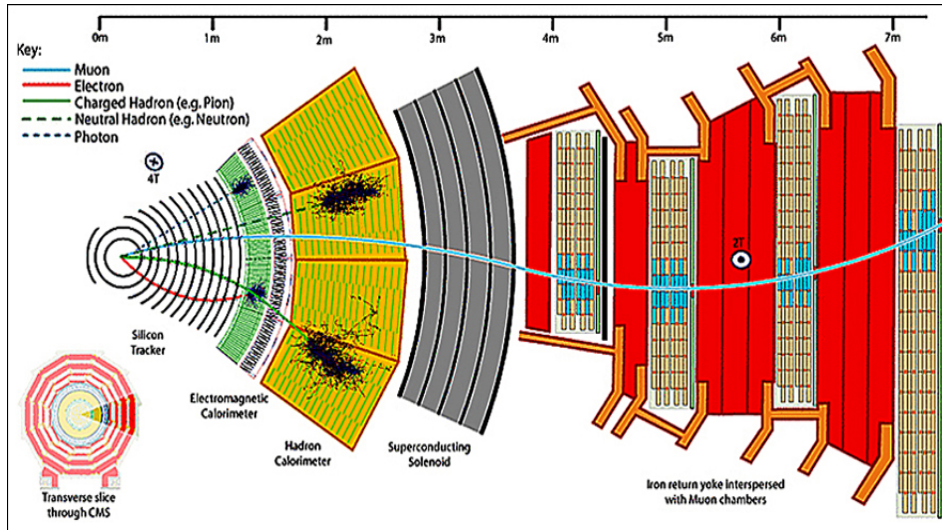


Figure 3.4: Transverse slice of the CMS detector.

detailed description of the CMS detector can be found in [3].

3.2.1 The CMS Magnet

The measurement of momentum of highly energetic charge particles is facilitated by the strong magnetic field of 3.8 Tesla of the CMS superconducting solenoid [6, 7]. It is one of the major components of the detector and also acts as a support structure to mount not only the magnet but also other detector modules. Figure 3.5 shows an artistic view of the solenoid. The main features of the CMS solenoid are the use of a high-purity aluminium-stabilized conductor and indirect cooling. A four-layer winding has been adopted using a novel conductor with a larger cross-section that can withstand an outward pressure (hoop stress) of 64 atmospheres.

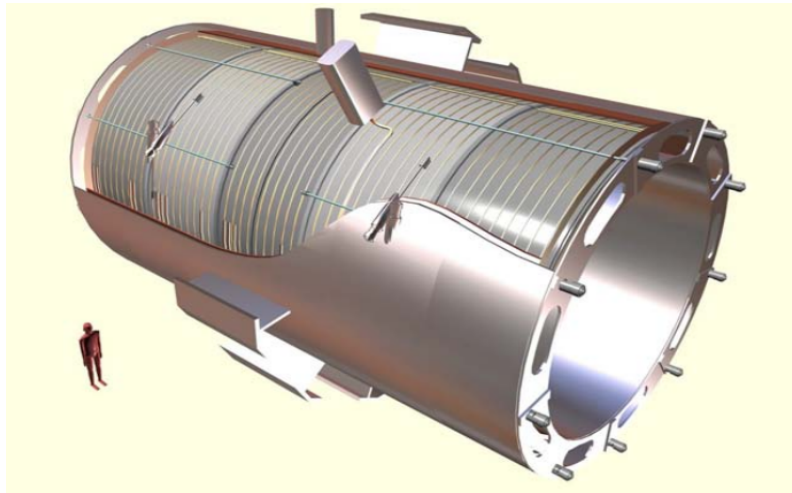


Figure 3.5: An artistic view of the 5 modules composing the cold mass inside the cryostat, with details of the support system.

3.2.2 Tracking Detector

The tracking system is the innermost component of the complex CMS detector, placed close to the LHC beam pipe. It is designed to provide a precise and efficient measurement of the trajectories of charged particles emerging from the LHC collisions, as well as a precise reconstruction of secondary event vertices. Proximity to the interaction vertex forces these detectors to have high granularity and radiation hardness.

The CMS tracker [8] is composed of silicon pixel detectors and silicon strip detectors. Figure 3.6 shows a schematic representation of the tracker layout in longitudinal plane. The Pixel detector has three barrel layers at radii between 4.4 cm and 10.2 cm. The detector delivers three high precision space points on each charged particle trajectory. Two endcap discs are placed on each side, extending the η coverage to 2.5. The silicon strip tracker has 10 barrel detection layers extending outwards to a radius of 1.1 m. Among these 10 layers, 4 are Tracker Inner Barrel (TIB) and 6 are Tracker Outer Barrel (TOB). Each system is completed by endcaps which consist of 3 Tracker Inner Discs

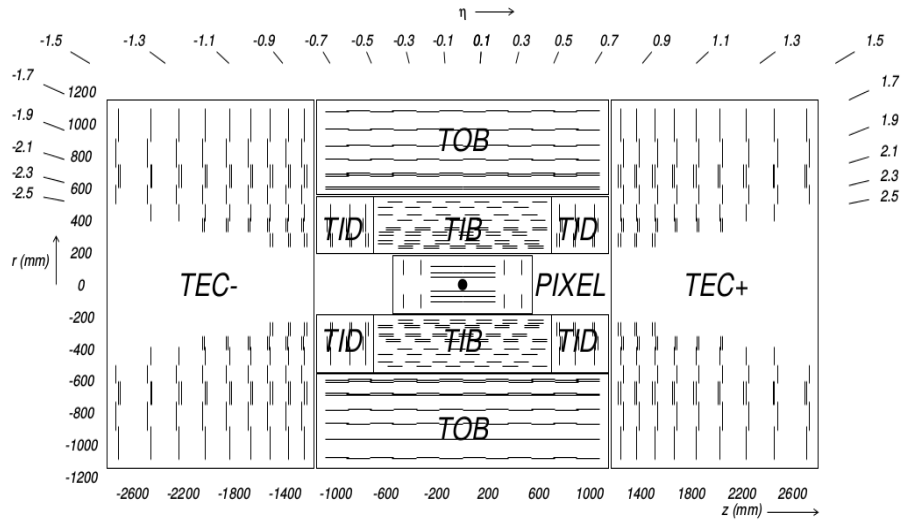


Figure 3.6: A schematic representation of the CMS tracker layouts in the longitudinal plane.

(TID) plus 9 Tracker Endcap (TEC) discs on each side of the barrel. With about 200 m² of active silicon area the CMS tracker is the largest silicon tracker ever built.

Figure 3.7 and Figure 3.8 show the expected resolution of transverse momentum, longitudinal impact parameter and transverse impact parameter, as a function of pseudorapidity for single muons of transverse momenta of 1, 10 and 100 GeV/c . For high momentum tracks (100 GeV/c), the transverse momentum resolution is around 1 - 2% up to $|\eta| \sim 1.6$, beyond which it degrades due to the reduced lever arm. The amount of material inside the tracker volume, technically known as Material Budget, is kept as minimum as possible to reduce multiple scattering which can degrade the resolution of measured track parameters. Figure 3.9 shows the material budget of the CMS tracker for different subsystems as a function of pseudorapidity.

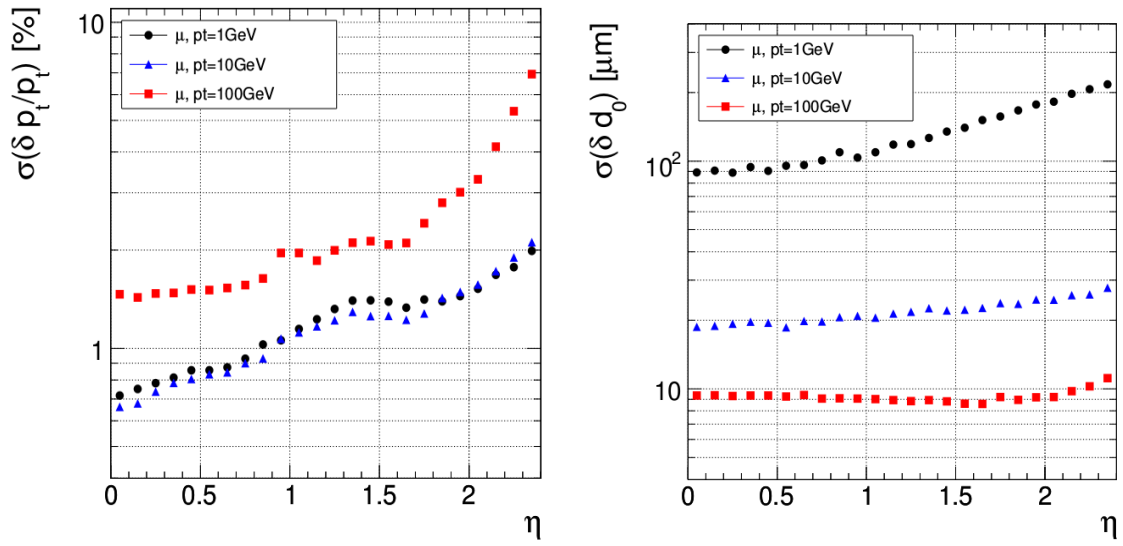


Figure 3.7: Expected transverse momentum (left) and longitudinal impact parameter (right) resolution of muons.

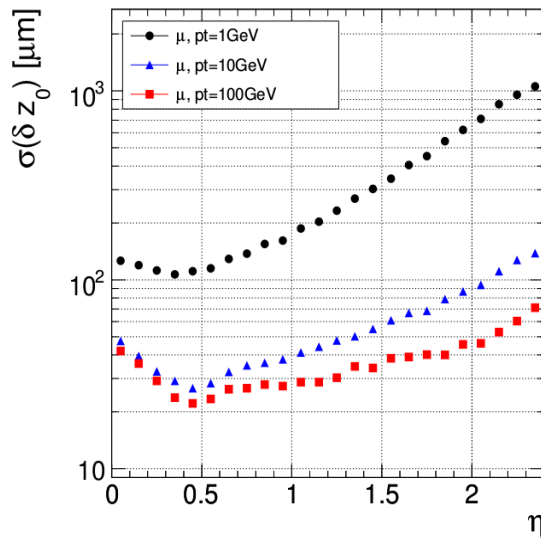


Figure 3.8: Expected transverse impact parameter resolution of muons

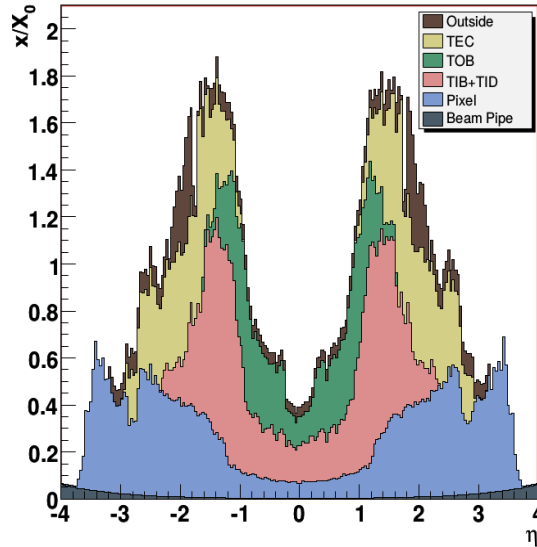


Figure 3.9: Material budget of the CMS tracker as a function of pseudorapidity with contribution from individual sub-components.

3.2.3 Electromagnetic Calorimeter

The Electromagnetic Calorimeter (ECAL) [9] is a hermetic, homogeneous calorimeter. It has around 60000 lead tungstate (PbWO_4) crystals mounted in the central barrel part, closed by around 7000 crystals in each of the 2 endcaps. The high density (8.28 g/cm^3), short radiation length ($X_0 = 0.89 \text{ cm}$) and small Moliere radius (2.2 cm) result in a fine granularity and compact calorimeter. These scintillating crystals are radiation hard (up to 10 Mrad) and have fast response time and 80% of the light is emitted within 25 ns. However, these crystals have relatively low light yield ($30 \text{ } \gamma/\text{MeV}$) which varies with temperature. Photodetectors with intrinsic gain that can operate in a magnetic field are used, Silicon avalanche photodiodes (APDs) in the barrel and vacuum phototriodes (VPTs) in the endcaps. Figure 3.10 illustrates a schematic layout of the CMS electromagnetic calorimeter showing the arrangement of crystal modules, supermodules and endcaps, with the preshower in front. The barrel section of the Electromagnetic

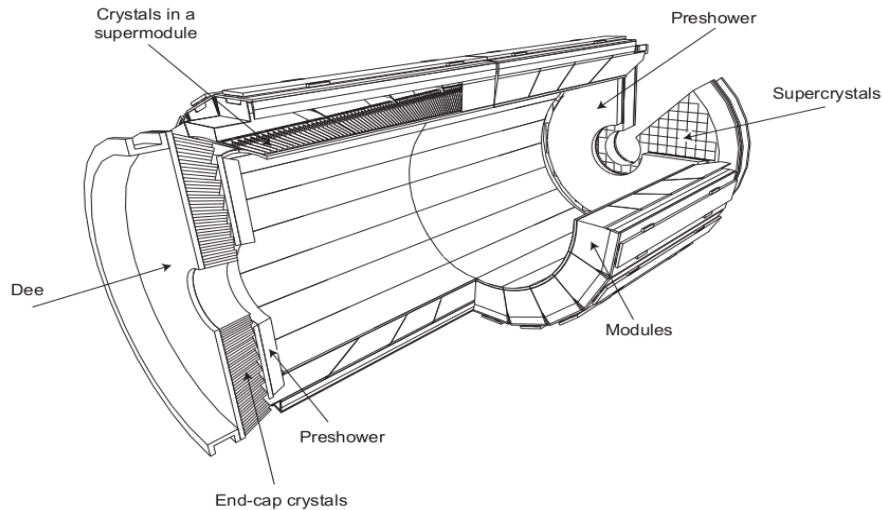


Figure 3.10: A schematic 3D view of the ECAL geometry

Calorimeter (EB) has an inner radius of 129 cm . It consists of 36 identical “supermodules”, each spreading over half the barrel length and corresponding to a pseudorapidity range of $0 < |\eta| < 1.479$. The crystals are mounted in a quasi-projective geometry where the axes are tilted by 3° with respect to the line from the nominal vertex position, to avoid cracks aligned with particle trajectories. The crystals have a dimension of $22 \times 22 \times 230\text{ mm}^3$. The endcaps (EE) of the calorimeter are at a distance of 314 cm from the vertex and cover a pseudorapidity range of $1.479 < |\eta| < 3.0$. A preshower device is placed in front of the crystal calorimeter over much of the endcap pseudorapidity range from $|\eta| = 1.65 - 2.61$. The aim of the CMS Preshower detector is to separate photons from neutral pions decaying to two closely spaced photons picked up together by the ECAL in the endcaps within a fiducial region $1.653 < |\eta| < 2.6$. It also helps identification of electrons against minimum ionizing particles, and improves position determination of electrons and photons with its superior granularity and position resolution. It is a sampling calorimeter with 2 layers: lead radiators initiate electromagnetic showers from incoming photons/electrons whilst silicon strip sensors placed after each

radiator measure the energy deposited and the transverse shower profiles.

The energy resolution of the calorimeter is expressed by Eq. 3.2, where S is the stochastic term, N the noise and C the constant term. The stochastic term includes fluctuations in the shower containment as well as a contribution from photostatistics.

$$\left(\frac{\sigma}{E}\right)^2 = \left(\frac{S}{\sqrt{E}}\right)^2 + \left(\frac{N}{E}\right)^2 + C^2 \quad (3.2)$$

Figure 3.11 demonstrates the energy ECAL energy resolution which is better than 1 % for $E_T > 20$ GeV.

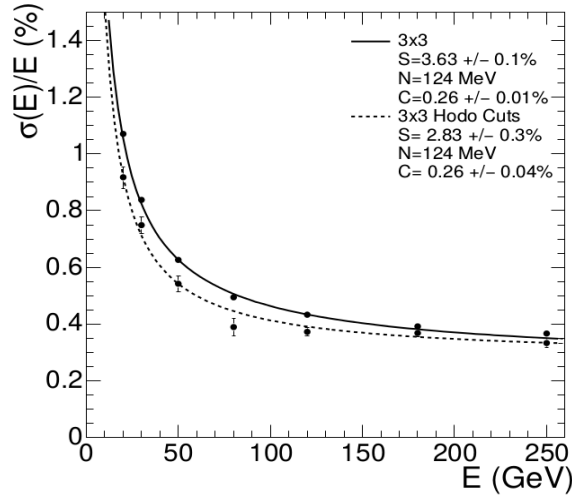


Figure 3.11: ECAL energy resolution as a function of electron energy as measured from a beam test.

3.2.4 Hadron Calorimeter

The CMS Hadron Calorimeter [10] is the third detector layer after the silicon-tracker and the ECAL calorimeter. Figure 3.12 describes the longitudinal view of the CMS detector showing hadron barrel (HB), hadron endcap (HE), hadron forward (HF) and outer (HO)

modules. The dashed lines in the figure represent fixed η values. The hadron calorimeter

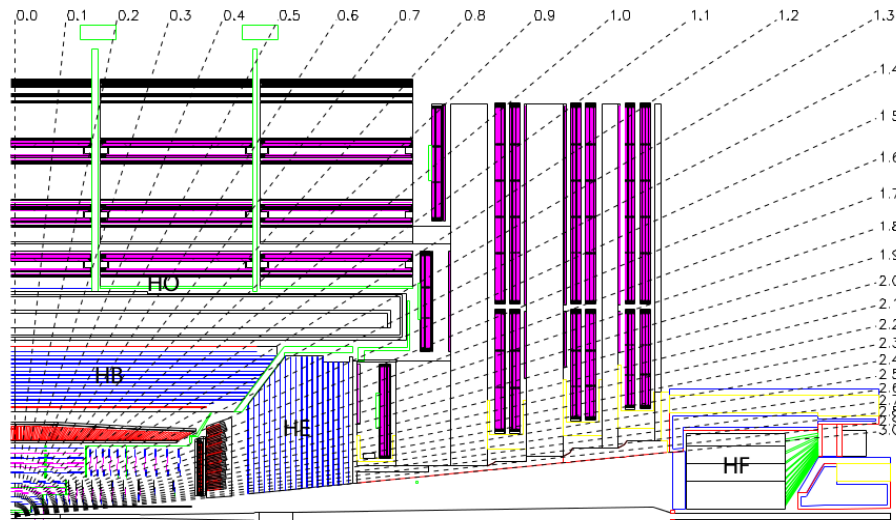


Figure 3.12: Longitudinal view of the CMS showing different parts of the hadron calorimeter: HB, HE, HF and HO.

barrel is radially bound between the outer extent of the ECAL ($R = 1.77\text{ m}$) and the inner extent of the solenoid ($R = 2.95\text{ m}$). It constrains the total amount of material which can be put in to absorb the hadronic shower. An outer hadron calorimeter or tail catcher is placed outside the solenoid complementing the barrel calorimeter. Beyond $|\eta| = 3$, the forward hadron calorimeters placed at 11.2 m from the interaction point extend the pseudorapidity coverage down to $|\eta| = 5.2$ using a Cherenkov-based, radiation-hard technology.

Figure 3.13 also illustrates a schematic quarter view of the hadron calorimeter system in the barrel, endcap and forward regions focussing on the layer depths and tower configurations. The central barrel part of the HCAL, namely the Hadron Barrel, consists of 32 towers in the pseudorapidity range $-1.4 < |\eta| < 1.4$, amounting to 2304 towers with the segmentation of $\Delta\eta \times \Delta\phi = 0.087 \times 0.087$. HB is constructed in two half barrels and is read out as a single longitudinal sampling. Each HB and HE tower has 17 scintillator

layers, except near the overlap region between HB and HE. The hadron outer detector

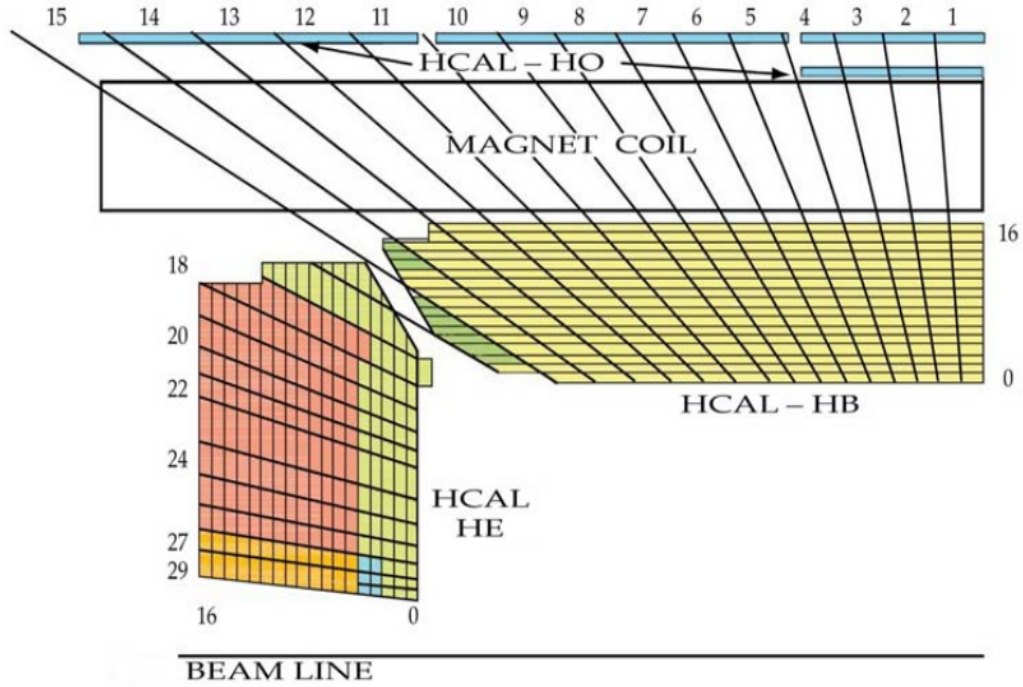


Figure 3.13: Another longitudinal view of the HCAL detector indicating the layer depths and tower configurations for HB, HE and HF. The signals of the tower segments with the same color are added optically, to provide the HCAL “longitudinal” segmentation.

(HO) samples the energy from penetrating hadron showers leaking through the rear of the calorimeters and so serve as a “tail-catcher” after the magnet coil. The effective thickness of the hadron calorimeter is increased to over 10 interaction lengths by adding this HO, thus reducing the tails in the energy resolution function. It also improves the E_T^{Miss} resolution in the calorimeter. Each hadron endcap (HE) of the HCAL has 14 towers in η direction covering a pseudorapidity range $1.3 < |\eta| < 3.0$, with a ϕ segmentation of 5° . The Hadron Forward (HF) detector provides a pseudorapidity coverage between $3.0 < |\eta| < 5.0$. The front face of the HF is located at 11.2 m from the interaction point, where the depth of the absorber is 1.65 m. The signal originates from Cerenkov light emitted in the quartz fibres, which is then channeled by the fibres to the photomultipli-

ers. The granularity of the sampling in the 3 parts of the HCAL has been chosen such that the jet energy resolution, as a function of E_T , is similar in all 3 parts.

3.2.5 Muon Detector

As the name of the detector suggests, detection of muons is one of the remarkable features of the CMS detector. Muon detection is a powerful tool for recognizing signatures of interesting processes over the very high background rate expected at the LHC with full luminosity. The $H \rightarrow ZZ \rightarrow 4\mu$ is called a Golden Channel as μ has very clean signature and are less affected than electrons due to radiative loss in the tracker material. Muon identification, momentum measurement and triggering are the three most important deliverables of the muon system. The high magnetic field and the iron return yoke ensures a good momentum resolution and triggering capability of the detector. CMS has 3 types of gaseous particle detectors for muon identification. Due to the shape of the solenoid magnet, the muon system was naturally driven to have a cylindrical, barrel section and 2 planar endcap regions. Each Endcap Detector consists of 4 discs that enclose both ends of the barrel cylinder. A schematic display of the muon system [11] is shown in Figure 3.14.

The barrel drift tube (DT) chambers, which cover the pseudorapidity region $|\eta| < 1.2$ and are organized into 4 stations interspersed among the layers of the flux return plates. The first 3 stations each contains 60 chambers, in 3 groups. A group of 4 chambers measure the muon coordinate in the $r - \phi$ bending plane, and other 4 chambers provide a measurement in the z direction, along the beam line. The fourth station does not contain the z -measuring planes. The 2 sets of 4 chambers in each station are separated as much as possible to achieve the best angular resolution. In the 2 endcap regions,

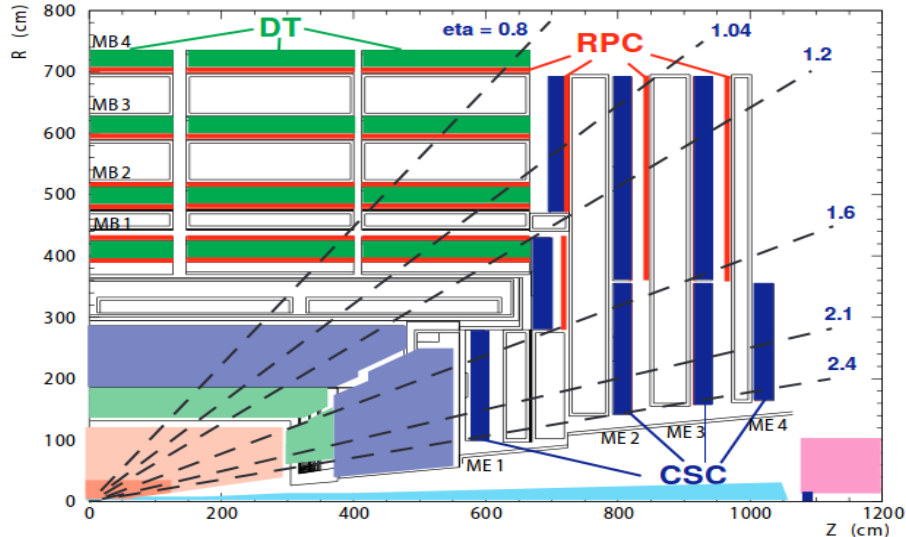


Figure 3.14: A schematic display of the muon system showing DT, RPC and CSC.

where the muon rates and background levels are high and the magnetic field is large and non-uniform, cathode strip chambers (CSC) are used. With their fast response time, fine segmentation, and radiation resistance, the CSCs identify muons between $|\eta|$ values of 0.9 and 2.4. There are 4 stations of CSCs in each endcap, with chambers positioned perpendicular to the beam line and interspersed between the flux return plates. The cathode strips of each chamber run radially outward and provide a precision measurement in the $r - \phi$ bending plane. In Figure 3.15 the muon transverse momentum resolution is shown for barrel and endcap regions. Optimal performance is achieved when the information from both tracker detector and muon system is used.

3.2.6 Trigger System

At the LHC, collisions are happening at a rate of 40 MHz. Depending on the instantaneous luminosity multiple interaction can happen in a particular bunch crossing. At the designed $10^{-34} \text{cm}^{-2} \text{sec}^{-1}$ luminosity, approximately 20 simultaneous collisions are

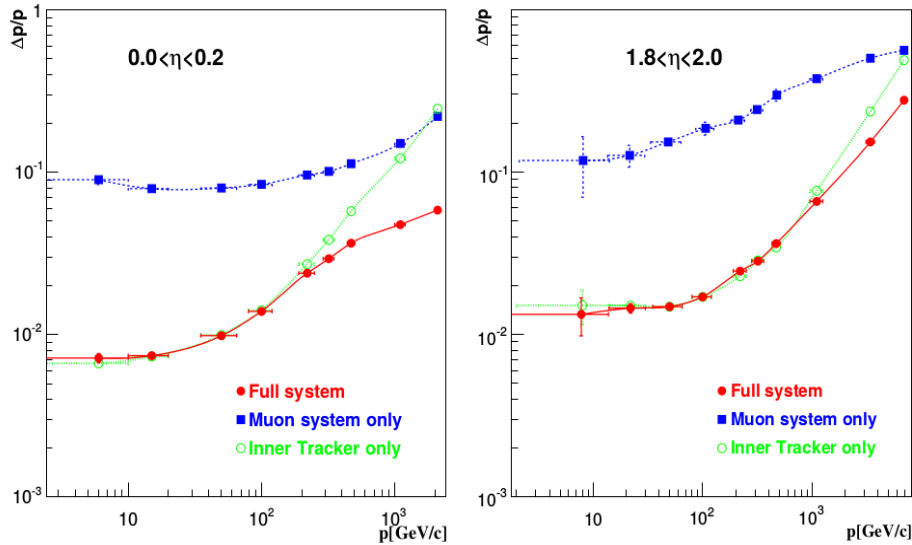


Figure 3.15: Muon transverse momentum resolution for barrel (left) and endcap (right) regions, comparing performance in muon and tracker system.

expected for proton-proton interaction. Practically, it is impossible to store and analyze this huge amount of data. Further, the rates of the interesting physics processes are quite low and a high performance trigger mechanism is needed to scale down inelastic event rates. CMS decided to have a two level trigger system; Level-1 trigger (L1) [12] and High Level Trigger (HLT) [13]. The Level-1 Trigger consisting of custom-designed, largely programmable electronics, brings down the rate to ~ 1 kHz. The HLT is software based and implemented in a computing cluster of about a thousand commercial processors, known as filter farm. The HLT further brings down the event rate to ~ 100 Hz.

The L1 Trigger uses coarsely segmented data from the calorimeters and the muon system, while holding the high-resolution data in pipelined memories in the front-end electronics. Figure 3.16 shows the two level trigger structure of the CMS Data Acquisition system. The Front End electronics has 128 pipelined memories which amounts to an L1 latency of $3.2 \mu\text{s}$, assuming 25 ns bunch crossing. Within this $3.2 \mu\text{s}$ an L1

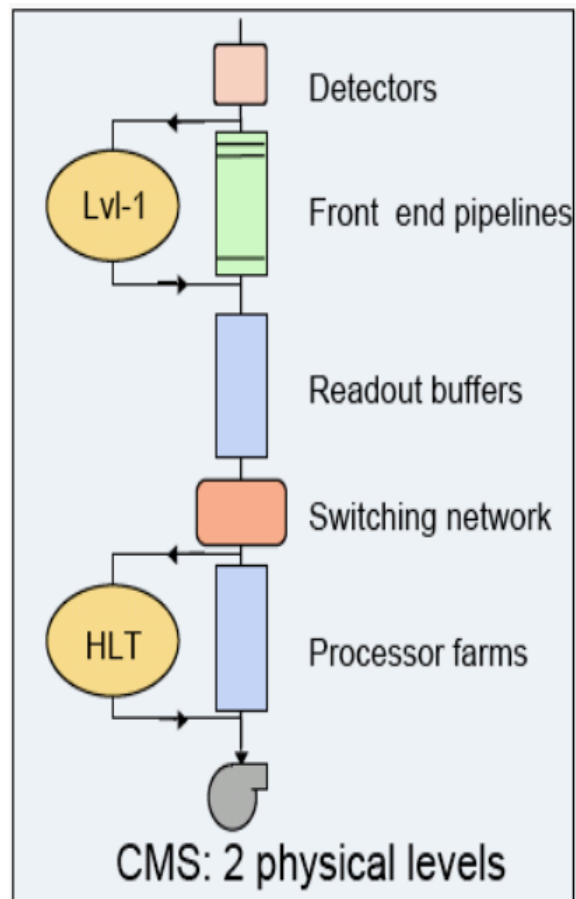


Figure 3.16: An illustration of the CMS Data Acquisition System, showing the two physical trigger levels.

decision has to be made. The L1 Trigger has different components; local, regional and global. Figure 3.17 presents a schematic for the architecture of L1 Trigger. At the lower end, the Local Triggers, also called Trigger Primitive Generators (TPG), are based on energy deposits in calorimeter trigger towers and track segments or hit patterns in muon chambers, respectively. Regional Triggers combine their information and use pattern logic to determine ranked and sorted trigger objects such as electron or muon candidates in limited spatial regions. The rank is determined as a function of energy or momentum and quality, which reflects the level of confidence attributed to the L1 parameter measurements, based on detailed knowledge of the detectors and trigger electronics and on the amount of information available. The Global Calorimeter and Global Muon Triggers determine the highest-rank calorimeter and muon objects across the entire experiment and transfer them to the Global Trigger, the top entity of the Level-1 hierarchy.

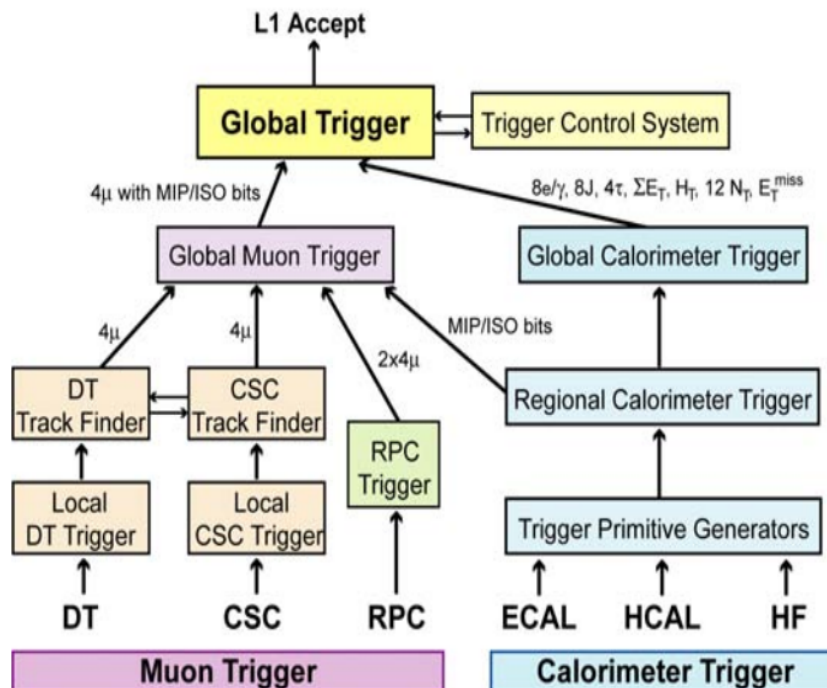


Figure 3.17: Architecture of the CMS Level 1 Trigger

The HLT has access to the complete read-out data from the front-end electronics with full granularity. The main idea is that each HLT trigger path is a sequence of reconstruction and selection steps of increasing complexity. Complex calculations are performed similar to those in offline analysis to decide on an event quality. HLT starts from the L1 candidate, and then improves the reconstruction and filtering process by exploiting also the tracker information. The starting selection based on the L1 information allows to reduce the rate before CPU intensive tracking reconstruction is performed. In fact, the most challenging aspect is that the CMS high level trigger has to maximize the efficiency while, at the same time, keeping the CPU-time (not only the rate) acceptable.

Bibliography

- [1] “The LHC Machine”, JINST 03 2008 S08001
- [2] ATLAS Collaboration, “The ATLAS Experiment at the CERN Large Hadron Collider”, JINST 03 2008 S08003
- [3] CMS Collaboration, “The CMS Experiment at the CERN LHC”, JINST 03 2008 S08004
- [4] ALICE Collaboration, “The ALICE experiment at the CERN LHC”, JINST 03 2008 S08002
- [5] LHCb Collaboration, “The LHCb Detector at the LHC”, JINST 03 2008 S08005
- [6] CMS collaboration, “The CMS magnet project: technical design report”, CERN-LHCC-97-010
- [7] A. Herve, “The CMS detector magnet”, IEEE Trans. Appl. Supercond. 10 (2000) 389.

-
- [8] CMS collaboration, “The CMS tracker system project: technical design report”, CERN-LHCC-98-006
 - [9] CMS collaboration, “The electromagnetic calorimeter project: technical design report”, CERN-LHCC-97-033
 - [10] CMS collaboration, “The hadron calorimeter project: technical design report”, CERN-LHCC-97-031
 - [11] CMS collaboration, “The CMS muon project, technical design report”, CERN-LHCC-97-032
 - [12] CMS collaboration, “The TriDAS project, technical design report. Volume 1: The level-1 trigger”, CERN-LHCC-2000-038
 - [13] CMS collaboration, “The TriDAS project, technical design report. Volume 2: Data acquisition and high-level trigger technical design report”, CERN-LHCC-2002-026,

Search for the Standard Model Higgs boson

4.1 Introduction

A search for the SM Higgs boson decaying to a pair of τ leptons has been performed using the data collected in 2011, 2012 & 2015 by the CMS Experiment at the LHC. τ is the heaviest member in the lepton family and has the shortest lifetime [1]. It decays to e , μ or hadrons (mostly pions) before reaching the detector. Figure 4.1 shows all the possible decay modes of a τ lepton pair. As can be seen from the figure, the double hadronic mode has the highest branching ($\sim 41\%$) followed by the semi-leptonic decays, namely $e\tau$ and $\mu\tau$ final states, where one of the τ leptons decays to either an e or a μ and the other one decays hadronically.

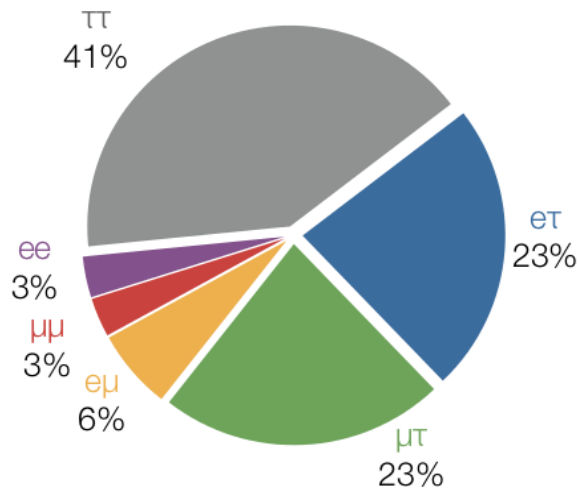


Figure 4.1: Decay modes of τ lepton pair, with relative fraction.

The focus of the present study is to look into the production mode where the Higgs boson is produced in association with a W boson which subsequently decays to a highly energetic μ and a neutrino. The study extends the coverage of the overall $H \rightarrow \tau\tau$ search. In this chapter two search channels in the associated production process will be described in details, namely,

- $WH \rightarrow \mu\tau_h\tau_h$: where both the τ leptons from the SM Higgs boson decay hadronically
- $WH \rightarrow \mu\mu\tau_h$: where one τ from the $H \rightarrow \tau\tau$ system decays to a μ while the other τ decays hadronically

It can be noted that in CMS tau indicates a hadronically decaying τ_h and leptonic decay modes are only visible as μ or e candidates.

4.2 $WH \rightarrow \mu\tau_h\tau_h$ Analysis

This channel looks for the SM Higgs boson produced in association with a W boson which decays to a highly energetic μ while the SM Higgs boson itself decays to a τ lepton pair, both of which subsequently decay hadronically. In other words, the final state of the channel is characterized by 3 leptons, one μ and two opposite sign τ 's. The Higgs boson mass is reconstructed from the τ pair. The analysis has been performed using a total integrated luminosity of 5 fb^{-1} at $\sqrt{s} = 7 \text{ TeV}$, 19.5 fb^{-1} at $\sqrt{s} = 8 \text{ TeV}$ and 2.1 fb^{-1} at $\sqrt{s} = 13 \text{ TeV}$, collected by the CMS detector during 2011, 2012 and 2015 respectively.

4.2.1 Data and Monte Carlo Samples

4.2.1.1 Data

Events where at least one muon at the trigger level satisfies threshold conditions on transverse momentum, detector acceptance and optionally isolation are analyzed. Datasets containing such events are termed as *Single Muon* datasets and are characterized by different trigger paths. Choice of the trigger path is the first and foremost step towards a sensitive analysis. A high efficiency trigger path with relatively low threshold and sharp turn-on response is essential for the SM Higgs search. CMS *Single Muon* trigger paths have been designed to satisfy these conditions. Data samples where all the sub-detector components have been certified as "Good" during data taking are used for the analysis. In Table 4.1, primary datasets recorded by the CMS detector in 2011 and 2012 with run ranges and amount of integrated luminosity have been listed.

SingleMu Datasets	Run Range	$\int \mathcal{L} \text{ pb}^{-1}$
/Run2011A-May10ReReco-v1	160431 - 163869	216 ± 5
/Run2011A-PromptReco-v4	165088 - 167913	955 ± 22
/Run2011A-05Aug2011-v1	170826 - 172619	383 ± 9
/Run2011A-03Oct2011-v1	172620 - 173692	707 ± 15
/Run2011B-PromptReco-v1	175860 - 180252	2714 ± 57
/Run2012A-13Jul2012-v1	190450 - 193680	801 ± 35
/Run2012A-06Aug2012recover-v1	190782,190895,190906,190945,190949	83 ± 4
/Run2012B-13Jul2012-v1	193752 - 196531	4446 ± 196
/Run2012C-24Aug2012-v1	198022 - 198523	495 ± 22
/Run2012C-PromptReco-v2	198941 - 203002	6401 ± 282
/Run2012D-PromptReco-v1	203894 - 208357	6752 ± 297

Table 4.1: Recorded CMS datasets in 2011 and 2012 analyzed with run range and corresponding integrated luminosity.

4.2.1.2 Signal

The signal Monte Carlo (MC) events are generated using dedicated event generators for Higgs boson masses ranging from 90 to 160 GeV/c^2 . During Run-1 Pythia6 [2] generated samples were used whereas during Run-2 in 2015 Powheg [3] generator has been used to take into account the Next-to-Leading Order (NLO) correction. As Powheg is only a matrix element generator, Pythia8 has been used for parton showering and hadronisation. In Run-1 $\sqrt{s} = 7$ & 8 TeV analyses WH-ZH- $t\bar{t}H$ combined signal was used to cover all the associated production processes. However, in Run-2 CMS recommends exclusive WH-only signal. Figure 4.2 portrays the generator level validation plots for the $W(H \rightarrow \tau\tau)$ signal process using 8 TeV Pythia6, 13 TeV Madgraph [4] and 13 TeV Powheg samples. For 13 TeV, the Next-to-Leading Order (NLO) generators are proposed instead of Pythia6 which is a Leading Order (LO) generator. As can be seen from the figure, comparison plots show a good agreement between the different generators and nothing unusual is found in the 13 TeV distributions.

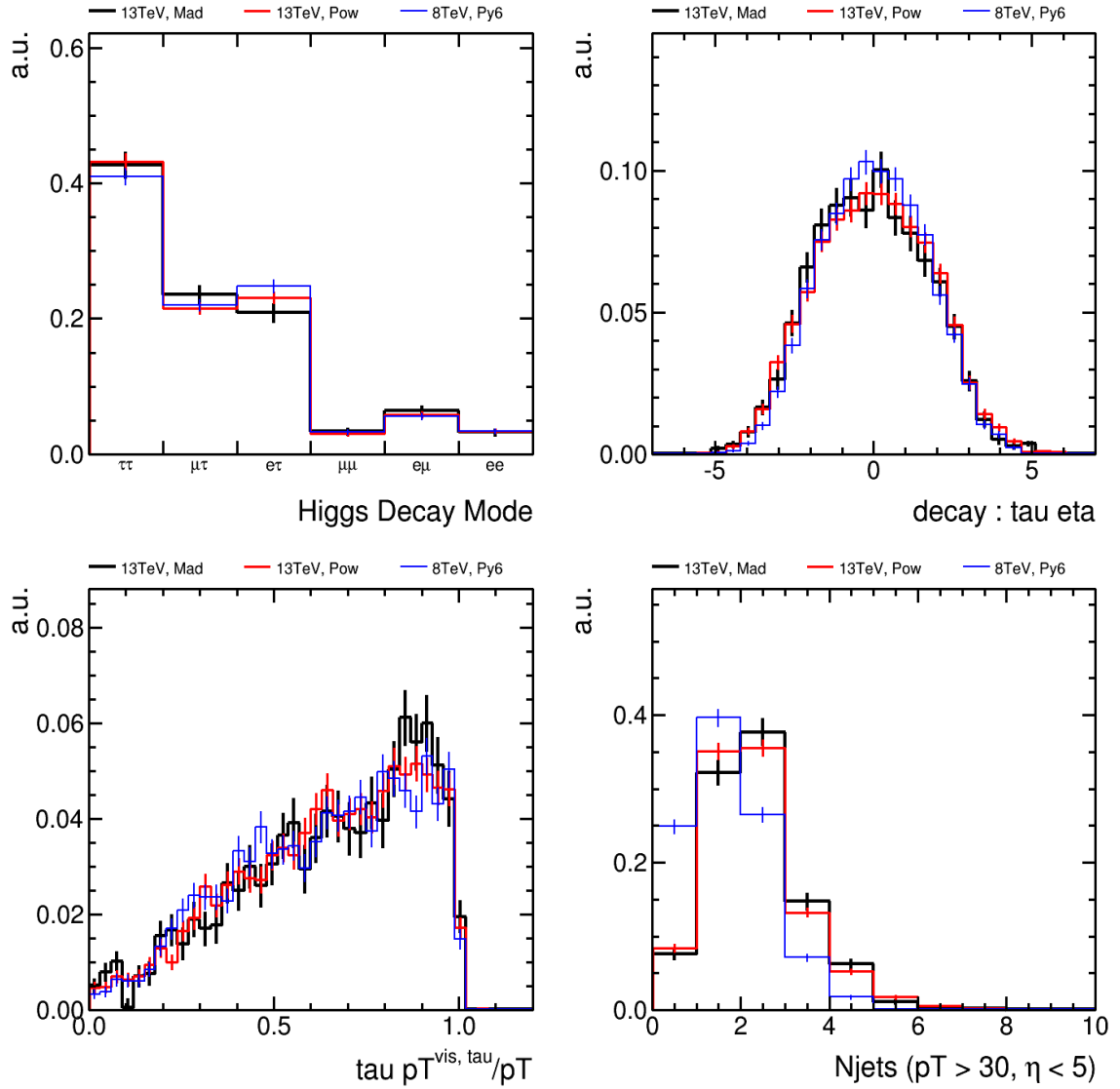


Figure 4.2: Comparison of generator level properties of the $W(H \rightarrow \tau\tau)$ signal process using 8 TeV Pythia6, 13 TeV Madgraph and 13 TeV Powheg samples.

In CMS, generated events are passed through a detailed simulation of the detector, based on GEANT4 [5], and are reconstructed using the same version of the CMS event reconstruction software as used for data.

4.2.1.3 Background

The processes that yield potentially non-negligible background contribution to the final sample of events satisfying all analysis level selection include $W + Jets$, $Z + Jets$, $t\bar{t}$, di-boson (WZ & ZZ) and QCD multi-jet production. The background contributions can be divided into two main categories - Irreducible and Reducible. Irreducible background contributions comprise of WZ, where all the final state objects come from real sources. ZZ can also be considered in this category because one lepton may either escape the detector acceptance or might not get reconstructed. The rest of the background sources are reducible in the sense that they contain at least one mis-identified light lepton or a mis-identified hadronically decaying τ candidate produced by a quark or gluon jet. The following reducible background processes have been considered in this analysis,

- $W + Jets$: This is the most dominant contributor. $W + Jets$ can mimic the signal process when W decays to a μ and two recoil jets are mis-identified as τ candidates.
- Drell-Yan + Jets: Drell-Yan + Jets can contribute to the final state in two different ways, (a) the decay chain $Z \rightarrow \tau\tau \rightarrow \tau_h\mu + X$ provides a real μ and a τ decaying hadronically while a recoil jet X is reconstructed as the other τ_h candidate and (b) events with $Z \rightarrow \mu\mu + X$ where one of the muons is mis-identified as a hadronic tau candidate, and the other tau candidate is a mis-identified recoil jet.
- $t\bar{t} + Jets$: Events where one W from the t decay produces a μ while the other W

from the second t decays to light quarks that can fake the τ_h candidates contribute to the fake τ_h background. However, the contribution can be suppressed largely by using a b-Jet veto.

- **ZZ:** Dominant contribution from the ZZ process can occur in the irreducible form as discussed earlier in the section. But ZZ can also contribute to the fake τ background where the second Z decays into a pair of jets mis-identified as two hadronic tau candidates.
- **WW:** The main contribution is due to events where one W decays into a μ and a neutrino, while the other one decays into a pair of quark jets mis-identified as τ_h candidates. Other possibilities include cases where the second W decays into a hadronically decaying τ lepton and a recoil jet is mis-identified as the second τ_h candidate.
- **QCD multi-jet:** The contribution of these events to the final sample is negligible due to the high p_T threshold for the μ and two hadronic τ candidates. The events can satisfy analysis selections if a light lepton (μ) is produced in semi-leptonic heavy flavor quark decays and the τ_h candidates are due to mis-identified quark or gluon jets.

The di-boson background sources are simulated using Pythia6. The Drell-Yan and $t\bar{t}$ samples are simulated using Madgraph for the hard scattering part while Pythia is used to describe parton showering and fragmentation of partons into jets. In all cases, the τ -lepton decays are generated with Tauola [6] to ensure the most accurate description of branching fractions and the kinematics of the τ lepton's decay products.

4.2.2 Pile-Up Reweighting

At the LHC, protons collide in bunches. When these bunches collide with each other at the centre of the CMS detector, usually more than one collisions take place. Interaction vertices other than the hard scattered event vertex are called pile-up vertices. Pile-up interactions are simulated by superimposing minimum bias events, generated using Pythia, onto the hard scattering event. The multiplicity of pile-up interactions in the simulation is sampled from a distribution that does not exactly reproduce the one observed in data. To match the pile-up conditions in data, every Monte Carlo event simulated with $\langle N_{mc} \rangle$ pile-up interactions is assigned a weight equal to the ratio between the probability of observing $\langle N_{data} \rangle$ in data and $\langle N_{mc} \rangle$ in the simulation. Figure 4.3 presents the distribution of number of primary vertices in the event from data and Monte Carlo, where the Monte Carlo distribution has been scaled by a weight factor, $\frac{\langle N_{data} \rangle}{\langle N_{mc} \rangle}$.

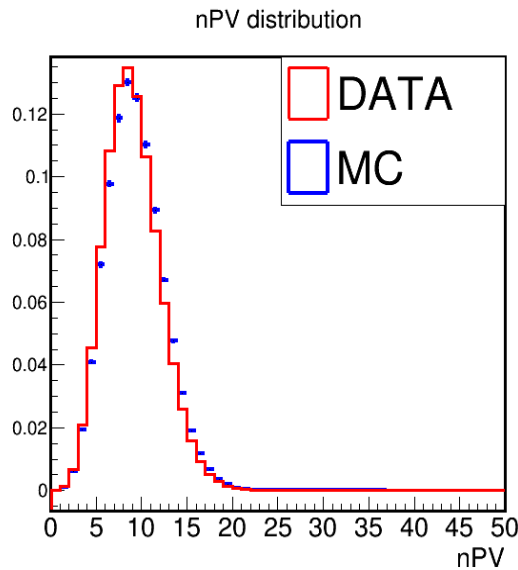


Figure 4.3: Number of Primary Vertices for data and MC at $\sqrt{s} = 13$ TeV, where the MC distribution has been scaled by the pile-up reweight factor to match the data distribution.

4.2.3 Baseline Selection

As discussed earlier, the experimental signature of the $WH \rightarrow \mu\tau_h\tau_h$ channel is marked by the presence of a highly energetic μ coming from the W boson and two hadronically decaying τ 's from the Higgs boson. Event selection is designed to take advantage of the signal event characteristics while maximizing rejection of the background contribution. The selection process requires presence of at least one μ candidate reconstructed using one of the standard CMS algorithms and at least two hadronically decaying τ candidates reconstructed using the Hadrons Plus Strips (HPS) algorithm, which relies on the CMS Particle Flow (PF) framework [7–9]. Following selection of a high quality μ and the τ candidates, a series of topological selection conditions is used to further reduce background contamination and improve the sensitivity of the analysis. The details of the selection are described below.

4.2.3.1 Trigger Requirement

During Run-1, the trigger paths $HLT_IsoMu24$ and $HLT_IsoMu24_eta2p1$ were used to select the events. These trigger paths come with a trigger level transverse momentum requirement of $24 \text{ GeV}/c$ and muon isolation. $HLT_IsoMu24_eta2p1$ has further constraint on $\eta (\leq 2.1)$ to reduce the rate for the trigger path. None of these paths was available as un-prescaled throughout the entire Run-1 data taking. However, together they covered the entire period suitably without any prescale. In Run-2 analysis at 13 TeV, $HLT_IsoMu20$ is used as the trigger path. The ability to keep the threshold lower is always beneficial for Standard Model physics analysis. Muon High Level Trigger (HLT) efficiencies are estimated using 13 TeV data and MC samples and are shown in Figure 4.4. As expected, the $HLT_IsoMu20$ trigger path has a very high efficiency

and shows a sharp turn-on around 20 GeV. The difference between the efficiencies for data and MC are accounted for by a data/MC scale factor while comparing event yield.

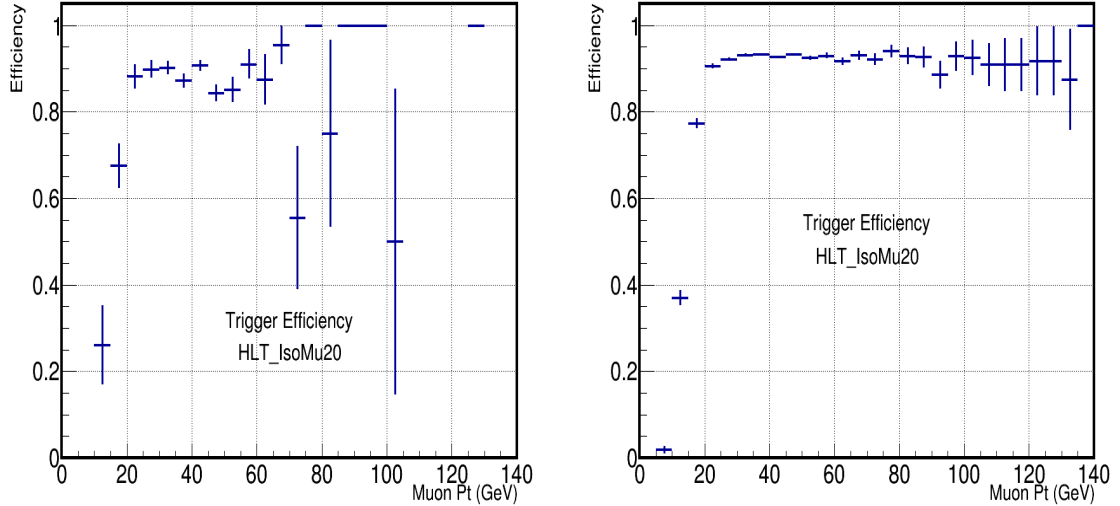


Figure 4.4: High Level Trigger (HLT) efficiency for muons at $\sqrt{s} = 13$ TeV **DATA** (left) and **MC** (right).

4.2.3.2 Event Vertex Selection

The primary vertex of the hard scattering process is selected using a dedicated algorithm [10, 11]. Firstly, the distance of a reconstructed vertex from the nominal interaction point is required to be less than 24 cm along the beam-line (the global CMS z direction) and less than 2 cm in the transverse plane. The number of degrees of freedom of the vertex fit is required to be smaller than 4. Out of all the reconstructed vertices satisfying the above selection, the one with the highest sum of square of the p_T values of the tracks associated to that vertex is chosen as the vertex corresponding to the hard scattering process. All other vertices are considered to come from additional soft

scattering collisions in the same bunch-crossing i.e pile-up.

4.2.3.3 Muon Selection

4.2.3.3.1 Identification

Muons are reconstructed using information from the tracker system and the Muon chamber hits. Reconstructed muons are required to have a $p_T > 24 \text{ GeV}/c$ and $|\eta| < 2.1$, as a fiducial selection. Muons are further required to pass the following selection criteria,

- at least one muon chamber hit included in the global-muon track fit;
- muon segments in at least two muon stations;
- the impact parameter of the inner track in the transverse plane with respect to the reconstructed primary vertex is required to be $|d_0| < 0.02 \text{ cm}$;
- the longitudinal impact parameter $|dz| < 0.2 \text{ cm}$ with respect to the reconstructed primary vertex;
- the global track fit is required to have $\chi^2/Ndf < 10$;
- hits in more than 5 layers of the inner tracker;
- atleast one hit in the pixel detector.

The above selection conditions ensure a high signal efficiency with small fake rate. Requirement against the primary vertex in the transverse and longitudinal plane reject cosmic muons.

A more detailed description of muon identification and performance studies are available here [12]. Figure 4.5 presents a comparison of Muon ID efficiencies for Tight and Medium working points. As expected, Medium ID working point shows a little higher efficiency than the Tight one for a comparable fake rate. During the 7 & 8 TeV analyses, the Tight working point was the recommended choice, but for 13 TeV, the Medium working point has been chosen for better performance.

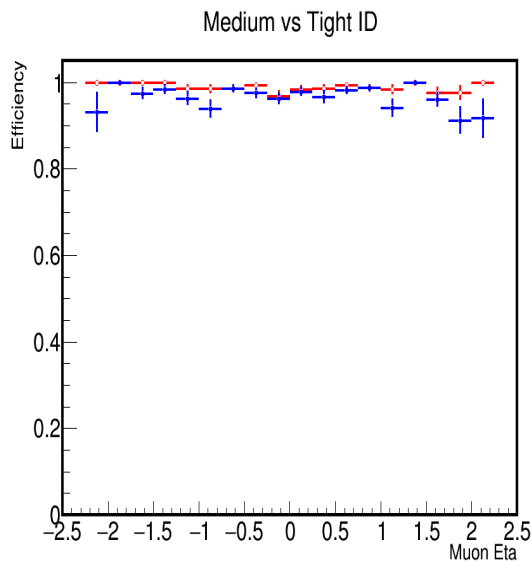


Figure 4.5: Comparison of Muon Identification efficiency for **Medium** and **Tight** working points as a function of Muon η using $\sqrt{s} = 13$ TeV data.

4.2.3.3.2 Muon Isolation

To reduce contamination from muons originating from b or c-quark decays within jets or decays in flight, the selected muons are required to be isolated.

Particles reconstructed by the PF algorithm are used to calculate the isolation deposits around a muon. The isolation variable is constructed using charged hadrons,

photons and neutral hadrons in a cone around the muon. All charged hadrons are considered, while photons and neutral hadrons are required to have $E_T > 0.5$ GeV for them to be considered in the isolation sum. The isolation variable sums up particles in a cone of $\Delta R = 0.4$ around the muon axis.

The isolation sum is corrected for contributions originating from pile-up vertices. Pile-up correction on charged hadron contribution can be easily estimated by applying a z -vertex requirement on the candidates. But it is difficult to estimate and subtract the neutral contribution coming from the pile-up.

An algorithm known as the $\Delta\beta$ correction technique has been used for this purpose. The correction, applied on an event-by-event basis, predicts the expected contribution to the isolation sum from neutral particles not associated with the primary hard interaction by exploiting the relative contribution between the charged and neutral hadrons inside the isolation cone. Pile-up corrected $\Delta\beta$ isolation is defined as,

$$I_{Rel}^{PF}(\Delta\beta) = \sum (p_T^{charged} + \max(E_T^{gamma} + E_T^{neutral} - \Delta\beta * E_T^{PU}, 0.0)), \quad (4.1)$$

where $p_T^{charged}$ is the sum of the charged hadrons that are inside the isolation cone and originate from the primary vertex while E_T^{gamma} & $E_T^{neutral}$ are the γ and neutral hadron contribution inside the isolation cone, respectively. E_T^{PU} corresponds to the charged hadron p_T sum from pile-up vertices and $\Delta\beta$ is set to 0.5 for muon isolation.

4.2.3.4 Tau Selection

4.2.3.4.1 Reconstruction

Tau, the heaviest member of the lepton family, decays to lighter leptons or hadrons shortly after production. Tau leptons have a lifetime of 2.9×10^{-13} s and a mass of $1776.82 \text{ MeV}/c^2$. Various decay modes of the τ lepton are summarized in Table 4.2. As

Decay Mode	Resonance	Br(%)
$\tau^- \rightarrow e^- \bar{\nu}_e \nu_\tau$		17.8
$\tau^- \rightarrow \mu^- \bar{\nu}_\mu \nu_\tau$		17.4
$\tau^- \rightarrow h^- \nu_\tau$		11.5
$\tau^- \rightarrow h^- \pi^0 \nu_\tau$	$\rho(770)$	26.0
$\tau^- \rightarrow h^- \pi^0 \pi^0 \nu_\tau$	$a_1(1260)$	10.8
$\tau^- \rightarrow h^- h^+ h^- \nu_\tau$	$a_1(1260)$	9.8
$\tau^- \rightarrow h^- h^+ h^- \pi^0 \nu_\tau$		4.8
other hadronic modes		1.8

Table 4.2: Branching fraction of different τ decay modes. h^\pm denotes charged pion or kaon.

can be seen from the above table, τ leptons decay hadronically in about two thirds of the cases, either to one or three charged pions or kaons plus up to two neutral pions and one neutrino. The pions decay instantaneously to $\gamma\gamma$. In one third of the cases τ leptons decay into an electron or muon plus two neutrinos. It is not possible to distinguish the electrons or muons originating from τ decays from electrons and muons coming out from the primary proton-proton interactions. They will be reconstructed by the standard CMS reconstruction algorithms used for electrons and muons. Particle Flow algorithm reconstructs the four-momentum of the τ lepton by summing up the four-momentum of all the particles with $p_T > 0.5 \text{ GeV}/c$ inside the signal cone around the leading charged hadron as shown in Figure 4.6. The leading charged hadron is also required to be within the matching cone around the jet axis. Tau isolation is computed

using the particles within the isolation cone around the leading candidate. Hadronically

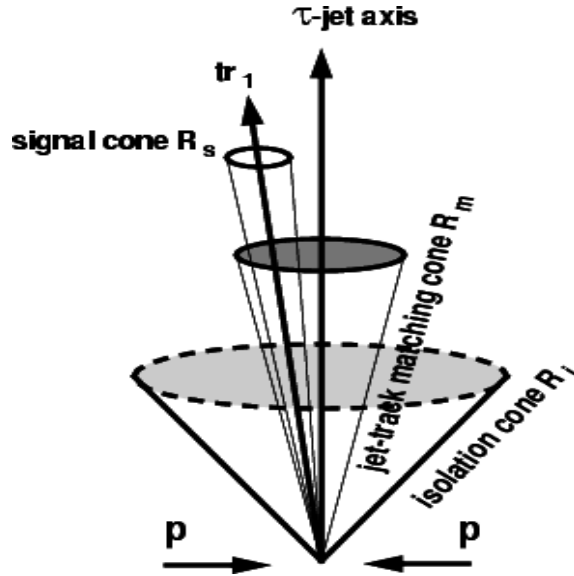


Figure 4.6: τ jet reconstruction using Particle Flow

decaying τ leptons are reconstructed using Hadron Plus Strip (HPS) algorithm [13, 14]. HPS tries to combine the PF charged hadrons with the nearby clusters of photons to take into account the additional π^0 's. The clustering of the photons is performed in η -strips and is needed to correctly account for photon conversion happening in the outer part of the tracker. In this case, the conversion e^+e^- pairs bend in the magnetic field. Since the conversion happens late and there are not enough tracker hits to form a track, the conversion electrons are reconstructed as photons with very similar η . If the conversion electrons radiate, additional photons may appear on the same η -strip. The four allowed categories of the reconstructed τ_h candidates are :

- h^\pm : A single charged hadron without any strips;
- $h^\pm\pi^0$: One prong decay with single $\eta - \phi$ strip;
- $h^\pm\pi^0\pi^0$: One prong decay with two $\eta - \phi$ strips;

- $h^\pm h^\mp h^\pm$: Three prong decays dominated by $a_1 \rightarrow \pi\pi\pi$.

Once reconstructed, a set of further identification criteria is imposed to separate the hadronic taus from jets, electrons or muons.

4.2.3.4.2 Isolation

To better separate hadronically decaying tau candidates (τ_h) from quark and gluon jets mis-identified as τ_h , each candidate is required to be well isolated using one of the standard HPS working points. The isolation sum is calculated using the charged and neutral PF-candidates in the isolation cone around the reconstructed *tau*-jet axis. This sum is corrected against the contribution coming from pile-up by the recommended $\Delta\beta$ technique, like what has been done for Muons. The formula in Eq. 4.1 is used to calculate the $\Delta\beta$ corrected isolation sum. Three standard working points are defined based on the value of the isolation sum corrected for the contamination due to particles from pile-up:

- Loose Combined Isolation: $I(\Delta\beta) < 2 \text{ GeV}$.
- Medium Combined Isolation: $I(\Delta\beta) < 1 \text{ GeV}$
- Tight Combined Isolation: $I(\Delta\beta) < 0.8 \text{ GeV}$

4.2.3.4.3 Discrimination against Muon and Electron

To distinguish genuine τ_h from muon or electron additional discriminator working points have been defined and implemented as built-in types of the HPS τ_h -candidate. The following working point types are defined to discriminate a real τ_h against a muon.

- Loose: Requires that no track segments in the muon detector should be matched to the PF charged hadron candidate with the highest p_T .
- Medium: Requires that no hits in the muon detector should be matched to the PF charged hadron candidate with the highest p_T .
- Tight: Requires that no hits in the muon detector should be matched to the PF charged hadron candidate with the highest p_T . In the Single Hadron category it is further required that the ratio of the sum of the energy deposits in the hadronic and electromagnetic calorimeter associated to this candidate over the track momentum of the candidate should be larger than 0.2, which is designed to reject candidates consistent with a minimum ionizing particle (MIP).

Similarly, two different approaches are adopted to build the discriminator against an electron, (a) a cut-based discriminator with three different working points, (b) an MVA-based discriminator.

- Loose: a cut on the standard MVA-based PF electron/pion discriminator.
- Medium: cut on the standard MVA-based PF electron/pion discriminator is tightened, and candidates pointing into the crack between the barrel and endcap components of the CMS electromagnetic calorimeter are discarded from further consideration.
- Tight: in addition to the MVA-based requirement, candidates are required to satisfy two additional selections to reduce the probability of an electron being misidentified as a tau further. The first selection rejects candidates in the "Single Charged Hadron" category (a single track and no reconstructed π^0 candidates),

which has too little energy deposit in the hadron calorimeter given the track momentum. The second selection rejects highly radiating electrons mis-identified as the "Single Charged Hadron Plus One Strip" decay mode.

- MVA based discriminator: another option available to reduce contamination of electrons mis-identified as tau candidates is based on the output of a multivariate Boosted Decision Tree (BDT). The τ_h candidates are categorized on the basis of the number of neutral PF candidates being part of the reconstructed τ_h candidate (0 or ≥ 1), pseudorapidity ($|\eta| < 1.5$ or $|\eta| > 1.5$) and presence of a Gaussian Sum Filter(GSF) track associated with the leading charged hadron candidate. Depending on the decay mode category, the BDT is trained on a dedicated set of variables based on tracking and calorimetric information.

As the analysis deals with two τ_h candidates in the final states, they are selected separately to increase the sensitivity of selection. Both the τ_h candidates are required to pass the following selections:

- $p_T > 20 \text{ GeV}/c$
- $|\eta| < 2.3$
- HPS Decay Mode
- Loose Combined Isolation with $\Delta\beta$ correction
- Loose Electron rejection
- Tight Muon rejection

Further the τ_h candidate with opposite sign to the μ (τ_h^{OS}) should have:

- Minimal separation in the $\eta - \phi$ plane with respect to the selected μ : $\Delta R(\tau_h^{OS}, \mu) \geq 0.5$
- $|Z_{\tau_h^{OS}} - Z_\mu| < 0.14$ cm, where $Z_{\tau_h^{OS}}$ is the Z-position of the τ leg which is of opposite sign to the selected μ and Z_μ is the Z-position of the μ .

Similarly the τ_h with the same charge (τ_h^{SS}) to the μ is further required to have:

- Minimal separation in the $\eta - \phi$ plane with respect to τ_h^{SS} and μ : $\Delta R(\tau_h^{OS}, \tau_h^{SS}) \geq 0.5$ and $\Delta R(\tau_h^{SS}, \mu) \geq 0.5$
- $|Z_{\tau_h^{SS}} - Z_\mu| < 0.14$ cm, where $Z_{\tau_h^{SS}}$ is the Z-position of the τ leg which is of same sign to the selected μ and Z_μ is the Z-position of the μ .

It should be noted that in the optimized scenario both the τ_h 's are selected by similar requirement except for isolation which is relatively tighter for the τ_h^{SS} leg. This feature is intentional and will be discussed in the next section when the background rejection will be discussed.

4.2.3.5 Topological Selection

The following selection conditions define the final state topology of the search channel and optimize selection efficiency and background contamination.

- Two τ_h 's must be of opposite sign;

- At least one of the two τ_h s should have a $p_T > 25 \text{ GeV}$, i.e. $\max(p_T^{\tau_h^{OS}}, p_T^{\tau_h^{SS}}) > 25 \text{ GeV}/c$;
- b-Jet Veto: The t quark predominantly decays into a W boson and a b-quark (identified at the reconstruction level as a b-tagged jet), hence the t-pair production process can lead to events with topology similar to that of signal events. In order to reduce the contamination due to $t\bar{t}$ events, events with one or more b-jets with $p_T > 20 \text{ GeV}$, $|\eta| < 2.4$ are excluded from further consideration. In this analysis the combined secondary vertex discriminator [15] is used. This discriminator combines information about impact parameter significance, the secondary vertex and jet kinematics. The medium working point is used to tag a jet as a likely b-quark.
- E_T^{Miss} cut: the final state is characterized by a certain amount of missing energy in the transverse plane due to escaping neutrinos. Thus only events with $E_T^{Miss} \geq 20 \text{ GeV}/c$ are kept for further analysis.
- μ Veto: the $Z/\gamma^* \rightarrow \mu^+ + \mu^-$ process accompanied by additional jet production can mimic the signal events. However, the contribution can be easily removed by applying a veto against the presence of an additional muon. If a second muon is found with $p_T > 15 \text{ GeV}/c$ and $|\eta| < 2.1$ coming from the same primary vertex as the OS τ_h ($|Z_{\tau_h^{OS}} - Z_\mu| < 0.14 \text{ cm}$) the event is discarded.
- electron Veto: for similar reasons, if an electron with $p_T > 10 \text{ GeV}/c$ and $|\eta| < 1.4442$ or $1.566 < |\eta| < 2.1$ passing the tight electron ID and compatibility with the Z-position of the primary vertex is found, the event is rejected.
- Overlap Removal: The transverse mass M_T formed by the muon and the missing transverse energy vector is required to be $\geq 20 \text{ GeV}$ to ensure that there is no event overlap with the $\mu\tau_h$ channel of the $H \rightarrow \tau\tau$ analysis in CMS and therefore allows the two channels to be easily combined.

4.2.3.6 Background Supression using a Multivariate BDT

After the objects are selected and event vetoes are applied, the dominant background contribution in the channel comes from events containing mis-identified or fake τ_h candidates. To suppress fake background further, a multivariate Boosted Decision Tree (BDT) [16] is trained to discriminate signal events containing real τ leptons from fake background. The following kinematic variables have been used as input to the BDT:

- p_T of the τ_h candidate same sign to the μ : $p_T^{\tau_h^{SS}}$,
- p_T of the τ_h candidate opposite sign to the μ : $p_T^{\tau_h^{OS}}$,
- Missing transverse energy, E_T^{Miss} in the event,
- Separation of the two τ 's in the $\eta - \phi$ plane; $\Delta R(\tau_h^{OS}, \tau_h^{SS})$,
- p_T ratio; $\frac{p_T^{\tau_h\tau_h}}{(p_T^{\tau_h^{OS}} + p_T^{\tau_h^{SS}})}$.

The above kinematic variables do not heavily depend on the Higgs mass or the tau candidate isolation, thus justifying the choice of the training samples in the signal region where all the available Higgs samples with different mass points are combined to get sufficient statistics. The BDT has been trained with the signal Monte Carlo events where it has three isolated leptons in the final state. Collision data are used to train the BDT for the background events, where both the τ_h are anti-isolated. Finally an optimized cut on the BDT value is applied for background suppression.

4.2.4 Background Estimation

The background contribution surviving all the selection conditions contains both irreducible and reducible components. As discussed earlier, the irreducible background comes from WZ & ZZ events which contain three real isolated leptons (μ and two τ_h) in the final state. The reducible background contains at least one quark or gluon jet which is incorrectly identified as an isolated τ_h .

4.2.4.1 Irreducible Background

The irreducible WZ and ZZ diboson backgrounds are estimated using Pythia, and normalized using the NLO theoretical prediction. WZ events have the same signature as that of the signal events. The Z mass is close to the region of interest for the low mass SM Higgs search. CMS measurements of the WZ and ZZ cross sections [17] using 2011 and 2012 data were found to be compatible with the NLO predictions. The WW diboson background contains only two isolated leptons in the final state and is therefore estimated using the fake rate method.

4.2.4.2 Reducible Background

The main sources of background events are due to $W + Jets$ and $Z + Jets$ processes, where at least one jet or its constituents are mis-identified as an isolated lepton. Fake non-prompt light leptons arise from the semi-leptonic decays of heavy flavor quarks, decays in flight, mis-identified hadrons, and electrons from photon conversions. The mis-identification probabilities are driven by the performance of the jet fragmentation

models in describing rare fluctuations in the regime that is far from the design limits of applicability of such models. Even though physics and detector simulation is fairly accurate, relying on simulation in predicting the mis-identification probabilities may introduce a large uncertainty. Instead, a robust data-driven approach based on the fake rate calculation is a preferable choice.

In order to estimate the background arising from mis-identification of a particular object, one performs an extrapolation from a background rich sample selected with a loose requirement on the object in question, into the signal region where the same object is selected with tighter conditions. The extrapolation is performed by scaling the distribution obtained in the background enriched **Side Band** region with the fake rate. The fake rate is frequently chosen to be dependent on the object p_T and other kinematics characteristics and is measured in another sample, which is known to be heavily dominated by mis-identified objects independent of whether one chooses to apply the loose or tight selection. The fake rate is calculated as the probability for a fakeable object to satisfy all the standard identification criteria. In order to account for various physics effects, this probability is parameterized as a function of various kinematic quantities such as object p_T . Care must be taken to ensure that the sample in which the fake rate is measured and the one where it is applied are sufficiently similar topologically as mis-identification probabilities are not topology independent. Alternatively, one can parameterize the fake rate to include quantities sensitive to the event topology, e.g. closeness of the fakeable object to another jet etc.

The fake contribution to the final state can be identified in two categories, (a) $Z + Jets$ class, where there are two real objects in the final state and one fakeable object ($Jet \rightarrow \tau_h$), (b) $W + Jets$ class, where there is only one real object in the final state coming from W decay and two jets fake two τ_h . Remaining reducible background

processes like $t\bar{t}Jets$, QCD, WW are also covered by this scheme. $t\bar{t}Jets$ falls in both the categories, where it can have either one jet fake or two jets fake ($jet \rightarrow \tau_h$) in the final state. QCD and WW need to have both the jets fake ($jet \rightarrow \tau_h$) in order to pass the selection. In Table 4.3, the breakdown of background contribution in terms of **Real** and **Fake** (Fakeable) objects, are shown.

Process	Final State		
	μ	τ_h^{OS}	τ_h^{SS}
$Z \rightarrow \mu\tau_h + Jets$	Real	Real	Fake
$W \rightarrow \mu + Jets$	Real	Fake	Fake
$t\bar{t} + Jets$	Real	Fake	Fake
$t\bar{t} + Jets$	Real	Real	Fake
WW	Real	Fake	Fake
QCD	Fake	Fake	Fake

Table 4.3: Fake objects in the final state from different background sources.

The data-driven fake rate estimation works in the following way:

- A background enriched region is selected. In this region the probability $f(p_T)$ for a jet to pass the final τ_h selection, parametrized as a function of the p_T of the τ_h , is measured.
- The fake background estimation is performed by defining a **Side Band** region by selecting events using standard selection except that the tau candidate which has the same charge as the muon is not required to be isolated. In other words, the candidate is the fakeable object.
- Each event in the **Side Band** region is weighted by the corrected probability $w(p_T) = \frac{f(p_T)}{1-f(p_T)}$. The resulting weighted spectrum is the estimate for the expected background contribution in the signal region due to jets mis-identified as tau candidates.

4.2.4.2.1 Measurement of the $Jet \rightarrow \tau_h$ Fake Rate

The probability of a quark or gluon jet to be mis-identified as an isolated τ_h candidate is known as $Jet \rightarrow \tau_h$ Fake Rate. The Fake Rate is measured as a function of tau p_T in two separate control regions, one enriched with $W + Jets$ and the other with $Z + Jets$ events. With the exception of the isolation, the τ_h candidates must fulfill the same requirements as used in the main analysis.

The $W + Jets$ measurement region is selected as follows :

- Exactly one isolated tight PF muon with $p_T \geq 24 \text{ GeV}/c$ and $|\eta| \leq 2.1$;
- At least two τ_h candidates of the same sign charge and also the same sign with the muon. The two τ_h s are required to be of same sign to avoid having signal events in this control region. Furthermore, the same sign requirement of the τ_h pair to the muon is imposed since the fake rate is only applied on the τ_h leg which is of same sign to the muon, as argued in the previous section;
- The transverse mass between the muon and the missing transverse energy, M_T , fulfills $M_T \geq 40 \text{ GeV}/c^2$. This is important to increase the purity of the $W + Jets$ events as M_T is expected to be high W decay;
- The longitudinal impact parameter of the tag muon track with respect to the primary vertex $< 0.2 \text{ cm}$;
- No loosely isolated electrons $> 10 \text{ GeV}$ in the event;
- No b-tagged jets with $p_T > 20 \text{ GeV}/c$ in the event.

Figure 4.7 shows the $Jet \rightarrow \tau_h$ fake rate measured in the $W + Jets$ control region as described above using the 13 TeV data and $W + Jets$ MC events for a pseudorapidity $\eta < 2.1$.

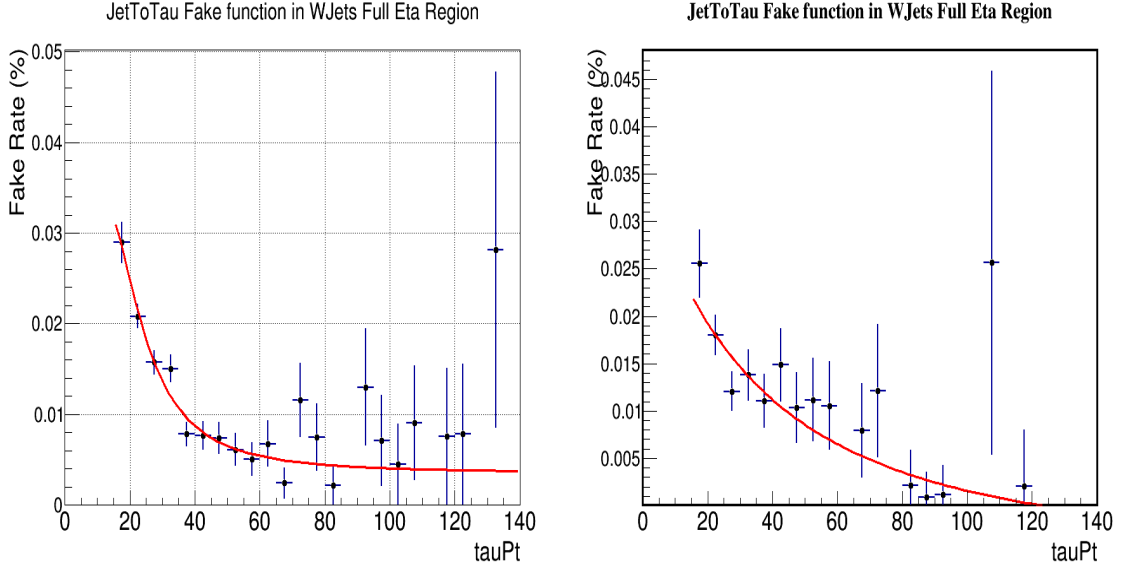


Figure 4.7: $Jet \rightarrow \tau_h$ fake rate in $W + Jets$ control region using 13 TeV data (left) and MC (right) events, fitted with a Landau function.

The $Z + Jets$ measurement region is selected in a similar way :

- Two isolated oppositely charged tight PF muons with $p_T \geq 20 \text{ GeV}/c$ ($p_T \geq 10 \text{ GeV}/c$) for the Leading (sub-Leading) muon respectively, and $|\eta| \leq 2.1$ for both muons;
- The invariant mass of the di-muon system, $M_{\mu\mu}$ should fulfill $70 \text{ GeV}/c^2 \leq M_{\mu\mu} \leq 100 \text{ GeV}/c^2$;
- The longitudinal impact parameter of both the muons with respect to the primary vertex is $< 0.2 \text{ cm}$;

- At least one τ_h without the isolation requirement;
- No loosely isolated electrons with $p_T > 10 \text{ GeV}$ in the event;
- No b-tagged jets with $p_T \geq 20 \text{ GeV}/c$ in the event.

The Fake function is then defined as

$$f(p_T) = \frac{p_T \text{ of the isolated } \tau_h \text{ candidates}}{p_T \text{ of the all } \tau_h \text{ candidates}} \quad (4.2)$$

Figure 4.8 shows $Jet \rightarrow \tau_h$ fake rates for 13 TeV data collected by CMS and $Z + Jets$ MC events for pseudorapidity $\eta < 2.1$.

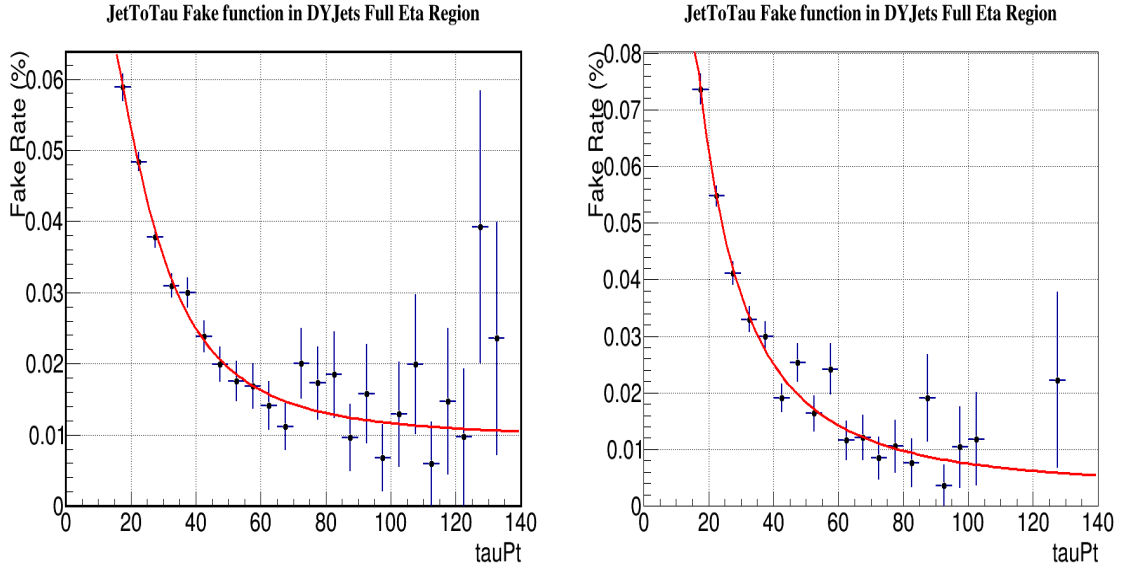


Figure 4.8: $Jet \rightarrow \tau_h$ fake rate in $Z + Jets$ control region using 13 TeV data (left) and MC (right) events, fitted with a Landau function.

To account for the detector effect, the parameterization in p_T is done in 3 η bins, central ($|\eta| \leq 0.8$), intermediate ($0.8 \leq |\eta| \leq 1.6$) and forward ($1.6 \leq |\eta| \leq 2.3$). The

disadvantage of measuring the fake rate in 3 η bins is reduced statistics which can be a factor while fitting the fake function.

4.2.4.2.2 Validation of the Fake Rate Method

It is essential to validate the fake estimation technique which is also known as a closure test. The diagram in Figure 4.9 explains the important control regions and side bands required for validation and estimation of fake contribution in the signal region. Along the

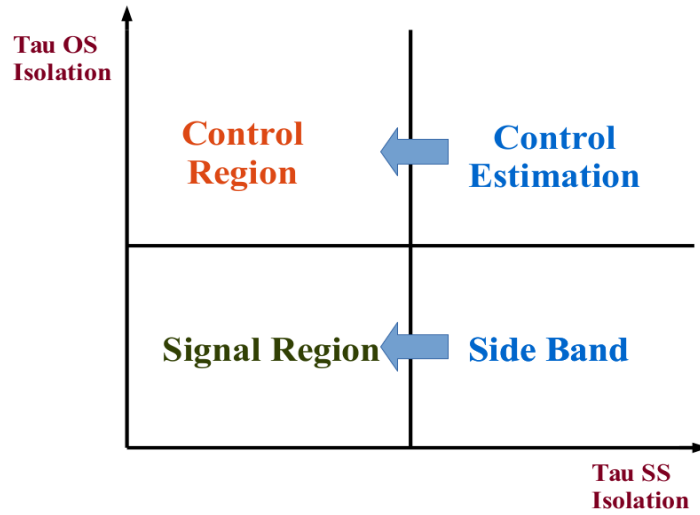


Figure 4.9: Definition of control regions in $WH \rightarrow \mu\tau_h\tau_h$ final state

X and Y axes of the diagram the isolation of the τ_h leg with same sign (SS) and opposite sign (OS) to the isolated muon are drawn, respectively. The tau isolation variable is built as a boolean quantity, so it can be either isolated or anti-isolated. The diagram shows the following four regions:

- The bottom left box is the **Signal Region** where both the τ_h legs are isolated. Presence of an isolated muon is required while defining the region.

- The bottom right box is the **Side Band** where the SS τ_h leg is anti-isolated. This region is used to estimate the fake contribution in the signal region by extrapolation.
- The top left box is the region of interest for validation of fake rate method, called **Control Region**. Here, the OS τ_h leg while the SS τ_h leg is isolated.
- The top right box is the region from where the extrapolation is made in order to predict the contribution in Control Region, called **Control Estimation Region**. Here, both the τ_h legs are anti-isolated.

In order to validate the fake rate method, the direct measurement in the **Control Region** for MC $Z + Jets$ or $W + Jets$ MC events have to agree with the prediction as extrapolated from the **Control Estimation Region** by applying a weight factor $w(p_T)$. The validation is better performed with data to avoid statistical uncertainty. Figure 4.10 shows the background composition in the **Control Estimation Region**, where the fake extrapolation will be applied to predict the fake contribution in the Control Region. As can be seen, the relative contribution of $Z + Jets$ events can be ignored with respect to the $W + Jets$ contribution. So, while doing the validation with data, only the fake function measured in $W + Jets$ control region using data has to be used.

Figure 4.11 displays distributions for muon p_T , $\tau_{OS} p_T$, $\tau_{SS} p_T$ and visible di-tau mass in the Control Region and the fake prediction from the Control Estimation Region. The agreement looks reasonable.

Figure 4.12 shows Control Region plots for τ_{OS} and $\tau_{SS} \eta$. The η distribution for the SS tau leg shows a disagreement between the observed data and fake prediction. This feature arises because the fake function that has been used to extrapolate the fake

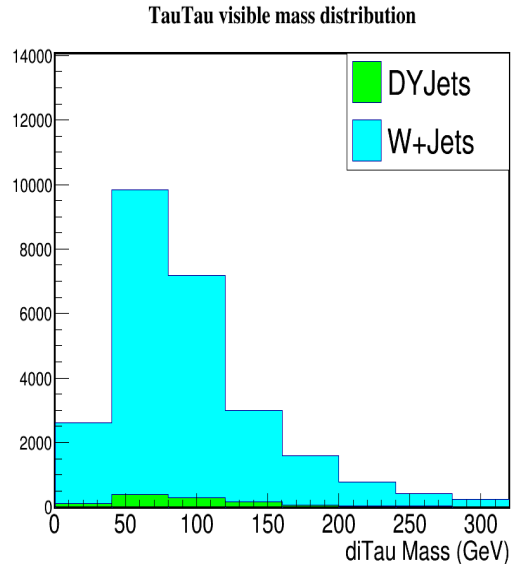


Figure 4.10: Background composition in the Control Estimation Region, normalized to the respective cross sections and an integrated luminosity of 2.1 fb^{-1} at $\sqrt{s} = 13 \text{ TeV}$.

prediction was parameterized as a function of p_T only, the η dependence was not taken into account. It is known that the fake function does not show a uniform response in the full η region.

Fake rates are measured in three separate η bins to incorporate the detector effect. Figure 4.13 shows the $Jet \rightarrow \tau_h$ fake rate measured with data in the $W + Jets$ control region for the following 3 η bins; central ($|\eta| < 1.1$), intermediate ($1.1 < |\eta| < 1.6$) and forward ($1.6 < |\eta| < 2.1$).

After considering the dependence of the fake function on both p_T and η of tau, Figure 4.14 shows a better agreement between the observed and expected shapes.

Similarly, Figure 4.15 shows set of Control Region distributions using the p_T and η dependent fake function.

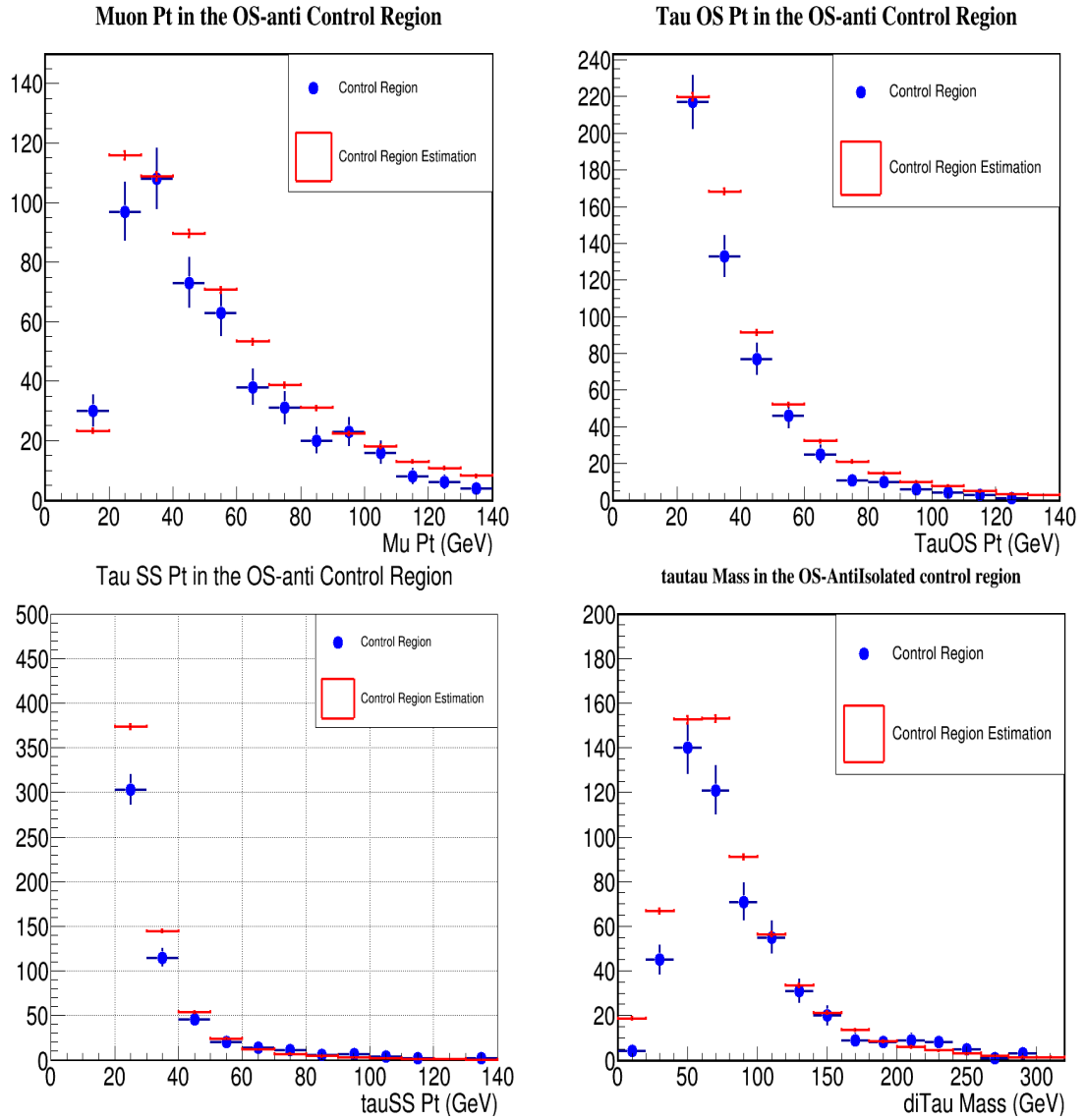


Figure 4.11: Control Region plots for muon p_T , $\tau_{OS} p_T$, $\tau_{SS} p_T$ and visible di-tau mass for 2.1 fb^{-1} of 13 TeV data collected by the CMS detector.

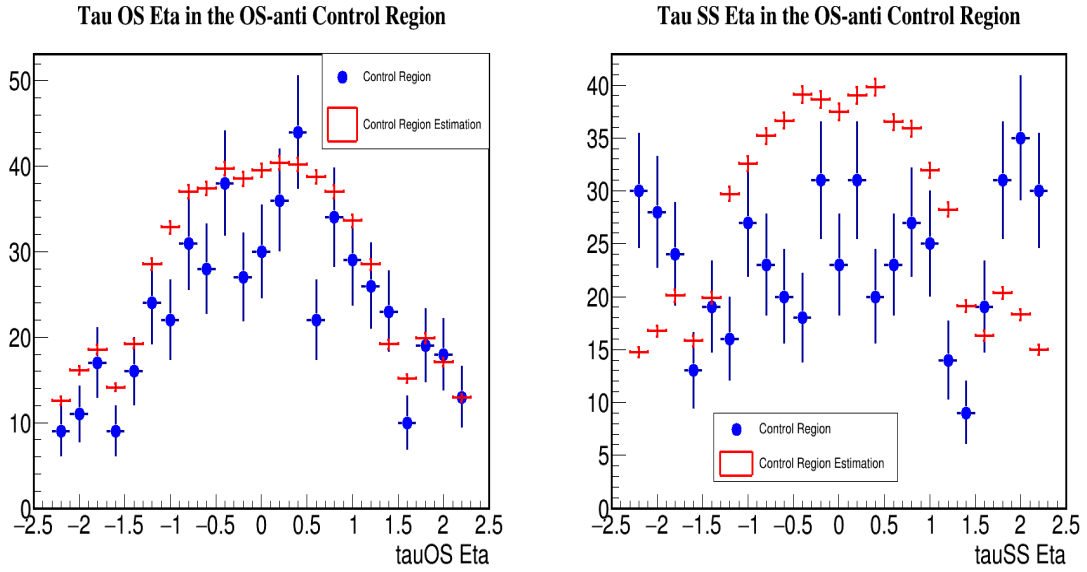


Figure 4.12: η distribution of the τ_{OS} (left) and τ_{SS} (right) in the Control Region using 2.1 fb^{-1} of 13 TeV data.

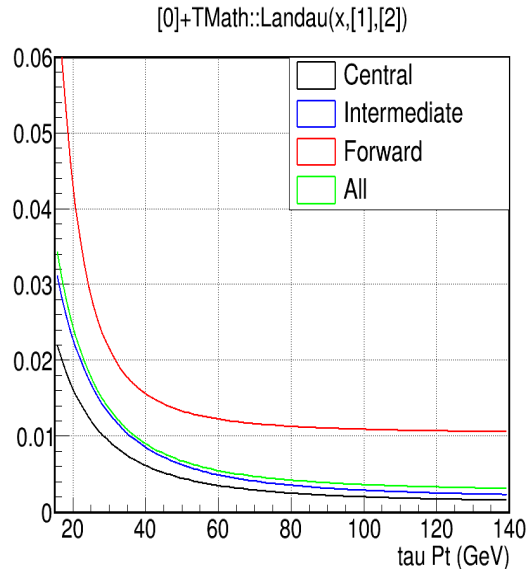


Figure 4.13: $Jet \rightarrow \tau_h$ fake rate measured in $W + Jets$ control region using the 13 TeV data as a function of tau pt in three bins of eta : central, intermediate and forward.

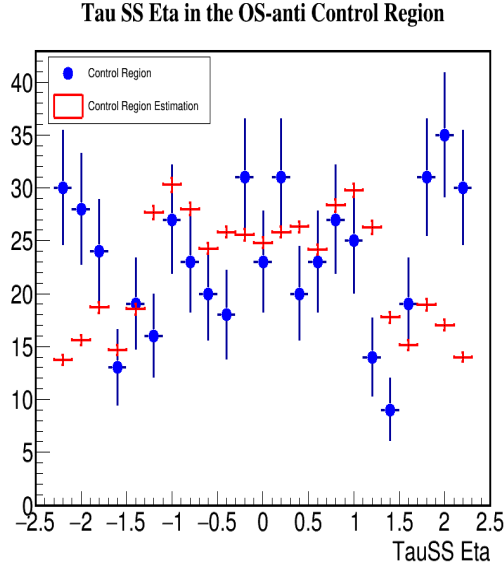


Figure 4.14: Distribution of τ_{SS} eta in the Control Region considering the p_T and eta dependent fake function. Now the observed and expected shapes agree better.

A second closure test was also performed by comparing the isolated and anti-isolated tau distribution in the fake dominated region after extrapolation using the fake function. Here the closure test is performed in the same region where fake rate has been measured i.e. in $W + Jets$ and $Z + Jets$ regions. The numerator of the fake function in Eq. 4.2 corresponds to the isolated tau in the fake dominated region, whereas the denominator is the sum of isolated and anti-isolated tau candidates. The idea here is to apply a weight factor $w(p_T)$ on the anti-isolated tau legs and check the compatibility with the isolated distributions.

Figure 4.16 and Figure 4.17 shows the closure distributions in $W + Jets$ and $Z + Jets$ control regions respectively.

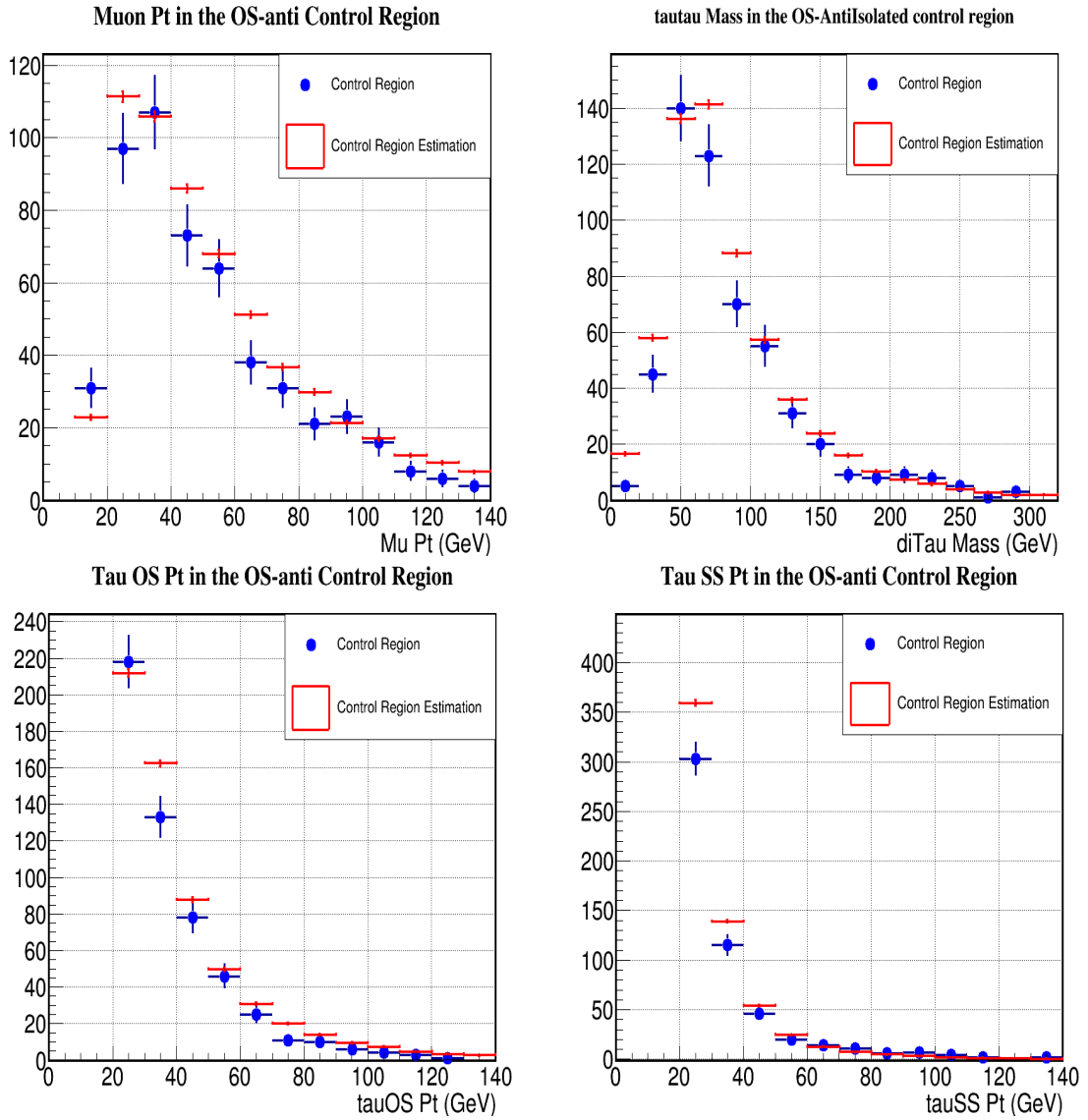


Figure 4.15: Distribution of muon pt, τ_{OS} p_T , τ_{SS} p_T and visible di-tau mass using pt and eta dependent fake function

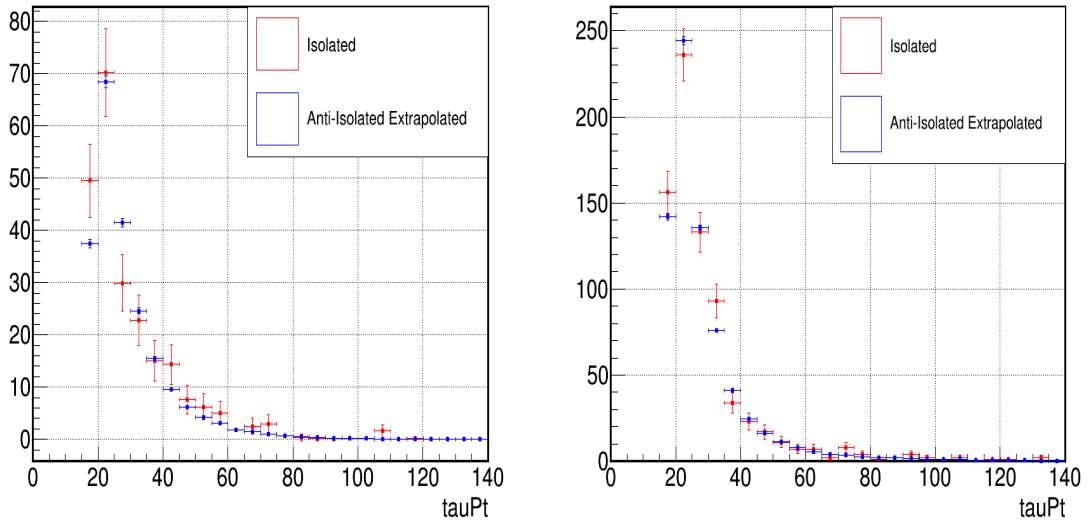


Figure 4.16: Closure test in $W + \text{Jets}$ control region using the 13 TeV MC (left) and data (right) samples.

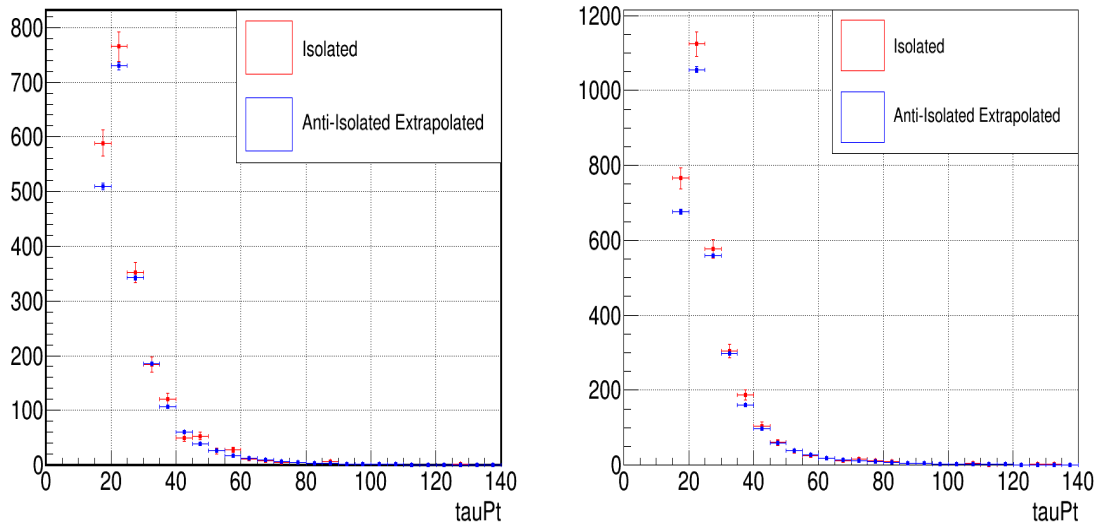


Figure 4.17: Closure test in $Z + \text{Jets}$ control region using the 13 TeV MC (left) and data (right) samples.

4.2.4.2.3 Estimation of Fake Contribution in Signal Region

The number of fake background events in the Signal Region is estimated from the number of events observed in the Side-Band region, in which the SS τ_h leg is required to be anti-isolated, Figure 4.9. Each event in the Side-Band region is then weighted with a factor $w(p_T) = \frac{f(p_T)}{1-f(p_T)}$, where f is the weighted average of the Fake Rate function measured earlier. The weights are chosen such that the final Fake Rate function reads as: $f = (w_1 * f_W + w_2 * f_Z)$, where f_W and f_Z are the Fake Rate functions obtained in the $W + Jets$ and $Z + Jets$ measurement region, respectively. Weight factors w_1 and w_2 are calculated from the relative composition of $W + Jets$ and $Z + Jets$ events in the Side-Band as seen from Monte Carlo simulation. This is the only information taken from Monte Carlo in the data-driven fake rate technique.

Figure 4.18 presents the visible mass distribution of the two opposite sign tau in the final state for $\sqrt{s} = 7$ & 8 TeV on the left and right hand side of the plot, respectively. The predicted background agrees with observed data.

Similarly, Figure 4.19 shows the final visible mass distribution for 2.1 fb^{-1} of data analyzed at $\sqrt{s} = 13$ TeV. Unlike the $\sqrt{s} = 7$ & 8 TeV scenarios, 13 TeV analysis has been optimized with higher p_T threshold on the τ_h legs. A nice agreement between observed data and estimated background have been found and no significant excess is observed.

4.2.5 Systematics

The following sources of systematic uncertainties have been considered:

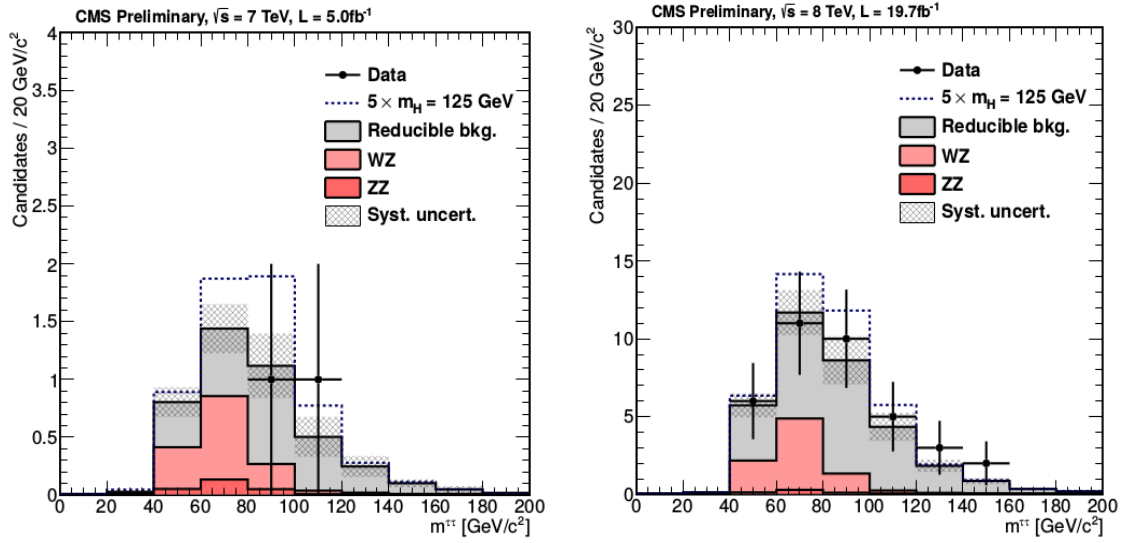


Figure 4.18: Visible mass distribution of the di-tau system for $\sqrt{s} = 7$ (left) and 8 TeV (right). The integrated luminosity for $\sqrt{s} = 7$ & 8 TeV runs are 5 and 19.5 fb^{-1} , respectively.

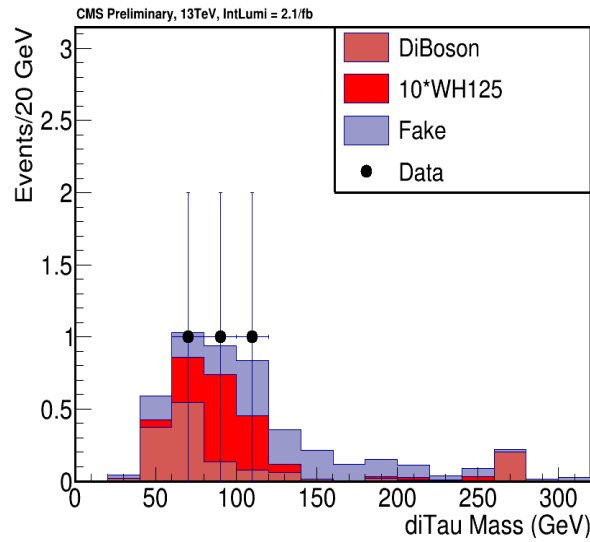


Figure 4.19: Visible mass distribution of the di-tau system coming from the $H \rightarrow \tau\tau$ decay for $\sqrt{s} = 13$ TeV using 2.1 fb^{-1} of integrated luminosity.

- **Luminosity:** A 2.2% uncertainty for 2011 data sample [18] and 4.4% for 2012 on the measured luminosity [19].
- **Parton Distribution Functions (PDF):** The systematic effect due to imprecise knowledge of the parton distribution functions is determined by comparing CTEQ6.6L, MSTW2008nnlo, and NNPDF20 PDF with the default PDF and variations within the family of parameterizations [20]. The maximal deviation from the central value is used to obtain the overall systematic effect due to PDFs, which came out to be 4.3%. This is consistent with values obtained in other WH analyses.
- **Trigger Efficiency:** The sample of events used in this search are collected with the inclusive muon trigger. The trigger efficiency for the muon leg is measured with respect to the offline selection using the Tag and Probe method on $Z/\gamma \rightarrow \mu\mu$ events. It is defined as the efficiency for a well identified offline muon to be matched to a HLT muon. There is a good agreement between data and simulation and $\varepsilon_{DATA}^{HLT}/\varepsilon_{MC}^{HLT}$ is compatible with unity within an uncertainty of $\delta_{elTrigger} < 1\%$ [12].
- **Muon ID Efficiency:** Muon efficiency is factorized into two components $\varepsilon_{tot} = \varepsilon_{Iso} \times \varepsilon_{ID}$. The muon identification efficiency (ε_{ID}) is defined as the efficiency to pass all the selection conditions except the isolation as outlined in the preceding sections. The muon isolation efficiency (ε_{Iso}) is defined as the efficiency to pass only the isolation condition. The simulation-to-data corrections for ε_{ID} have been measured in [12] and have uncertainties $\sim 0.3\%$ and 0.4% for the barrel and end-cap respectively. The simulation-to-data corrections for ε_{Iso} have been measured in [12] and have uncertainties of $\sim 0.4\%$. Therefore, a total systematic uncertainty on muon efficiency of $\delta_\varepsilon = \sqrt{(0.4\%)^2 + (0.4\%)^2} = 1.0\%$ is assigned. The correction factors are measured in $Z/\gamma \rightarrow \mu\mu$ events, where the topology can be different from WH events due to effects like initial and/or final state radiation. This difference in topology results in small differences in isolation efficiencies between Z and

WH events. An additional systematic uncertainty of 0.4% is assigned due to the difference in isolation between Z and WH events.

- **Tau ID Efficiency:** The tau identification systematic uncertainty measured in [13] is 6%. In a conservative approach, considering that the two selected taus are correlated, the total systematic uncertainty due to tau identification is 12%.
- **b-Tagging Efficiency:** A 20% uncertainty on the mis-tag rate as measured by the b-tagging Physics Object Group is considered. [15]
- **Electron Energy Scale:** The effect on the signal acceptance of a 1% shift on the electron energy scale is considered and the systematic effect was found to be negligible.
- **Muon Momentum Scale:** The effect on the signal acceptance of a 1% momentum scale uncertainty on the muon momentum is considered. The systematic effect is negligible.
- **Tau Energy Scale:** The effect of the measured 2% tau energy scale uncertainty on the signal acceptance is considered. The tau 4-momentum is measured by a factor of $k = 1.02$ ($p_{smearred} = k \cdot p_{default}$) and variables are recalculated using $p_{smearred}$. By using $p_{smearred}$ calculated with a factor of $k = \pm 1.02$, the signal acceptance fluctuates by $\sim 3\%$. Therefore, a 3% systematic on the signal acceptance due to the tau energy scale is assigned [13].
- **Jet Energy Scale:** The effect of a 2-5% jet energy scale uncertainty on the signal acceptance is considered. The jet 4-momentum is smeared by a factor of $k = 1.05$ ($p_{smearred} = k p_{default}$) and variables are recalculated using $p_{smearred}$. It is found that by using $p_{smearred}$ calculated with a factor of $k = \pm 1.02 - 1.05$, the signal acceptance fluctuates by $\sim 1\%$. Therefore, the systematic uncertainty on the signal acceptance of 1% is assigned due to jet energy scale.

- E_T^{Miss} : The uncertainty on E_T^{Miss} for the signal process is driven by the tau energy scale (TES), jet energy scale for non-tau jets (JES), muon energy/momentum scale, and unclustered energy (UCE). The unclustered energy scale (10%) is defined as the energy not associated with the reconstructed leptons and jets with $p_T > 10$ GeV/c . It is found that a 10% uncertainty on the unclustered energy results in 3.7% uncertainty on the signal acceptance.
- **Fake Rate Normalization:** The systematic uncertainty on the fake rate normalization is calculated by splitting the total uncertainty into many contribution.

First one is the statistical uncertainty of the fit of the measured fake rate as a function of p_T . To account for the uncertainty of the fit and its systematic effect on the analysis an uncertainty of 10% has been assigned by propagating the error on the fit parameter to the predicted number of background events.

Another systematic uncertainty that is taken into account is the difference between the calculations of the fake rate function using the $W + Jets$ and $Z + Jets$ events. The two functions are different, but this is understood to be due to event topology: the Fake Rate in $Z + 1Jet$ and $W + 2Jets$ events is different because of a different fraction of quark-induced and gluon-induced jets. A 10% uncertainty is attributed to the difference between the two regions when requiring two jets in both of them.

Next contribution to the systematic error comes from the determination of the weights when combining the Fake Rate function measured in a $W + Jets$ or a $Z + Jets$ enriched region. A 10% is attributed for this source of uncertainty.

A conservative estimate of a total uncertainty of 20% has been assigned, so that also those effects that are not known and are therefore not considered are covered. This seems reasonable because of many implicit assumptions associated with the Fake Rate background estimation technique.

- **Fake Rate Shape:** The statistical uncertainty on the fake rate based background can lead to differences in the shape of the background distribution. To estimate the systematic influence on the exclusion limits different shapes are used where each bin from fake visible mass distribution is scaled up and down by the statistical error individually. The exclusion limit is calculated for each shape which results in an additional systematic uncertainty which is taken into account during the limit calculation.

4.2.6 Results and Limits

No evidence for the standard model Higgs boson produced in association with a W^\pm has been found in the visible di-tau mass distribution. The exclusion limits for the $W^\pm H$ production process are calculated using the signal shape of the SM Higgs extracted from MC and the shapes corresponding to various background production processes. The background shape for processes like $W + Jets$, WW or QCD are estimated from data using the fake rate method, while for diboson production processes such as WZ and ZZ the shape is estimated using the MC simulation. The 95% confidence level (CL) upper limit and its $\pm 1\sigma$ and $\pm 2\sigma$ uncertainty regions on the rate of the signal with respect to the SM cross section are calculated with the Asymptotic CLs algorithm [21] using the visible mass of the selected di-tau pair. The algorithm uses a frequentist statistical test where a hypothesis with only background processes is tested against the model with background plus signal. In this algorithm the shape of the di-tau pair visible mass and its uncertainty is considered together with the systematic uncertainties on normalization, introduced as nuisance parameters.

The exclusion limits at $\sqrt{s} = 7$ & 8 TeV are shown in Figure 4.20, where the expected

and observed limits are drawn along with the 1σ and 2σ confidence intervals.

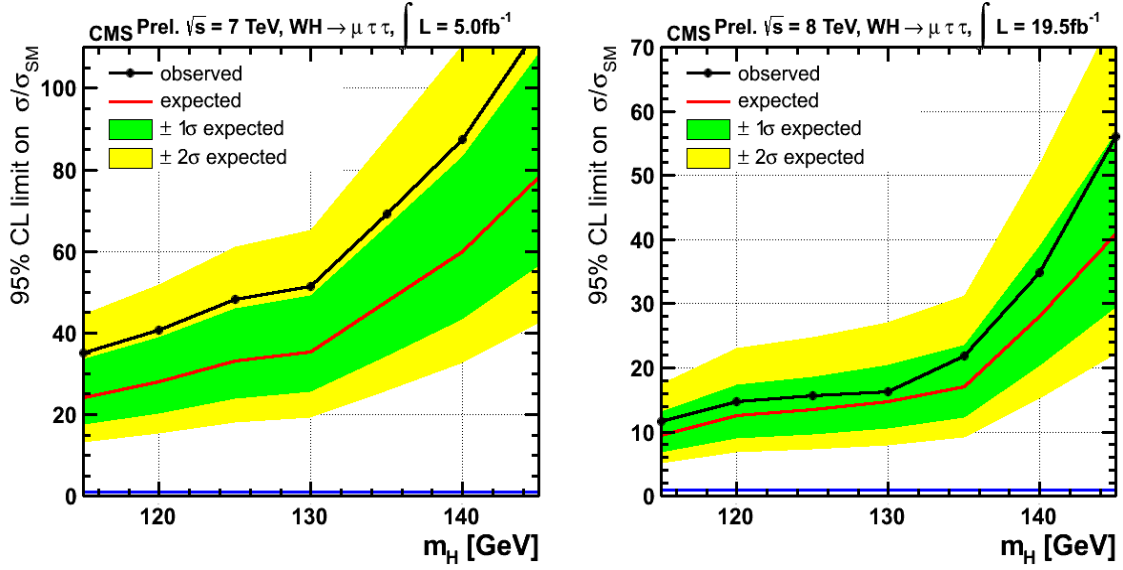


Figure 4.20: The 95% CL upper limits for the $W^\pm H$ production process with the $W^\pm(\mu^\pm)H(\tau_h^+\tau_h^-)$ channel for the 7 TeV (left) and 8 TeV (right) data collected by CMS.

Figure 4.21 presents the combined limit for 7 & 8 TeV analysis, where the expected limit for a $125 \text{ GeV}/c^2$ Higgs boson is $\sim 12 \times \text{SM}$ for the total 24.4 fb^{-1} of data collected by CMS during Run-1. More data is needed to improve sensitivity of this channel. The observed limit is compatible with both the SM background only as well as Higgs hypotheses. These results are a part of the inclusive $H \rightarrow \tau\tau$ search as published in [22] and [23].

The first 2.1 fb^{-1} of 13 TeV data has been analyzed and the corresponding expected limit is comparable to the $\sqrt{s} = 7$ TeV analysis at $125 \text{ GeV}/c^2$ as shown in Table 4.4.

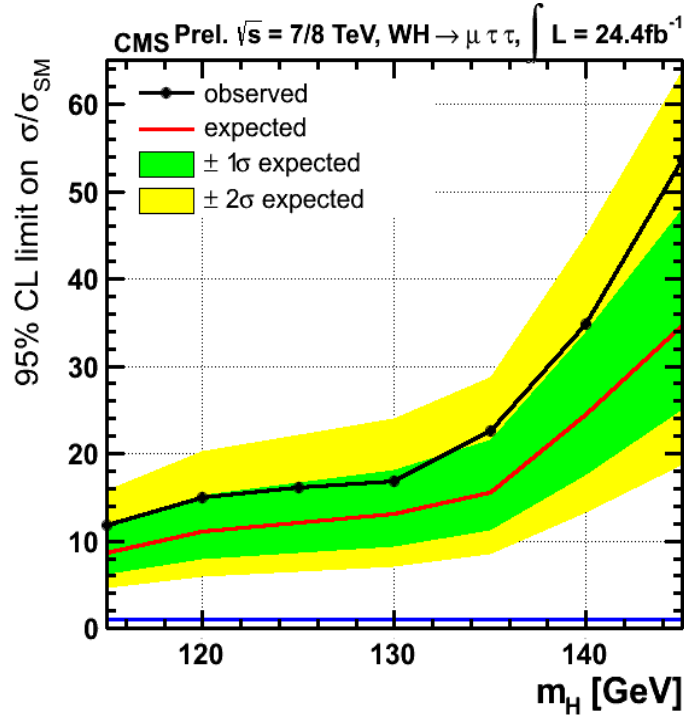


Figure 4.21: The 95% CL upper limits for the $W^\pm H$ production in SM with the $W^\pm(\mu^\pm)H(\tau_h^+\tau_h^-)$ channel combined for the 7 and 8 TeV data.

4.3 $WH \rightarrow \mu\mu\tau_h$ Analysis

A search for WH events in the $\mu\mu\tau_h$ final state has been performed with 2.1fb^{-1} of 13 TeV data collected in 2015, where the W decays to a highly energetic muon and H decays to a pair of τ leptons, one of which subsequently decays to a muon while the other decays hadronically to complement the $WH \rightarrow \mu\tau_h\tau_h$ analysis. The presence of an extra muon in the $WH \rightarrow \mu\mu\tau_h$ final state improves the event yield. The analysis is described in the following sections.

\sqrt{s} in TeV	Integrated Luminosity (fb^{-1})	Expected Limit at 125 GeV
7	5.0	$32 \times$ SM
8	19.5	$13 \times$ SM
13	2.1	$34 \times$ SM

Table 4.4: Comparison of expected limit at 125 GeV/c^2 for $WH \rightarrow \mu\tau_h\tau_h$ channel using $\sqrt{s} = 7, 8$ & 13 TeV datasets collected by CMS. Given the respective integrated luminosities, 7 & 13 TeV results are expected to be similar.

4.3.1 Baseline Selection

Object reconstruction, identification, and isolation techniques used in this analysis are identical to those used in the previous analysis. The mass of the candidate Higgs boson is reconstructed from the sub-Leading muon and hadronic tau. The Leading muon is supposed to originate from the W decay. Candidate events are selected online by the double-muon trigger. In the offline analysis the following selection conditions are applied:

- Leading Muon $p_T > 20$ GeV/c and $|\eta| < 2.1$;
- Sub-Leading Muon $p_T > 10$ GeV/c and $|\eta| < 2.1$;
- The muons are also required to pass the standard identification criteria, which demand the muon to be reconstructed as a Global or Tracker muon, have at least one hit in the pixel detector to discriminate against decays in flight, and pass the set of strict identification criteria;
- The $\Delta\beta$ -corrected relative PF isolation of the Leading muon has to be less than 0.15 (0.1) for candidates with $|\eta| < 1.479$ ($|\eta| \geq 1.479$);
- The $\Delta\beta$ -corrected relative PF isolation of the sub-Leading muon has to be less than 0.2 (0.15) for candidates with $|\eta| < 1.479$ ($|\eta| \geq 1.479$);
- τ_h $p_T > 20$ GeV/c and $|\eta| < 2.3$;

- τ_h should pass the standard identification criteria of Decay Mode Finding, rejection against electrons and muons, and pile-up corrected isolation.

The two muons are required to have the same charge, which greatly reduces the contribution from Drell-Yan and $t\bar{t}$ background events where an additional jet is reconstructed as a τ_h . The τ_h is required to have opposite charge with respect to the muons. The three objects are required to be well separated in the $\eta - \phi$ space. The probability for a quark or gluon jet to pass the hadronic tau identification and isolation (aka “Jet $\rightarrow \tau_h$ fake”) is 10 to 100 times larger than the probability for the same jet to pass the muon identification and isolation requirements. For the $WH \rightarrow \mu\mu\tau_h$ channel, requiring the muons to have the same charge removes the large $Z/\gamma \rightarrow \mu^+\mu^- + \text{fake jet } \tau$ background. To reduce contamination from ZZ and $t\bar{t}$ backgrounds, events with additional isolated electrons, isolated muons, or b-jets with a p_T above a threshold are rejected. None of these vetoes but the one for b-jet have a significant impact on the final result of the analysis. It also helps to avoid any overlap of the signal region with $t\bar{t}H$ analyses.

4.3.2 Background Estimation

Like the analysis of the fully hadronic channel, this analysis too has two different types of background, Irreducible and Reducible.

4.3.2.1 Irreducible Background

The di-boson WZ and ZZ processes contribute to the Irreducible background where the final state consists of at least three real candidates, exactly mimicking the $WH \rightarrow \mu\mu\tau_h$

topology. The selection efficiency and shape of the di-boson background are estimated using simulated events generated with Pythia. The normalization of the di-boson background is taken from the NLO theoretical prediction.

4.3.2.2 Reducible Background

The sources of this kind of processes include $W + Jets$, $Z + Jets$, QCD, $t\bar{t}Jets$ etc. The contribution is estimated by a data-driven fake rate technique. For $WH \rightarrow \mu\mu\tau_h$ analysis, a lepton fake rate method ($Jet \rightarrow \mu$ fake) has been introduced and the two muons (marked as Leading and sub-Leading) are used as the fakeable objects. In the following paragraphs the method and justification is described.

Depending on the decay mode of the background processes, reducible backgrounds are mainly of three types, which can have atleast one jet (Type I), two jets (Type II) and three jets (Type III) as fake objects. In Table 4.5, the different background processes, their fake type and how they have been estimated using fake anti-isolated leg are described. The fake estimate type indicates which final state objects are anti-isolated and weighted in order to predict the fake contribution in the signal region.

Type I backgrounds have two opposite sign (OS) real objects and one fake object. It is assumed that there are no Standard Model backgrounds, other than diboson events, with two isolated same-sign leptons (e, μ, τ_h). Two examples of type I background sources in the $\mu\mu\tau_h$ channel are $Z \rightarrow \tau\tau \rightarrow \mu\tau_h + jet \rightarrow \mu$ and $Z \rightarrow \tau\tau \rightarrow \mu\tau_h + jet \rightarrow \mu$. It is important to note that due to the charge requirement $\mu^\pm\mu^\pm\tau_h^\mp$, all type I backgrounds have either a fake Leading muon or a fake sub-Leading muon, but never a fake hadronic tau. To estimate all type I backgrounds, it is necessary to use both the Leading and

Background	Final State Objects			Estimated By			
	μ	μ	τ_h	μ	μ	$\mu\mu$	$\mu\mu\tau_h$
Two OS Isolated Leptons, Type-I							
$Z \rightarrow \tau\tau(\mu\tau_h) + Jet_\mu$	real	jet fake	real	no	yes	no	no
$t\bar{t} \rightarrow \mu\tau_h + Jet_\mu + Jet$	real	jet fake	real	no	yes	no	no
One Isolated Lepton, Type-II							
$W \rightarrow \mu + 2Jets$	real	jet fake	jet fake	no	yes	no	no
$W \rightarrow \tau_h + 2Jets$	jet fake	jet fake	real	yes	yes	yes	no
$t\bar{t} \rightarrow \mu + Jet_\mu + Jet_{\tau_h} + Jet$	real	jet fake	fake jet	no	yes	no	no
$t\bar{t} \rightarrow \tau_h + 2Jet_\mu + Jet$	jet fake	jet fake	real	yes	yes	yes	no
No Isolated Leptons, Type-III							
QCD	jet fake	jet fake	jet fake	yes	yes	yes	yes

Table 4.5: Definition of “Fake Type” and “Estimated By” in $WH \rightarrow \mu\mu\tau_h$ final state

sub-Leading muons, in turn, as the fakeable object, and sum together the two estimates.

Type II backgrounds consist of a single real object and two fake objects. In the $\mu\mu\tau_h$ channel type II backgrounds include $W \rightarrow \mu/\tau_h + 2$ jet fake and semi-leptonic $t\bar{t}$ decays. If the Leading or sub-Leading μ comes from the decay of the W boson, then the other remaining muon is fake, and the contribution to the signal region is accounted for by the corresponding fake estimate. In the case, when the τ_h comes from the decay of the W boson, both the Leading and sub-Leading μ are fake. The yield from this background is counted by both the μ fake estimates. Thus the $W \rightarrow \tau_h + 2jet \rightarrow \mu$ is double counted when the individual μ estimates are summed together. This double counting occurs for any background where both the muons are fake. It is corrected by using both the μ simultaneously as fakeable objects. It is referred to as the $\mu\mu$ fake estimate and is further illustrated in the next section when the estimation of background contribution is presented.

Type III backgrounds are dominated by QCD multi-jet events, where all the three final state objects are fake. As both the muons are fake in these events, they are also

double counted by the sum of the individual Leading and sub-Leading muon fake estimates. However, they are also included in the $\mu\mu$ fake estimate which is used to correct the double counting. The QCD contribution is thus correctly predicted by this method.

4.3.2.2.1 Lepton Fake Rate Measurement Control Regions

The probability $f(p_T)$ for a jet satisfying some loose requirements to pass the final lepton selection is measured for different types of background processes in selected background enriched control regions. These control regions should be exclusive to the signal region and be as close as possible to the signal selections to avoid biases. Purity of the control region is also a matter of concern. Contamination from processes with real isolated leptons should be kept as low as possible.

Three different background enriched control regions are used to measure the fake rate by tagging the physics process: $W \rightarrow \mu\nu + \text{jet}$, $Z \rightarrow \mu\mu + \text{jet}$, and QCD heavy-flavor. Once the physics process has been tagged, a probe jet passing the relevant loose selection in the event is used to measure the fake rate.

Events in the $W \rightarrow \mu\nu + \text{jets}$ control region are defined in the following way:

- One isolated high quality tag muon with $p_T > 20 \text{ GeV}/c$ and $|\eta| < 2.1$,
- The tag muon and E_T^{Miss} system has transverse mass $M_T > 40 \text{ GeV}/c^2$,
- The longitudinal impact parameter of the tag muon track with respect to the primary vertex is less 0.2 cm,
- The tag muon and object candidate (μ, τ_h) in the probe jet have the same sign (to

remove Z/γ),

- No additional loosely isolated muons above $5 \text{ GeV}/c$
- No additional loosely isolated electrons above $10 \text{ GeV}/c$,
- No b-tagged jets with $p_T > 20 \text{ GeV}/c$,
- No hadronic tau candidates passing HPS loose isolation with $p_T > 20 \text{ GeV}/c$, to avoid the signal region
- At least one Jet with $p_T > 20 \text{ GeV}/c$ to mimic the presence of a tau candidate

Figure 4.22 and Figure 4.23 exhibit the $Jet \rightarrow \mu$ fake rates using the 13 TeV data collected by the CMS detector in Run-2 for the $W + Jets$ and $Z + Jets$ control regions respectively. Fake rates are measured separately for the Leading and sub-Leading muons because of different isolation requirements.

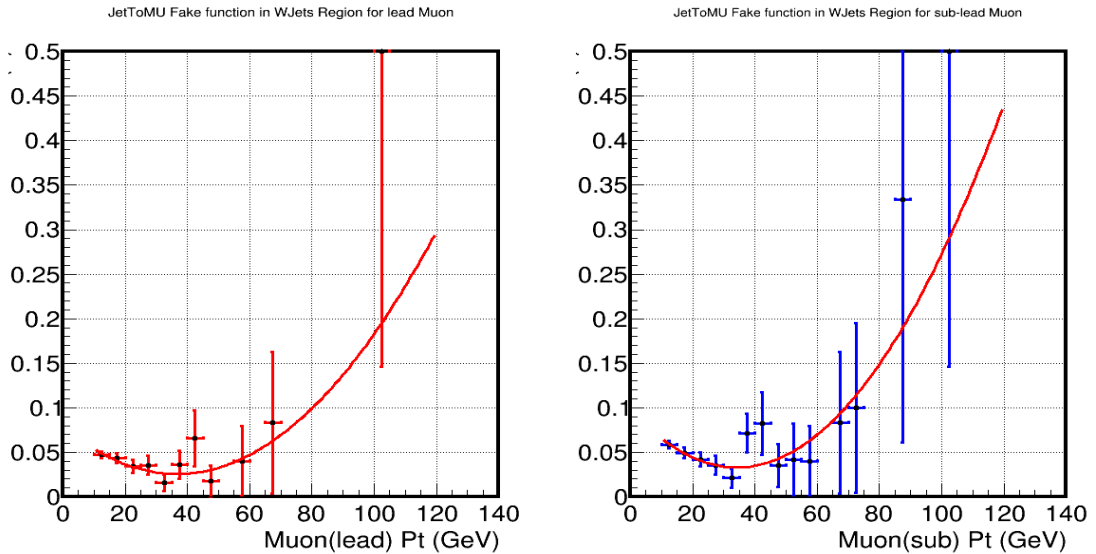


Figure 4.22: $Jet \rightarrow \mu$ fake rate for the Leading (left) and sub-Leading (right) muons using the 13 TeV data in the $W + Jets$ control region.

Similar way, the $Z \rightarrow \mu\mu + \text{Jets}$ control region is defined by the following selections

- Two isolated tightly identified tag muons with $p_T > 20, 10 \text{ GeV}/c$ and $|\eta| < 2.1$,
- Invariant mass of the two tag muon should satisfy, $70 < M_{\mu\mu} < 110 \text{ GeV}/c^2$.
- $E_T^{Miss} < 20 \text{ GeV}$, since no missing energy is expected in $Z \rightarrow \mu\mu$ events.
- The transverse mass (M_T) of the probe jet and E_T^{Miss} system is less than $20 \text{ GeV}/c^2$ to remove WZ contamination,
- The longitudinal impact parameter of the tag muon track with respect to the primary vertex is less 0.2 cm,
- No additional loosely isolated muons above $5 \text{ GeV}/c$
- No additional loosely isolated electrons above $10 \text{ GeV}/c$,
- No b-tagged jets with $p_T > 20 \text{ GeV}/c$.

4.3.2.2.2 Estimation of Fake Background

Fake contribution in the signal region of $WH \rightarrow \mu\mu\tau_h$ final state is measured from a control region where the τ_h is always isolated and among the Leading and sub-Leading muons atleast one or both are anti-isolated, as illustrated in Figure 4.24. The bottom right box marked as '1' is the signal region where all the three leptons are isolated (highlighted in blue). Then comes the region 2, 3 and 4 where the Leading μ , sub-Leading μ or both the muons are anti-isolated, respectively. Anti-isolated objects are marked as red for understanding. Fake contribution in the signal region is extrapolated in the following way,

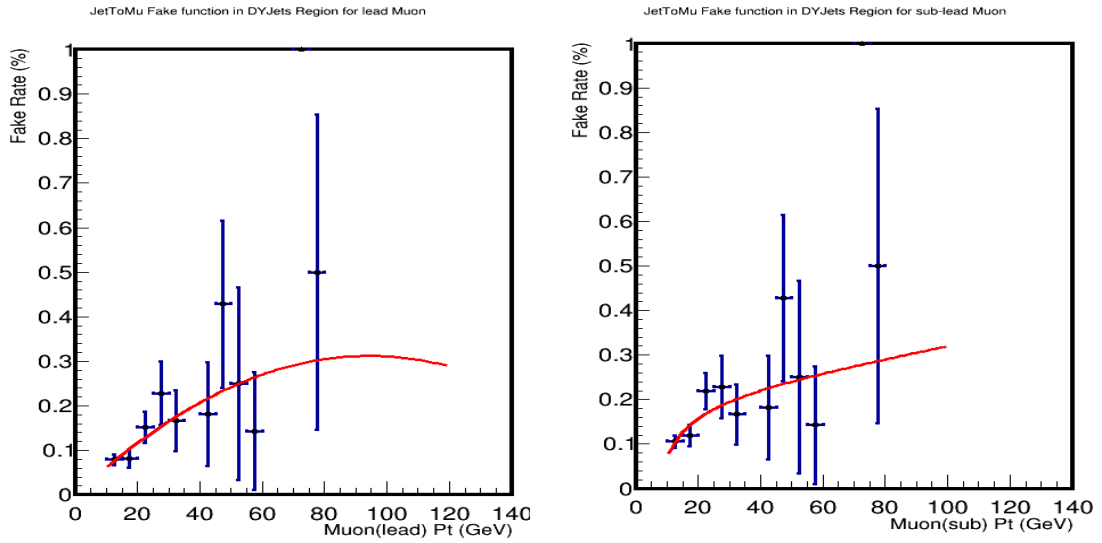


Figure 4.23: $Jet \rightarrow \mu$ fake rate for the Leading (left) and sub-Leading (right) muons using the 13 TeV data in the $Z + Jets$ control region.

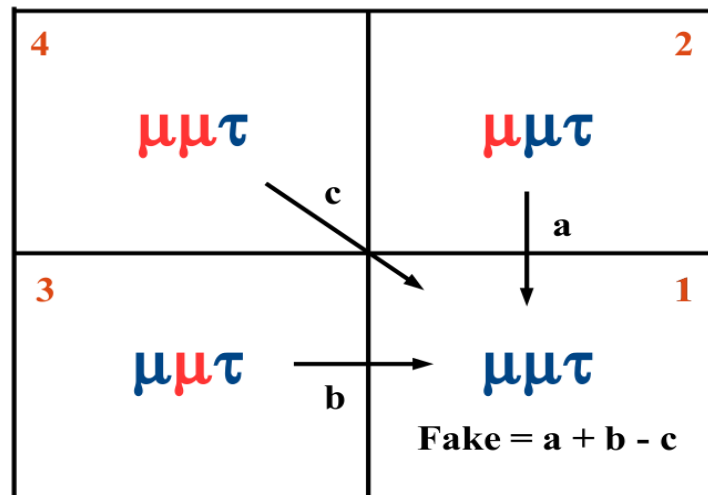


Figure 4.24: Definition of regions for Fake Contribution estimation in $WH \rightarrow \mu\mu\tau_h$ final state

- **Contribution from 2 \rightarrow 1 a:** Extrapolation is made using the weight factor $w(p_T) = f(p_T)/(1 - f(p_T))$, where $f(p_T)$ is the $Jet \rightarrow \mu$ fake rate for the lead μ measured as a function of muon p_T .
- **Contribution from 3 \rightarrow 1 b:** Extrapolated in the same way, but with the $Jet \rightarrow \mu$ fake function for the sub-leading muon.
- **Contribution from 4 \rightarrow 1 c:** In this region both the muons are anti-isolated at the same time. To extrapolate the fake contribution from this region, both the muon legs have to be weighted.

$$c = \frac{f_{leading}(p_T)}{(1 - f_{leading}(p_T))} * \frac{f_{sub-leading}(p_T)}{(1 - f_{sub-leading}(p_T))} \quad (4.3)$$

It is understood that the contribution c from region 4 \rightarrow 1 has already been counted twice by a and b . So the final fake contribution in the signal region should be, ($a + b - c$).

For this analysis, a **Control Region** for validation is defined by the same diagram in Figure 4.24 but with inverted τ_h isolation to increase the statistics and choose a region exclusive to the signal events. Figure 4.25 displays the distributions for reconstructed visible Higgs mass, Leading muon p_T , sub-Leading muon p_T and tau p_T in the **Control Region**. The agreement looks reasonable.

4.3.3 Systematics

Systematic uncertainties considered in the analysis are shown in Table 4.6,

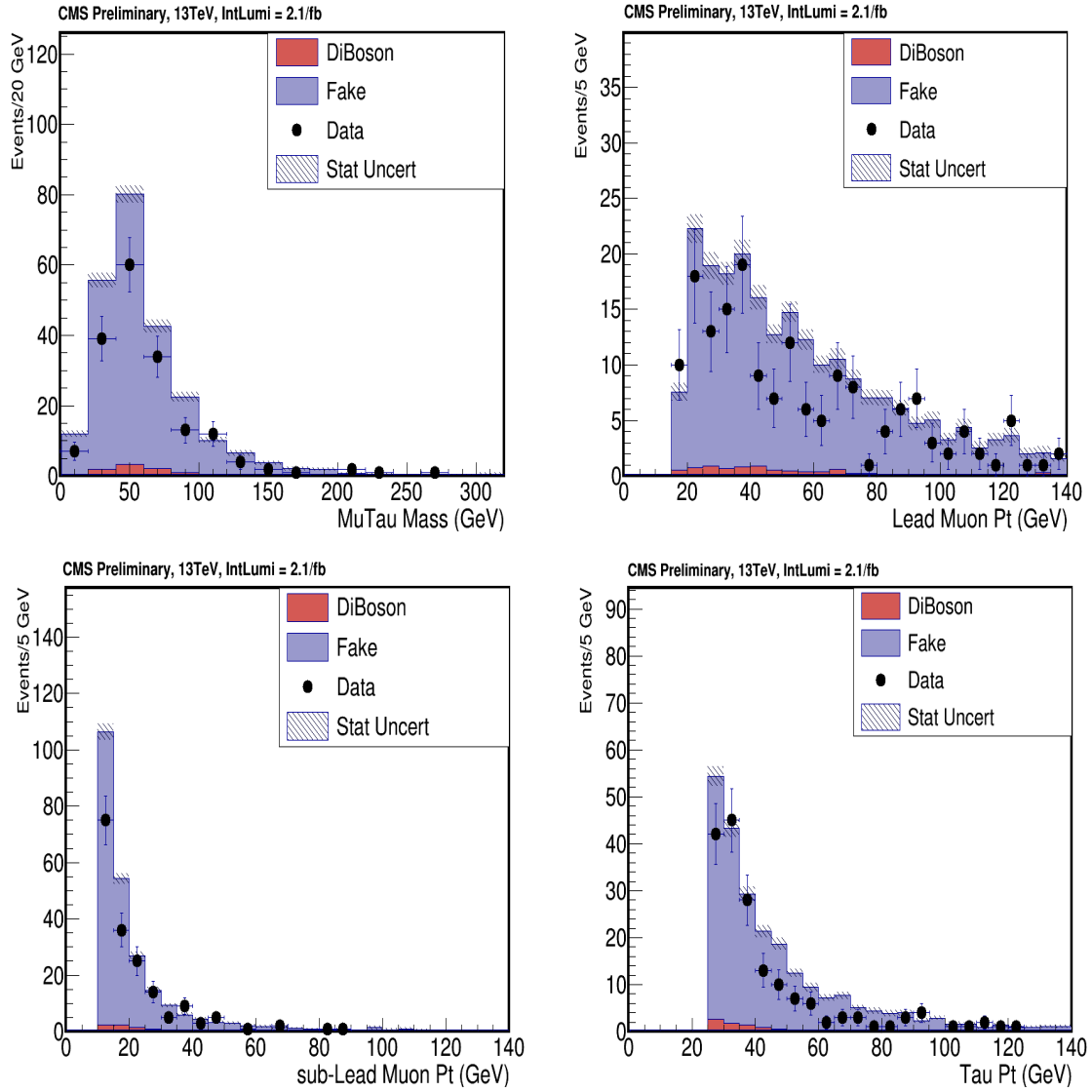


Figure 4.25: Control Region plots for reconstructed visible Higgs mass, Leading and sub-Leading muon p_T , and tau p_T for 2.1 fb^{-1} of 13 TeV data collected by the CMS detector.

Source	Uncertainty
Luminosity	4.5 %
σ_{WZ}	16.6 %
σ_{ZZ}	40 %
$\sigma_H(\text{PDF})$	4.5 %
Fakes	30 % + CR Stat
Tau Energy Scale	1-2.5 %
Tau ID	6 %
Muon ID + Iso	1 %

Table 4.6: Normalization systematic uncertainties for the $WH \rightarrow \mu\mu\tau_h$ final state.

4.3.4 Results and Limits

Figure 4.26 shows the visible mass distribution of the Higgs candidate formed by the sub-Leading muon and the tau in the final state. It compares the expected and observed

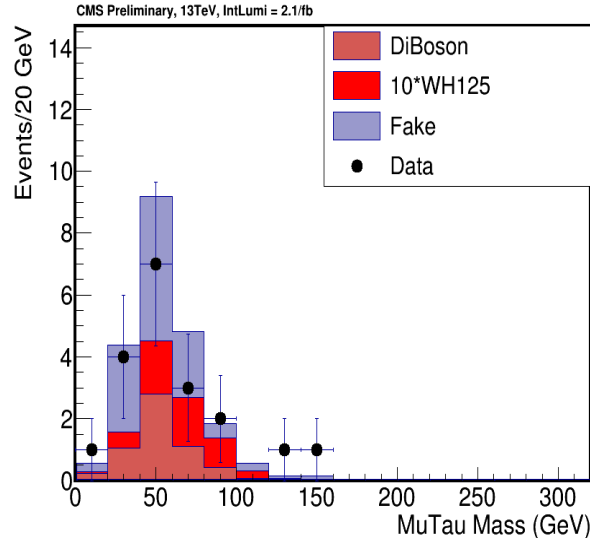


Figure 4.26: Visible Mass distribution of the sub-Leading muon and tau in the final state for the $WH \rightarrow \mu\mu\tau_h$ channel using the 2.1 fb^{-1} of 13 TeV data collected by CMS in Run-2.

events for the $WH \rightarrow \mu\mu\tau_h$ final state using the 13 TeV data and shows no indication of excess with respect to the predicted background. A 95 % CLs upper limit is set on

the Higgs boson production cross section, in terms of the standard model expectation. Table 4.7 is comparing the expected limit at $125 \text{ GeV}/c^2$ for 13 TeV data with the previous 7 & 8 TeV analyses. More data is needed to increase the sensitivity of the channel.

\sqrt{s} in TeV	Integrated Luminosity (fb^{-1})	Expected Limit at 125 GeV
7	4.9	$16 \times \text{SM}$
8	19.7	$8 \times \text{SM}$
13	2.1	$21 \times \text{SM}$

Table 4.7: Comparison of expected limit at $125 \text{ GeV}/c^2$ for $WH \rightarrow \mu\mu\tau_h$ channel using $\sqrt{s} = 7, 8$ & 13 TeV datasets collected by CMS.

Bibliography

- [1] Particle Data Group, “Review of particle physics”, Chin. Phys. C 38 (2014) 090001.
- [2] T. Sjostrand, S. Mrenna, and P. Z. Skands, “Pythia 6.4 physics and manual”, JHEP 0605 (2006).
- [3] S. Alioli et. al., “A general framework for implementing NLO calculations in shower Monte Carlo programs: the POWHEG BOX”, JHEP 1006 (2010) 043.
- [4] J. Alwall et. al., “MadGraph 5 : Going Beyond”, JHEP 1106 (2011) 128.
- [5] GEANT4 Collaboration, “GEANT4 - a simulation toolkit”, Nucl. Instrum. Meth. A 506 (2003) 250.
- [6] S. Jadach et. al., “The tau decay library TAUOLA: Version 2.4”, Comput. Phys. Commun. 76 (1993) 361-380.
- [7] CMS Collaboration, “Commissioning of the Particle-Flow Reconstruction in minimum-bias and jet events from pp collisions at 7 TeV”, CMS Physics Analysis Summary CMS-PAS-PFT-10-00

- [8] CMS Collaboration, “Particle-flow event reconstruction in CMS and performance for jets, taus, and E_T^{miss} ”, CMS Physics Analysis Summary CMS-PAS-PFT-09-001, 2009.
- [9] CMS Collaboration, “Commissioning of the particle-flow event reconstruction with the first LHC collisions recorded in the CMS detector”, CMS Physics Analysis Summary CMS-PAS-PFT-10-001, 2010.
- [10] E. Chabanat and N. Estre, “Deterministic annealing for vertex finding at CMS”, in Computing in high energy physics and nuclear physics. Proceedings, Conference, CHEP’04, Interlaken, Switzerland, September 27-October 1, 2004, p. 287. 2005.
- [11] W. Waltenberger, R. Fruhwirth, and P. Vanlaer, “Adaptive vertex fitting”, J. Phys. G: Nucl. Part. Phys. 34 (2007) N343.
- [12] CMS Collaboration, “Performance of CMS muon reconstruction in pp collision events at $\sqrt{s} = 7$ TeV”, JINST 7 (2012) P10002.
- [13] CMS Collaboration, “Performance of tau-lepton reconstruction and identification in CMS”, JINST 7 (2012) P01001.
- [14] CMS Collaboration, “Reconstruction and identification of tau lepton decays to hadrons and tau neutrino at CMS”, JINST 11 (2016) P01019.
- [15] CMS Collaboration, “Performance of b-jet identification in CMS”, CMS Note (2011), CMS PAS BTV-11-001.
- [16] H. Voss, A. Hocker, J. Stelzer and F. Tegenfeldt, “TMVA, the Toolkit for Multivariate Data Analysis with ROOT”, in XI Int. Workshop on Advanced Computing and Analysis Techniques in Physics Research 2007. arxiv:physics/0703039. PoS ACAT:040.

-
- [17] CMS Collaboration, “Measurement of the WW, WZ and ZZ cross sections at CMS”, CMS Note (2011), CMS-PAS-EWK-11-010.
- [18] CMS Collaboration, “Absolute Calibration of the Luminosity Measurement at CMS: Winter 2012 Update”, CMS Note (2012). CMS-PAS-SMP-12-008.
- [19] CMS Collaboration, “CMS Luminosity Based on Pixel Cluster Counting - Summer 2012 Update”, CMS Note (2012). CMS-PAS-LUM-12-001.
- [20] S. Dittmaier et. al., “Handbook of LHC Higgs cross sections”, arXiv:1101.0593v2 [hep-ph] (2011).
- [21] G. Cowan et. al., “Asymptotic formulae for likelihood-based tests of new physics”, Eur. Phys. J. C71 (2011) 1554.
- [22] CMS Collaboration, “Evidence for the 125 GeV Higgs boson decaying to a pair of τ leptons”, JHEP 1405 (2014) 104.
- [23] CMS Collaboration, “Evidence for the direct decay of the 125 GeV Higgs boson to fermions”, Nature Phys. 10 (2014).

Level 1 Track Trigger with Electron

5.1 Introduction

The Large Hadron Collider (LHC) is scheduled for several upgrades to ensure smooth running and achieve its physics goals. The tentative time line of the projected LHC luminosity is presented in Figure 5.1. The high luminosity period that follows Long Shutdown 3, (LS3, tentatively between 2022-2024) with the upgraded LHC is referred to here as **HL-LHC** or **Phase-II**. The proposed operating scenario is to level the instantaneous luminosity at $5 \times 10^{34} \text{cm}^{-2} \text{s}^{-1}$ from a potential peak value of $2 \times 10^{35} \text{cm}^{-2} \text{s}^{-1}$ at the beginning, and to deliver $\sim 250 \text{fb}^{-1}$ per year for a further 10 years of operation. Under these conditions the event pile-up will increase many fold to become a major challenge for the experiments, and degradation in detector performance due to integrated radiation

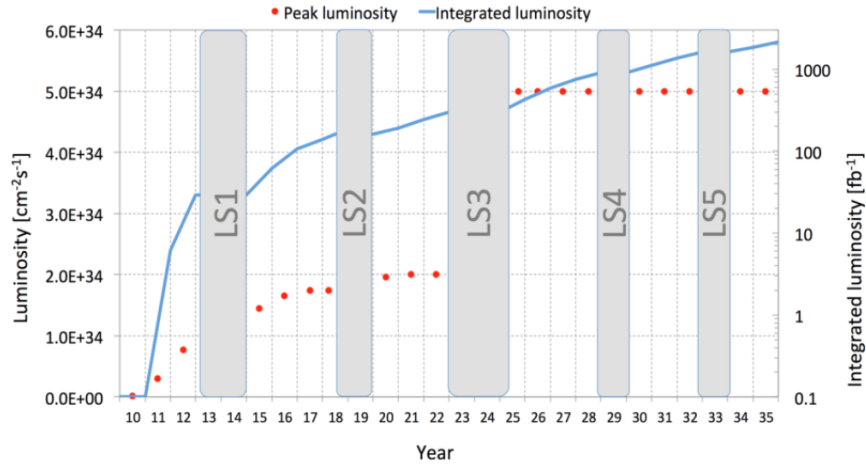


Figure 5.1: LHC timeline for the projected luminosity. LSx stands for “Long Shutdown x”. Left side of the Y-axis is showing the peak instantaneous luminosity and right side is showing the integrated luminosity.

dose will need to be addressed. The physics scope of the LHC would be significantly extended by this luminosity upgrade. This would increase the LHC mass reach by about 20 - 30 % and provide the possibility to measure the Higgs self-coupling, probing of its tensor structure, and search for rare SM and BSM decays. During the Phase-II Upgrade (LS3) of the CMS detector several modifications have to be made in order to maintain the expected physics performance. A number of sub-detector components need to be upgraded due to the radiation damage caused by prolonged running till the LS3 starts. In the HL-LHC scenario, it is expected to have 100-200 minimumbias interactions per beam crossing, which is 6-7 times higher than the present value. The present High Level Trigger (HLT) of the CMS detector and Data Acquisition System (DAQ) will not be able to sustain such high rate of events and it is required to reduce the rate at the Level 1 trigger by at least an order of magnitude. A simple increase in the trigger threshold cannot achieve this rate reduction at Level 1 Trigger because a similar physics performance of the CMS detector must be ensured at the low mass range as of the 7 & 8 TeV runs. The selectivity of Level 1 trigger needs to be improved to deal with the harsh pile-up

environment. The present Level 1 trigger of the CMS detector does not use any tracker information. It is based entirely on the calorimeter and muon detector. The reduction of event rate by required margin is not possible to achieve by the calorimeter based triggers, even after the upgrade, because of the coarse granularity or resolution. It is understood that the tracker information must be included in Level-1 trigger to meet the required resolution. A work has been done in developing an improved trigger algorithm for Level 1 electron including the tracker information to achieve an acceptable L1 rate even at the lower threshold without compromising the efficiency. This was an important result included in the technical proposal for the Phase II tracker upgrade [1] to demonstrate the usefulness of L1 tracking-trigger for electron. In the following sections the details of the algorithm and expected performance have been described.

5.2 Trigger Primitive

The current CMS tracker detector will no longer be efficient due to the integrated luminosity dose at the time of the Phase-II Upgrade. It needs to be replaced completely. At the same time a new tracker detector has been optimized, that has the capability to provide tracking information at Level I. A longitudinal view of the new outer tracker design is shown in Figure 5.2, which has 6 barrel layers and 5 endcap discs (hence the name Barrel-Encap 5 Discs or BE5D). Each layer is made up with sandwiched sensors separated by $O(1)$ mm, called “Stacked Module” or “ p_T -module” and the layers are called “Stacked Layer” as can be seen from Figure 5.3. The blue modules in Figure 5.2 are called “**Pixel-Strip**” (**PS**) module and the red ones as “**Strip-Strip**” (**SS or 2S**) module. As the name suggests the PS modules are a sandwich of pixel and strip type detector modules, providing better z-position resolution in the barrel layers or r-position resolution in the endcap. The SS modules have two close-by strip sensors with worse z-position

(or r-position) resolution than the PS one. The PS modules are placed closer to the interaction vertex to get a precise vertex position measurement.

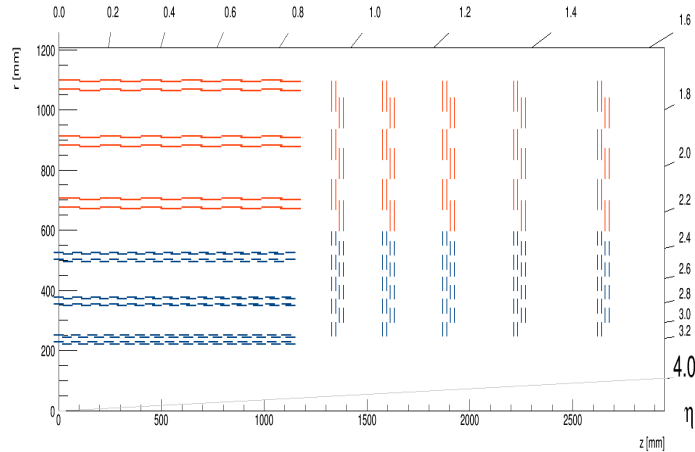


Figure 5.2: Schematic diagram of the BE5D outer tracker geometry

5.2.1 Stub

Charged particle hits in two sensors of the stacked module are accumulated as cluster signal in adjacent strips and correlated clusters in a stacked module is called a “**Stub**”. In Figure 5.3 a closely spaced stacked module is displayed in $r - \phi$ plane. The segments are strips in ϕ direction. The two parallel sensors in a stacked module are displaced along radial direction for barrel modules and in the z-direction for the endcap modules. The concept behind this “ p_T -module” design is that tracks below a certain p_T threshold can be rejected at the hardware level by looking into the amount of bending in the closely spaced sensor modules. As can be easily understood, the distance between the two closely spaced parallel sensors is an important parameter to tune the p_T threshold of tracks that are to be rejected. It was decided to set the p_T threshold of track rejection at 2 GeV/c, since more than 95 % of the tracks coming from pile-up fall below this p_T

threshold.

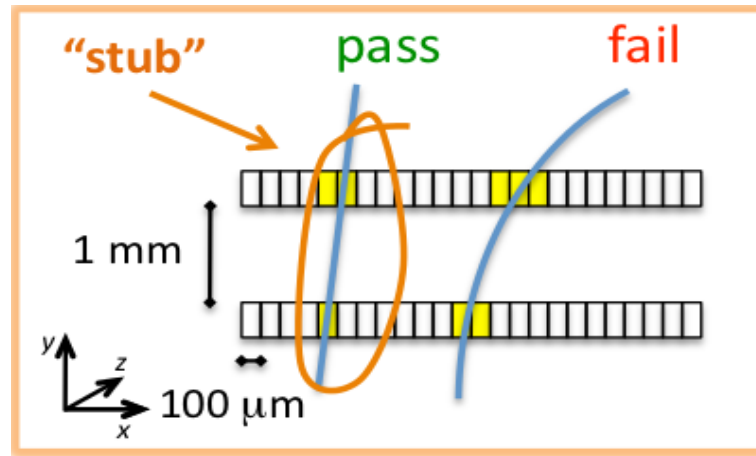


Figure 5.3: Schematic diagram of Stub formation in a stacked module

5.2.2 Tracklet

In Figure 5.4 a schematic diagram of the formation of a tracklet for a high P_t track is shown. Two correlated stubs in two adjacent layers is called a **Tracklet**.

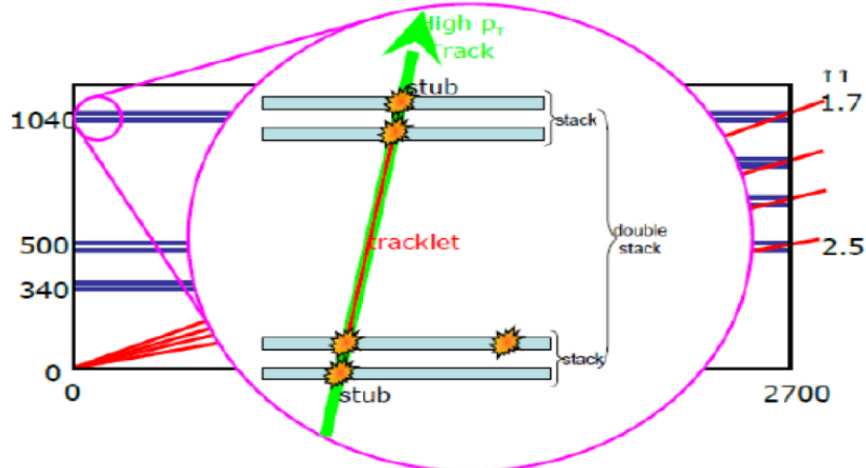


Figure 5.4: Schematic diagram of Tracklet formation in a double-stack module

5.3 Tracks at Level 1

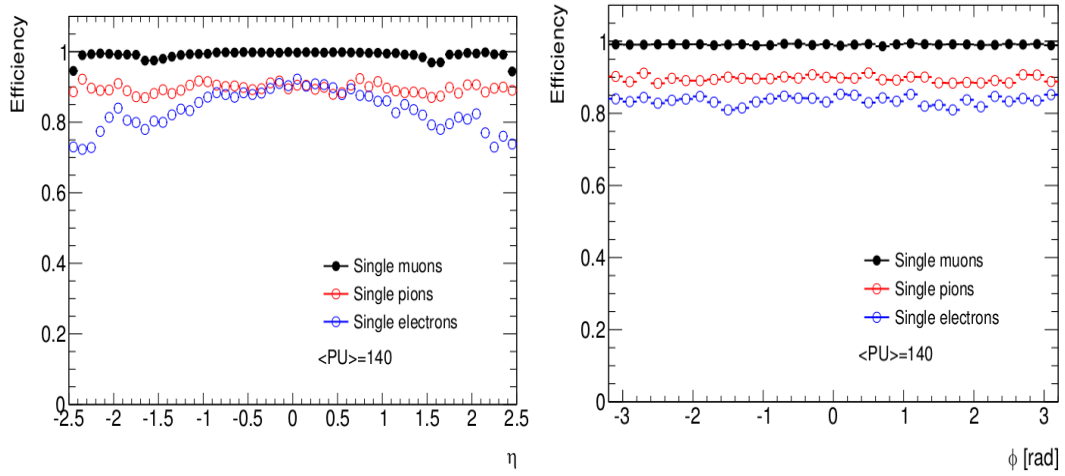
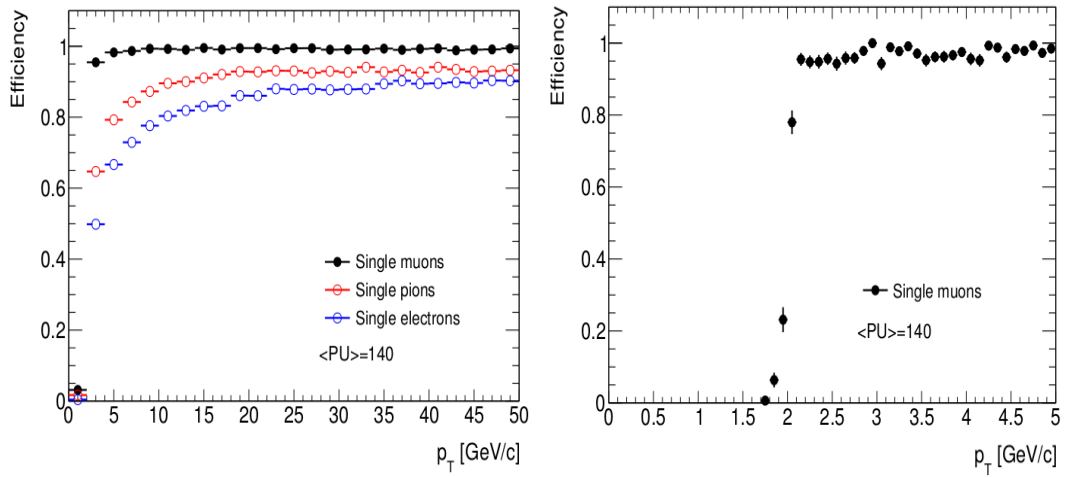
There are two main approaches being pursued parallelly to reconstruct tracks at Level-1 in the Phase-II upgrade scenario by the collaboration. One is the traditional and aggressive approach where tracking is done by extrapolating the tracklets as seed to the outer or inner layers. This is known as the Tracklet-based tracking. Another idea is to use the Associative Memory based tracking which works in a two step way, first it checks if the candidate track matches with any of the pre-stored low precision patterns inside the memory bank and then fitting the stubs with full precision. For the present study of the Level 1 Electron trigger, only the tracklet-based tracks have been used.

The tracklet based algorithm to reconstruct L1 tracks proceeds in four major steps. First tracklets are formed from pairs of stubs in neighboring layers which are consistent with a track with $p_T > 2$ GeV originating from $z < 15$ cm. The seeding is performed multiple times between different layers and disks to ensure high efficiency. Next the tracklets are projected to other layers and endcap disks to search for matching stubs. The projection is performed both inside-out and outside-in. The third step of the algorithm is the track fitting, performed as a linearized χ^2 fit of stubs matched to the trajectory. Finally duplicate tracks are removed based on their χ^2 , since a given track can be found many times due to seeding in multiple pairs of layers. The method uses precomputed derivatives to very quickly obtain an improved estimate of the track parameters.

It is very essential to ensure a quality tracking performance at Level 1, because the main objective is to benefit from the tracking information by combining L1 Tracks with calorimetric trigger primitives. L1 tracking efficiencies and track parameter resolutions are studied for single particle tracks. Samples with single muons, pions and electrons

are used, all overlaid with an average pileup of 140. The single particles are uniformly distributed in ϕ , η and p_T with Gaussian distributed d_0 and z_0 according to the expected LHC beam envelope. L1 tracks are required to have $|\eta| < 2.5$, $|z_0| < 30$ cm, and $p_T > 2$ GeV. For studies of muons and pions, L1 tracks are required to have $\chi^2 < 100$ and a minimum of 4 stubs associated to each track. In Figure 5.5, L1 tracking efficiency is shown for muon, pion and electron with $p_T > 2$ GeV as a function of η (left) and ϕ (right). The efficiency is observed to be independent of ϕ within the statistics, while an η dependence is particularly prominent. For muons, the efficiency is $>99\%$ in the central pseudorapidity region, $|\eta| < 1.0$, while in the barrel to endcap transition regions, i.e around $1.0 < |\eta| < 1.5$, the efficiency is reduced to about 97%. The efficiency integrated over η and $p_T > 2$ GeV is about 99% for single muons. Electrons and pions show around 80 % and 90 % efficiency respectively when integrated over the η or ϕ range. In the higher η region the efficiency for electrons fall off rapidly due to material effect.

For electrons, with a higher rate of interaction in the tracker through bremsstrahlung, a looser selection is used where the χ^2 and number of stub cuts are relaxed. Additionally, the L1 tracking is run with a looser setting applied for electrons, where the matching windows used to extrapolate “tracklets” to other layers and discs in searching for matching stubs are a factor of two larger than the default setting. In Figure 5.6, L1 tracking efficiency is shown as a function of p_T for the full p_T range for muon, pion and electron in the left side of the plot. In the right side of the plot Figure 5.6, low p_T turn on region, integrated over η is shown as a function of p_T for muons in events with $\langle PU \rangle = 140$. The L1 track parameter resolution of the fitted L1 tracks are studied for single-muon events. In Figure 5.7, η (left) and ϕ (right) resolutions are shown as a function of η for low, medium and high p_T range of muons. The η resolution ranges between $1.0 - 2.5 \times 10^{-3}$ for high p_T tracks and is about 3.0×10^{-3} for tracks at low p_T . The ϕ resolution is about 0.3 mrad in the barrel region for a 10 GeV track. In Figure 5.8, p_T (left) and z_0

Figure 5.5: L1 Tracking efficiency as a function of η (left) and ϕ (right)Figure 5.6: L1 Tracking efficiency as a function of p_T

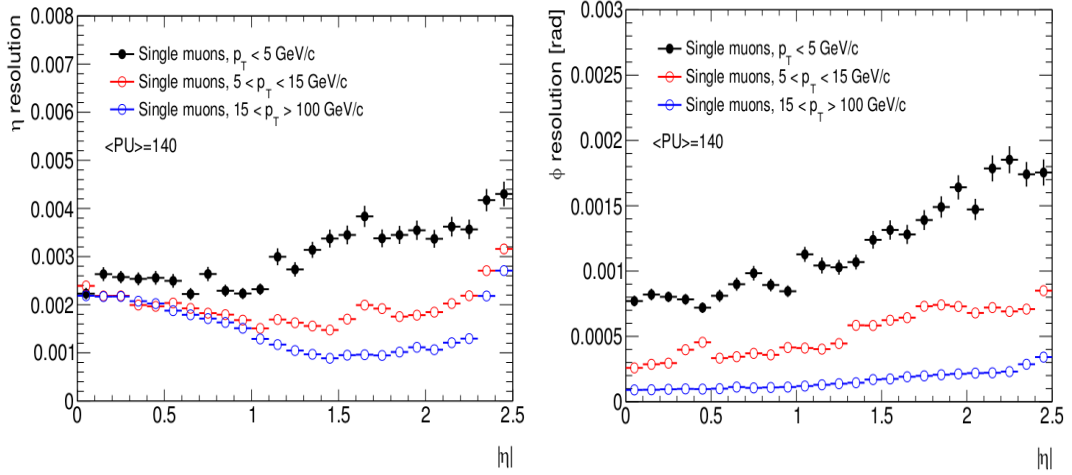


Figure 5.7: η resolution (left) and ϕ resolution (right) for muon as a function of η

(right) resolutions are shown as a function of η for low, medium and high p_T muons. The p_T resolution is about 1% at central η for high- p_T tracks but is significantly worsened in the outer regions. A distinctive feature of the L1 tracks is the precise z_0 resolution. Despite the large extrapolation distance (the first layer is at 25 cm), due to the 1.5 mm long pixels in the PS modules the z_0 resolution is about 1 mm for a wide range of pseudorapidity, similar to the average separation of pileup vertices. For $|\eta| > 2.2$, the z_0 resolution is less precise due to lack of PS module coverage in this region.

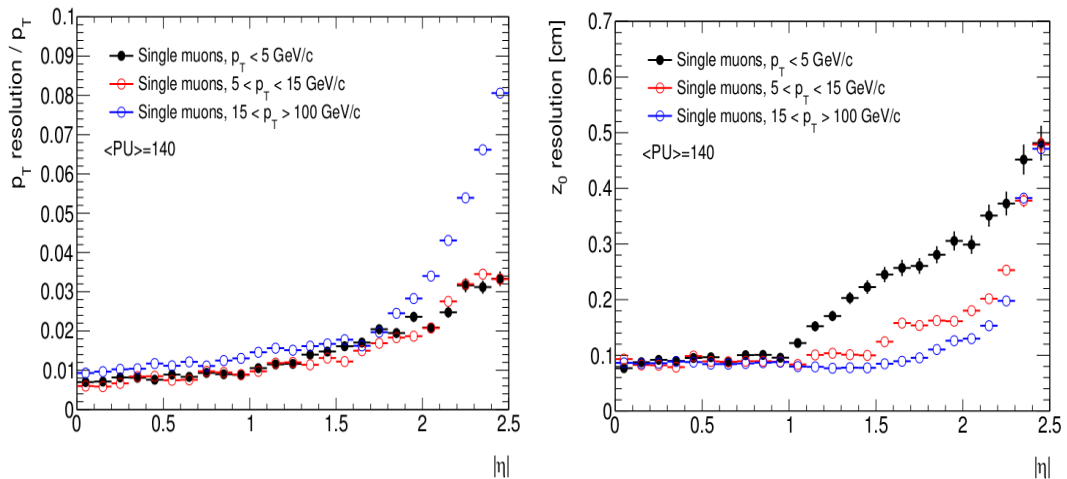


Figure 5.8: p_T resolution (left) and z_0 resolution (right) for muon as a function of η

5.4 Electron Triggers

The impact of tracking information on the L1 trigger electron identification and corresponding gain in the rate reduction is discussed here. Algorithms are developed to match L1EGamma objects provided by the calorimeter trigger with L1 tracks [1, 2] and stubs [2, 3]. The effect of track based isolation has also been studied in detail.

5.4.1 Calorimeter Electrons

Standard CMS simulation of the tower-level calorimeter trigger uses an optimized algorithm developed for High Luminosity LHC (HL-LHC). Both isolated and non-isolated L1EGamma objects have been used for the study.

Single electron events produced with particle gun and superimposed with 140 minimum bias events are used, where the electrons are generated with transverse momentum in the range 2-50 GeV and within $|\eta| < 3.0$. In Figure 5.9 distributions of generated electron E_T and η are shown for no pile up case.

It is important to tag the signal electron, which is used to quote the efficiency, correctly in the electron+140 PU events. A monte-carlo truth technique by simply choosing the minimum Δ_R matched electron candidate with respect to the generated electron, has been used, where Δ_R is the relative angle in the $\eta - \phi$ plane. A cutoff of 0.5 is applied on the minimum Δ_R angle to get rid of the accidental matches with pile-up events. It should be noted that a tighter cutoff leads to a set of signal electrons which produces a biased efficiency measurement. Because only η and ϕ variables are available in the

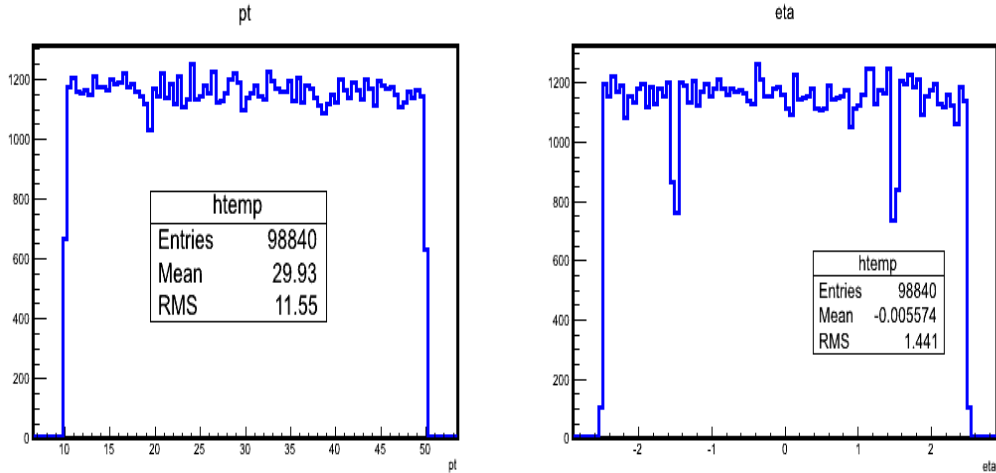


Figure 5.9: Distribution of electron E_T generated for 10-50 GeV range (on the left) and pseudo-rapidity Eta (of the right) are shown for no pile-up events.

existing L1EGamma objects, the r position of the object is calculated assuming that the calorimeter is a cylinder of radius 129 cm and length 628 cm, placing the showers at a depth of $0.89(7.7 + \log(E_{cal}))$, where E_{cal} is the total energy deposited in the calorimeter (in GeV).

5.4.2 L1EGamma object to Stub Matching

A two step algorithm has been used to match L1EGamma objects with stubs. In the first step individual stubs with the transverse momentum (p_T) > 5 GeV in the tracker with positions consistent with the L1EGamma objects are pre-selected and in the second step, pair of compatible stubs are selected with more stringent conditions. The three innermost barrel layers and the first three discs on either side of the interaction point i.e mostly PS modules are considered for making the stub pair. Details of the algorithms are described below.

To pre-select single stubs consistent with the calorimeter objects, we construct two roads for positive and negative charges from the beam spot to the L1EGamma object position through the tracker, using the curvature defined by the transverse energy measured in the calorimeter. Two spatial variables $\Delta\phi$ and $Z_{\text{intercept}}$ are used to restrict the width of the road in $r - \phi$ and $r - z$ planes respectively.

- $\Delta\phi$: difference in azimuthal angle between the stub (ϕ_{stub}) and the L1EGamma object measured in the calorimeter (ϕ_{ecal}) where, ϕ_{stub} has been corrected for the curvature of the trajectory.

$$\Delta\phi = \phi_{\text{stub}} - \phi_{\text{ecal}} \pm (r_{\text{ecal}} - r_{\text{stub}}) \frac{d\phi}{dr} \quad (5.1)$$

where

$$\frac{d\phi}{dr} = -3.0 \times 10^{-3} \frac{B}{E_{T,\text{ecal}}} \quad (5.2)$$

and B is the magnetic field in Tesla and $E_{T,\text{ecal}}$ is the transverse energy deposited in the calorimeter.

- $Z_{\text{intercept}}$: the intercept with the beam-line of a line drawn from the calorimeter object through the stub in the r-z plane

$$Z_{\text{intercept}} = \frac{r_{\text{ecal}}Z_{\text{stub}} - r_{\text{stub}}Z_{\text{ecal}}}{r_{\text{ecal}} - r_{\text{stub}}} \quad (5.3)$$

A schematic diagram of the $\Delta\phi$ variable is shown on the left of Figure 5.10. As seen from the figure, it is the difference between the expected phi position of the stub from the original position at a particular layer. Since the charge of the electron can not be determined from the calorimeter energy deposit, expected phi position of the stub will lie on either side of the original position. On the right side of the Figure 5.10, the concept

of $Z_{\text{intercept}}$ variable is shown.

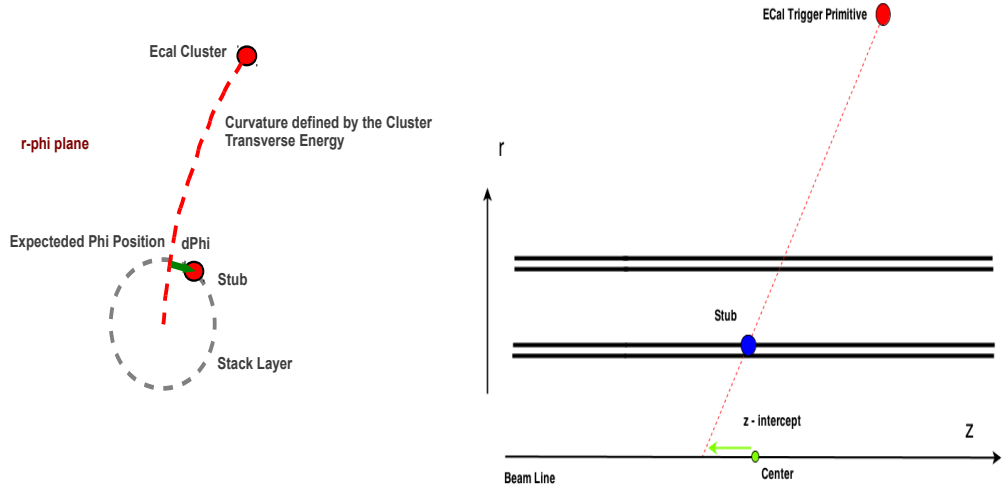


Figure 5.10: schematic diagram of $\Delta\phi$ (left) and z -intercept (right).

The $\Delta\phi$ distributions for the stubs in the innermost three barrel layers are shown in Figure 5.11. Stubs are pre-selected with the condition that $|\Delta\phi| < 0.05$ radian.

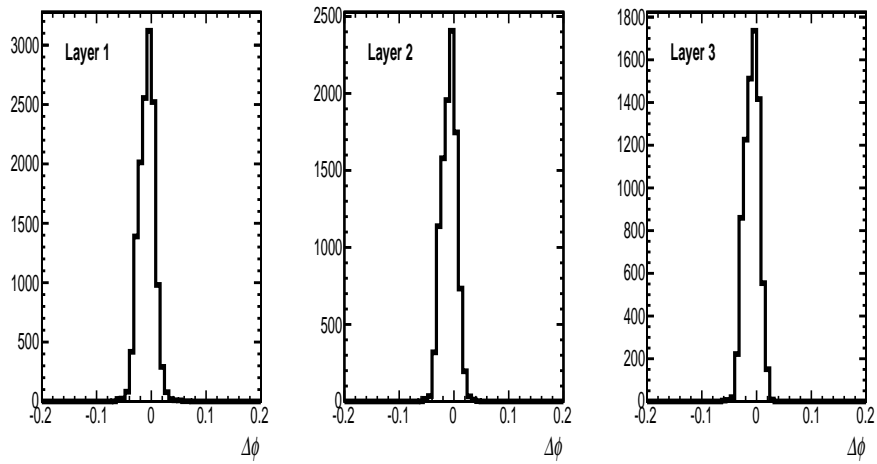


Figure 5.11: $\Delta\phi$ distribution for first three barrel layers.

In Figure 5.12, the $Z_{\text{intercept}}$ distribution of the first and third barrel layers are shown.

We select stubs with $|Z_{\text{intercept}}| < 20$ cm. No significant dependence of the $|Z_{\text{intercept}}|$ variable on η has been observed.

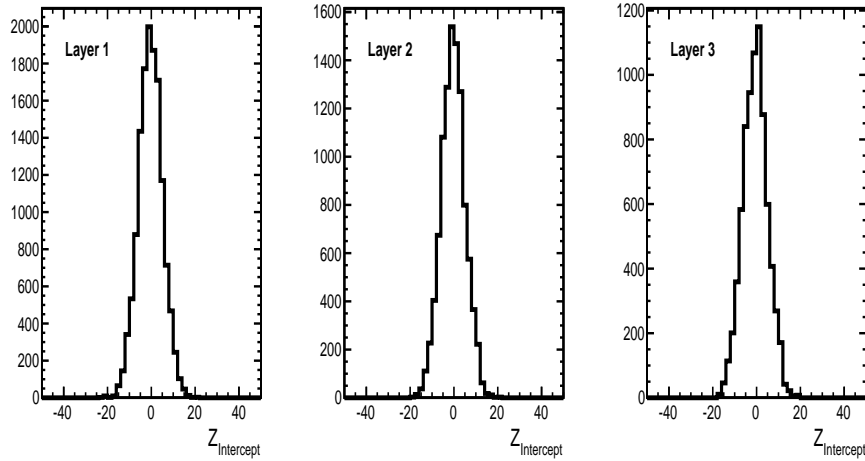


Figure 5.12: Distribution of $Z_{\text{intercept}}$ for 1st, 2nd and 3rd barrel layers.

From the list of pre-selected stubs, compatible stub pairs are identified to form stub-doublets. These doublets must satisfy loose ϕ and z cuts to be consistent with the same trajectory. The ϕ difference between the two stubs should be within the predicted ϕ due to the curvature in the magnetic field. Similarly the z coordinate of these stubs should be within a given tolerance of the interaction point. With these we can significantly reduce number of stubs on which finally the algorithm is applied.

Two variables ϕ_{miss} and Z_{miss} , based on the ϕ and z coordinates of the stubs in the doublet are constructed which are constrained further to match the stub doublet and the L1EGamma object. ϕ_{miss} compares the observed phi coordinate of the outer stub with its predicted value based on a charged particle trajectory, whose E_t is given by the L1EGamma object, and which passes from the beam-line through the ϕ coordinate of the inner stub. Z_{miss} compares the observed z coordinate of the outer stub with its predicted value based on a straight line trajectory which passes through the (r,z) -coordinates of

the inner stub and the L1EGamma object.

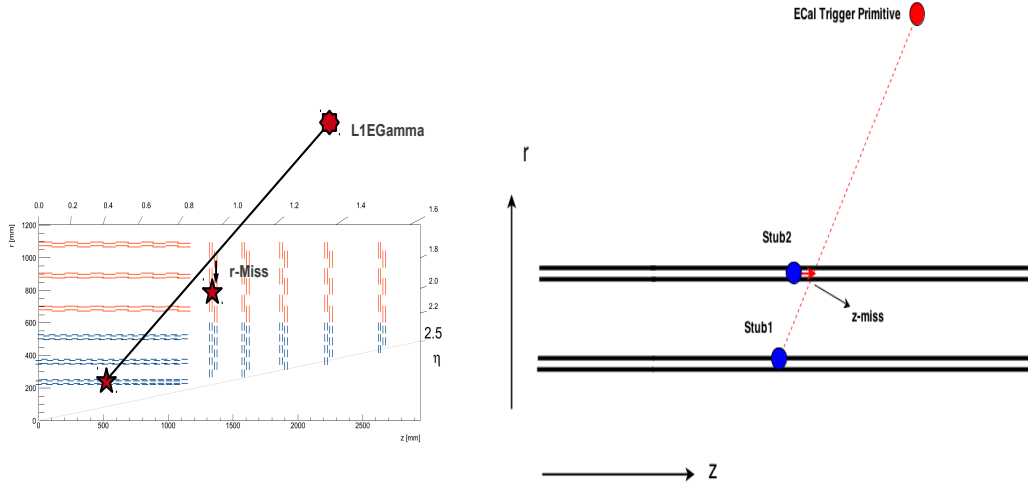


Figure 5.13: schematic diagram of r_{Miss} (left) and Z_{miss} (right).

$$\phi_{\text{miss}} = \phi_{\text{stub2}} - \phi_{\text{stub1}} \pm (r_{\text{stub1}} - r_{\text{stub2}}) \frac{d\phi}{dr} \quad (5.4)$$

where ϕ_{stub1} , ϕ_{stub2} , r_{stub1} and r_{stub2} are the ϕ and r positions of the inner and outer stubs in the doublet. In Figure 5.14, the ϕ_{miss} distributions are shown for the barrel layers. We select stub doublets if $|\phi_{\text{miss}}| < 0.007$ radian.

$$Z_{\text{miss}} = z_{\text{stub2}} - \frac{r_{\text{stub2}}(z_{\text{ecal}} - z_{\text{stub1}}) - r_{\text{stub1}} \cdot z_{\text{ecal}} + z_{\text{stub1}} \cdot r_{\text{ecal}}}{r_{\text{ecal}} - r_{\text{stub1}}} \quad (5.5)$$

Z_{miss} depends strongly with η of the electron as shown in Figure 5.15. There is some dependence also on the radial position of the layers. This functional dependence has been taken care of while selecting the stub-doublets and is shown by a solid red line in the Figure 5.15. For the endcap discs where the z coordinate is fixed and r varies along the disc a R_{miss} parameter is used instead of Z_{miss} . The selection conditions in the

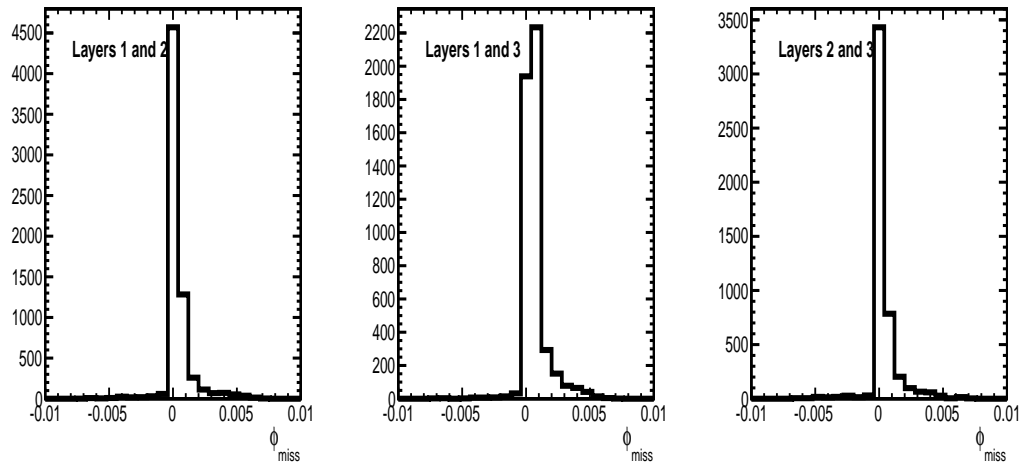


Figure 5.14: ϕ_{miss} distribution for stub-doublets in layer pairs 1st–2nd, 1st–3rd and 2nd–3rd.

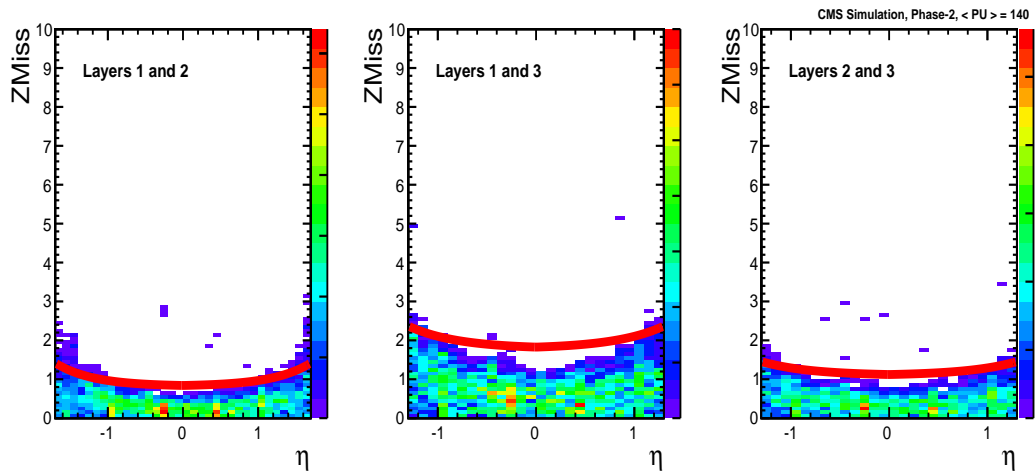


Figure 5.15: Z_{miss} as a function of electron η for stub-doublets in layer pairs 1st–2nd, 1st–3rd and 2nd–3rd.

endcap discs are loose compared to those in the barrel part. If a stub doublet is found in any two of the first three barrel layers or first three endcap discs, their combination are required to have $|\phi_{miss}| < 0.002$. The Z_{miss} or R_{miss} are required to satisfy the condition properly scaled for the layer/disc position and η . Stub pairs satisfying these conditions are considered to be matched with the electron in the calorimeter.

5.4.3 Isolation Requirement on L1EGamma object to Stub Matching

Once stubs matched with L1EGamma objects are found, we further constrain them with the requirement that they should be isolated. Isolation is defined using reconstructed tracks within the annular region around the selected stubs. The relative Isolation I_{rel} is calculated as

$$I_{rel} = \frac{\sum P_{T,Trk}}{E_{T,ecal}} \quad (5.6)$$

where $\sum P_{T,Trk}$ is sum of the transverse momentum of the tracks inside the annular region with Z-vertex constraint ($|\Delta Z| < 0.6$ cm) with respect to the extrapolated z position at the beam line of the stub-doublet. In the analysis we define the annular region as $0.05 < \Delta R < 0.4$ where $\Delta R = \sqrt{(\Delta\phi)^2 + (\Delta\eta)^2}$. It is required that $I_{rel} < 0.15$.

5.4.4 Efficiency and Rate Reduction with L1EGamma object to Stub Matching

The performance in terms of efficiency and the gain in rate reduction is shown in the following figures. The colors of the symbols are similar in all the figures. Red symbols represent the L1EGamma objects, solid black symbols represent the L1EGamma objects

matched with stub doublets (L1StubElectrons) and empty black symbols represent the cases when stub doublets are required to be isolated (L1TkStubElectron_Isolated).

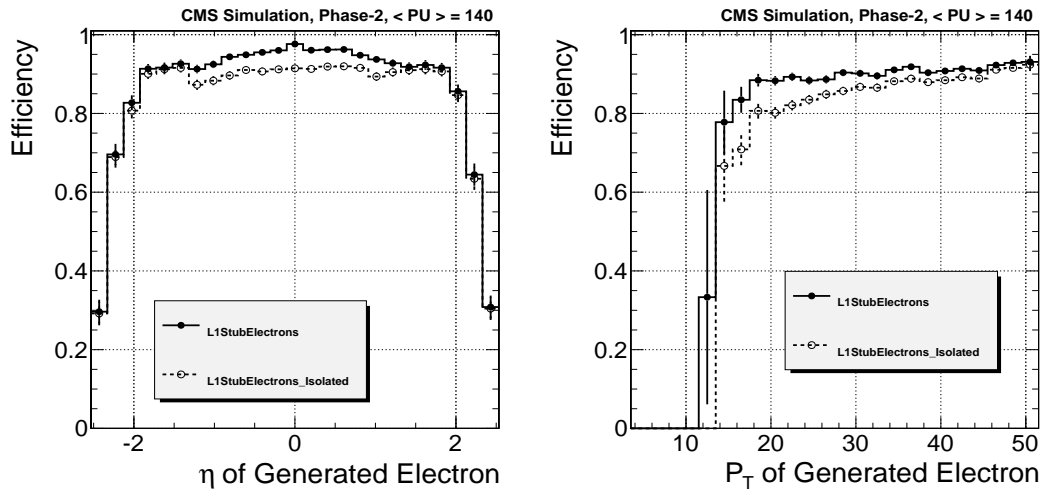


Figure 5.16: The stub-doublet matching efficiency as a function of η (left plot) and transverse momentum (right plot) of the generator level electron are shown. The solid and empty symbols represent efficiency for stubs and isolated stubs respectively. In both cases L1EGamma objects within $|\eta| < 2.5$ are considered and for the η dependence L1EGamma objects required to have $p_T > 20$ GeV. All stub combination from first three layers/discs are considered here.

In Figure 5.16 (left) the stub matching efficiency as a function of generated electron η is shown. In the barrel region $|\eta| < 1.1$, around 95% efficiency with respect to the generated electron has been achieved and it drops beyond $|\eta| > 2$. In the right side distribution of Figure 5.16, the matching efficiency as a function of the transverse momentum of the generated electron is shown. It should be noted that requirement of the isolation condition on the stubs does not degrade the efficiency by more than 3-4%.

In Figure 5.17 the rates of the L1EGamma trigger are shown as a function of transverse energy ($E_{T,ecal}$) measured at the calorimeter. The rates get significantly reduced when we require the matching of the L1EGamma objects with the stub doublets. At an $E_{T,ecal}$ of 20 GeV, the rates we get are presented in the Table 5.1 with the corresponding rate reduction factors. We can reduce the rate by a factor of 3 using non isolated stub

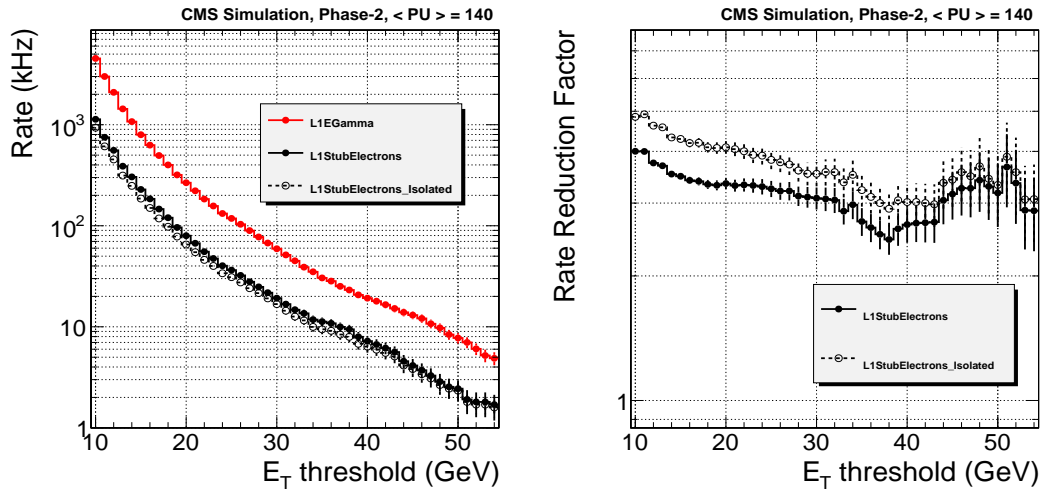


Figure 5.17: The rates of L1EGamma trigger with different matching conditions for stub doublets and isolated stub doublets are shown in the left plot as a function of transverse energy measured at the calorimeter. The rate reduction factors with respect to the L1EGamma objects when matched with stub doublets and isolated stub doublets are shown in the right plot.

doublets, which can go up to 4 requiring isolation condition on the stub doublet. The rate reduction factors are plotted as a function of $E_{T,ecal}$ is shown in the right side of Figure 5.17.

5.4.5 L1EGamma object to Track Matching

In this section we describe the algorithm we have developed to match L1EGamma objects with tracks reconstructed at L1. The performance of tracking at L1 has been discussed in detail in the previous section. To improve the tracking efficiency for electrons, a couple of measures have been taken. The ϕ window to extrapolate the tracklets to the outer or inner layers while doing the tracking has been widened to include tracks that lose energy due to bremsstrahlung and deviate from their original trajectory. The transverse momentum of the tracks measured using only the two innermost stubs is used instead

of the one found from the track fit. Two selection windows to associate the L1EGamma object with the track are deployed as described below. For this matching we require good quality tracks with a transverse momentum requirement, but no χ^2 cut has been applied to have the full advantage of extended ϕ window tracking.

- $\Delta\phi$ is the difference between the propagated ϕ of the track at the calorimeter face and that of the L1EGamma object measured at the calorimeter itself. The propagated ϕ of the track is defined as

$$\phi_{\text{propagated}} = \phi_{\text{trk}} - \phi_{\text{curvature}} \quad (5.7)$$

where $\phi_{\text{curvature}}$ is the deviation in ϕ due to the track curvature while moving from the vertex position to the calorimeter and above relation holds for both positively and negatively charged tracks, as $\phi_{\text{curvature}}$ itself carries a sign with $\frac{E}{|P|}$ where E is energy of the L1EGamma object and P is the track momentum.

- $\Delta R = \sqrt{(\Delta\phi^2 + \Delta\eta^2)}$, where the definition of $\Delta\phi$ is stated above and $\Delta\eta$ is the difference between the track η and the vertex corrected η of the L1EGamma object. Vertex correction of the electron is necessary as η is measured with respect to the origin of the CMS detector.
- It is further required that track transverse momentum $P_{T,\text{Trk}} > 10$ GeV. This turns out to be very crucial to achieve a significant rate reduction. This cutoff is intended for high energy electrons ($E_{T,\text{ecal}} > 20$ GeV).

Figure 5.18 (left) shows the distribution of ΔR variable using single electron events, each superimposed with 140 pile up events, while Figure 5.18 (middle) and Figure 5.18 (right) show $\Delta\phi$ and $\Delta\eta$ distributions, respectively. We have scanned over ΔR and $\Delta\phi$ windows to have an optimal choice of the window size which gives around 90% signal efficiency.

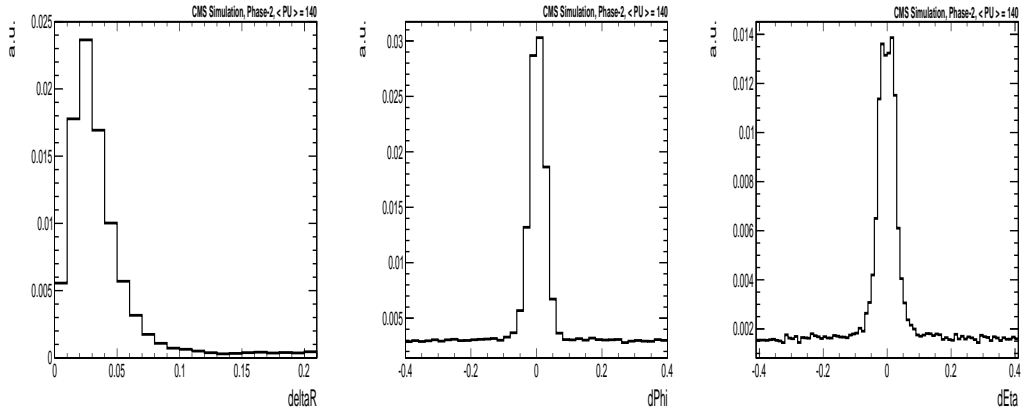


Figure 5.18: ΔR (left), $\Delta\phi$ (middle) and $\Delta\eta$ (right) distributions between the L1 track and L1EGamma object are shown.

We require $\Delta R < 0.08$ and $|\Delta\phi| < 0.07$. A tighter restriction on $\Delta\phi$ has been imposed even after a cut on ΔR that includes $\Delta\phi$, as $\Delta\phi$ looks slightly narrower than $\Delta\eta$ distribution, which improves the rate reduction. A tight quality cut on $P_{T,Trk}$ is essential to achieve significant background reduction. The effect of the $P_{T,Trk}$ cut on signal and background efficiencies are studied and it is optimized to put a 10 GeV cut to retain a 90% signal efficiency working point after track electron matching. In the low transverse energy range where the transverse energy of the L1EGamma object, $E_{T,ecal} \leq 20$ GeV, this tight requirement results in drop of signal efficiency. Hence for the electrons of $E_{T,ecal} \leq 20$ GeV we are applying a relaxed minimum $P_{T,Trk}$ requirement of 3 GeV to have a maximum possible efficiency for the low $E_{T,ecal}$ working point, which will be used for the dilepton triggers or cross object triggers.

5.4.6 Isolation Requirement on L1EGamma object to Track Matching

Once a track matched with the L1EGamma object is found, as refinement, an isolation requirement on this track is imposed. Relative isolation (I_{rel}) is constructed using the

tracks which are inside the isolation annulus and within a z -vertex restriction with respect to the matched track. The isolation annulus inner and outer cones and the z -vertex restriction are optimized in the following way. First the contribution to the relative isolation variable coming from individual ΔR (relative angle in $\eta - \phi$ plane) bins where each bin in ΔR has been used to form an annular isolation cone, is accounted. In Figure 5.19 (left), the x axis represents the annulus ΔR bins and the y axis shows the mean isolation value in the corresponding bins for the $W \rightarrow e\nu + 140$ PU signal events. The lower and upper edges of the ΔR bins are the isolation inner and outer cones respectively.

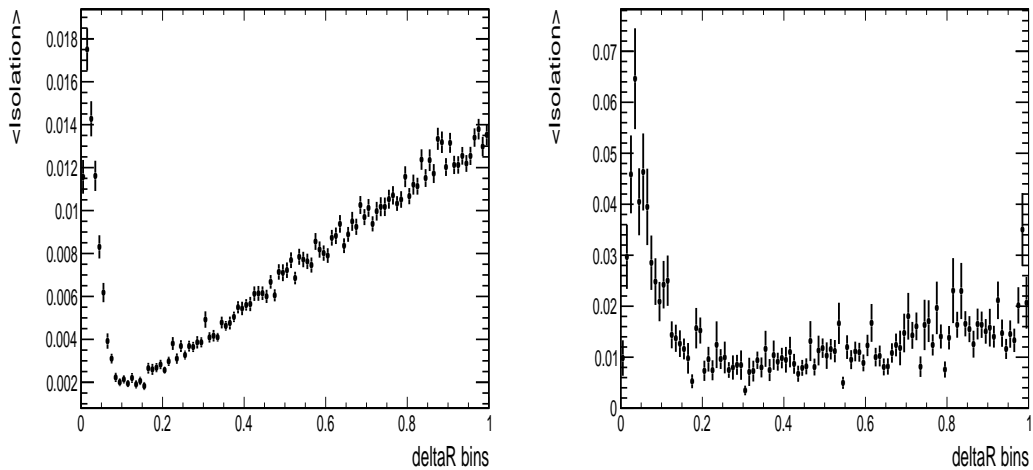


Figure 5.19: The isolation profile as a function of bins in ΔR shown for signal (left) and background (right) events.

In Figure 5.19 (right) the isolation profile for the background events shows that the outer cone of the isolation annulus should be somewhere around 0.2, beyond that it does not give any advantage over the signal distribution. At the same time the isolation profile for the signal distribution indicates that putting the isolation inner cone at 0 would result in a loss of signal efficiency because of the electron conversion footprint. So these plots are used to optimize the range of ΔR bins we should scan for isolation inner

and outer cone. In a similar way we checked the isolation profile as function of ΔZ bins where ΔZ is the z-vertex distance of the candidate track from the one matched to the L1EGamma object. Figure 5.20 (left) and Figure 5.20 (right) show isolation profiles for the $W \rightarrow e\nu + 140$ PU signal events and minimum bias background events respectively.

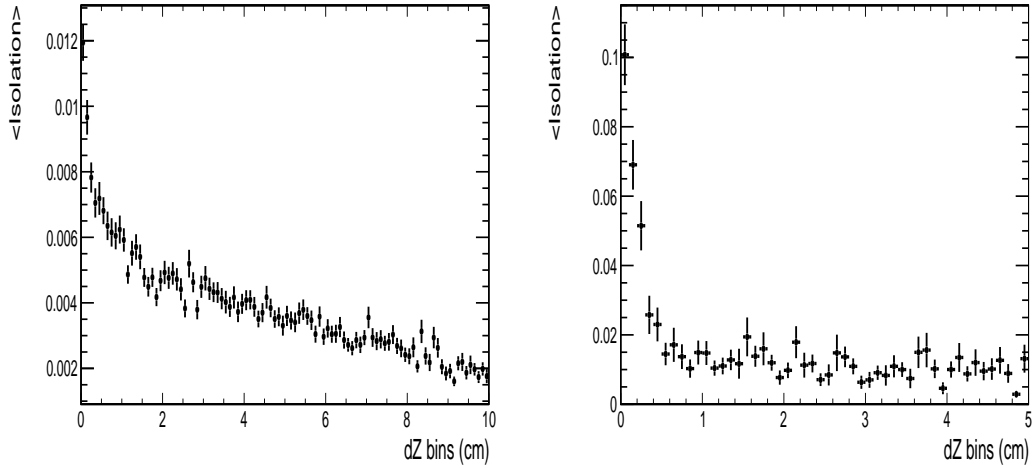


Figure 5.20: Isolation profile as a function of dz bins shown for signal (left) and background (right) events.

The isolation profile for the background events gives us a range of ΔZ values to define the optimal ΔZ cut. Figure 5.21 (left) shows the variation of isolation performance for different isolation inner-cones, keeping the outer-cone fixed at 0.2 and $|\Delta Z| < 0.6$ cm. It is clear that the optimized value of the isolation inner-cone should be 0.03. Similarly, Figure 5.21 (right) shows the variation of isolation performance for different isolation outer-cones, keeping the inner-cone fixed at the optimized value of 0.03 and $|\Delta Z| < 0.6$ cm. In Figure 5.21, signal (x-axis) and background (y-axis) efficiencies are shown for different selection conditions of cone sizes.

Figure 5.22 (left) shows the variation of isolation performance for different ΔZ cuts, where the curve corresponding to the $|\Delta Z| < 0.6$ cm is our optimized one. We further checked the effect of a minimum threshold on the transverse momentum of the track,

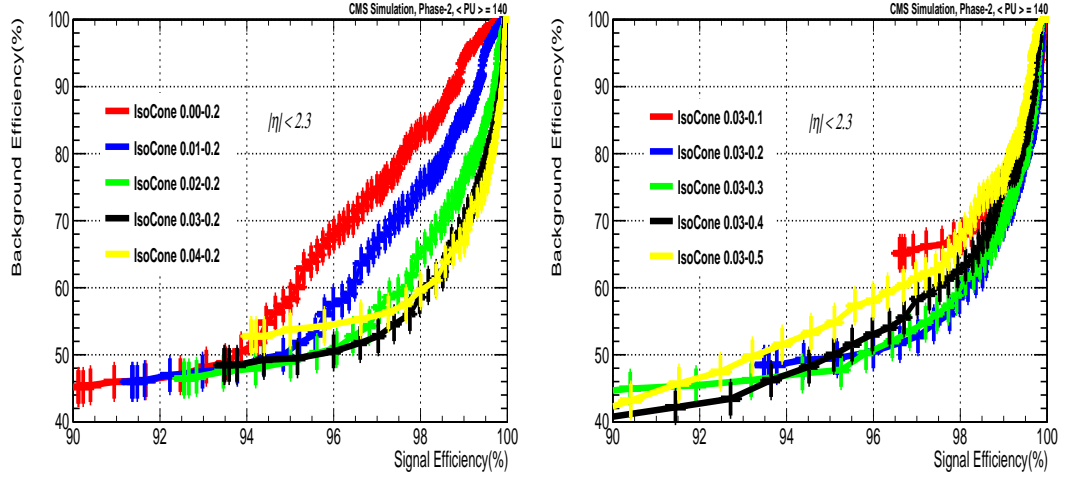


Figure 5.21: The isolation optimization in terms of signal and background efficiencies for isolation inner-cone (left) and outer-cone (right) are shown.

$P_{T,Trk}$ while calculating the relative isolation I_{rel} . In the left plot of figure 5.22 the effect of ΔZ cut off is estimated and the right plot shows the effect of minimum threshold on $P_{T,Trk}$. It can be noted that a minimum threshold on $P_{T,Trk}$ above 2 GeV starts to degrade the isolation performance.

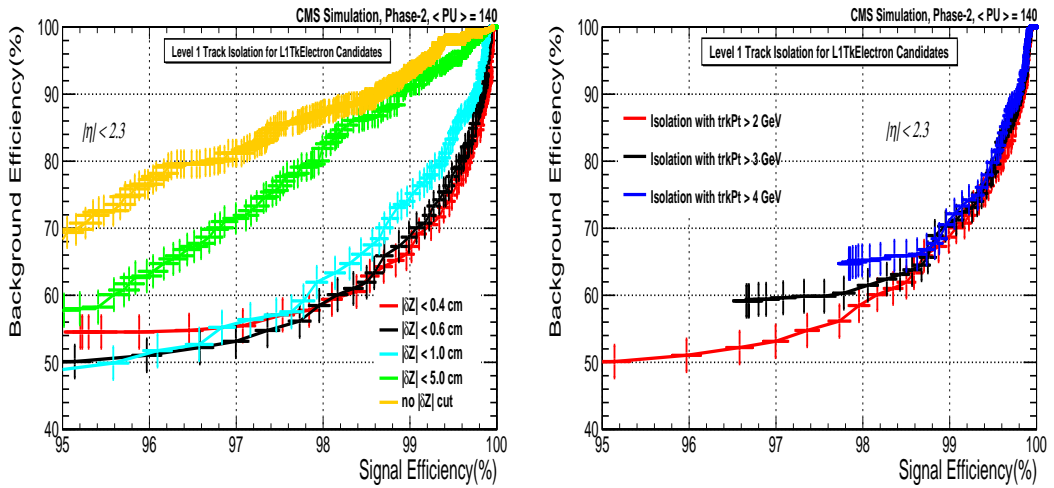


Figure 5.22: The performance of isolation in terms of signal and background efficiencies for ΔZ (left) and the minimum threshold on the transverse momentum of the L1 track $P_{T,Trk}$ (right) are shown.

During the Phase-II, nominal number of interactions per bunch crossing is expected to be around 140. It is also worth while to study how the performance changes when the interaction per bunch crossing hits the upper tail of the Gaussian where this number can be as large as 200. In Figure 5.23 left and right plots show the variation of isolation performance for isolation inner and outer cones respectively at 200 pile up scenario. The optimized value for the isolation cone is 0.03-0.2, similar to the 140 pile up case.

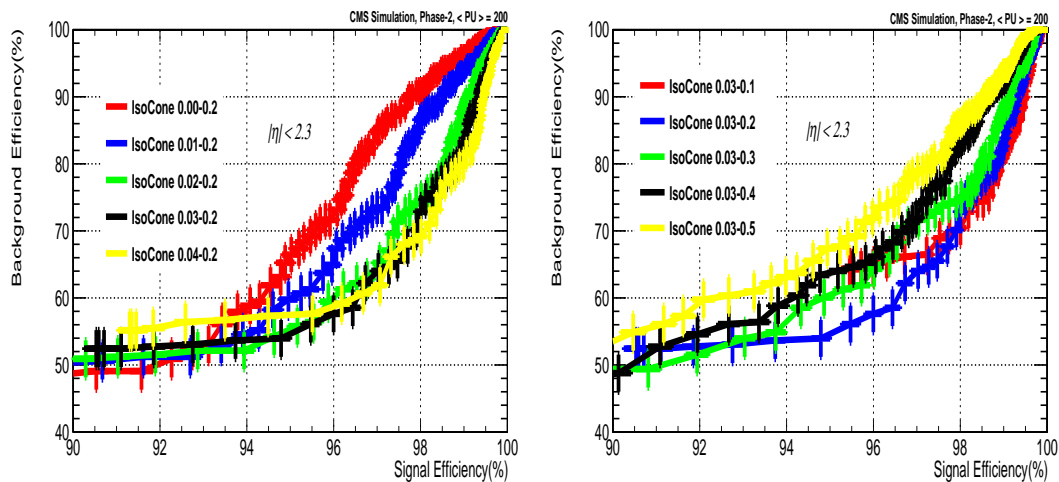


Figure 5.23: The isolation optimization in terms of signal and background efficiencies for isolation inner-cone (left) and outer-cone (right) at 200 pile up are shown.

Figure 5.24 (left) shows the variation of isolation performance for different ΔZ cuts at 200 pile up scenario, where the curve corresponding to the $|\Delta Z| < 0.6$ cm is best performing for $> 95\%$ signal efficiency working points. Figure 5.24 (right) shows signal and background efficiency variation as a function of a cut applied on isolation variable.

Figure 5.25 shows comparison between the isolation performance for 140 and 200 pile up cases. It is evident from the plot that a track-based isolation is still relevant even at 200 pile up scenario.

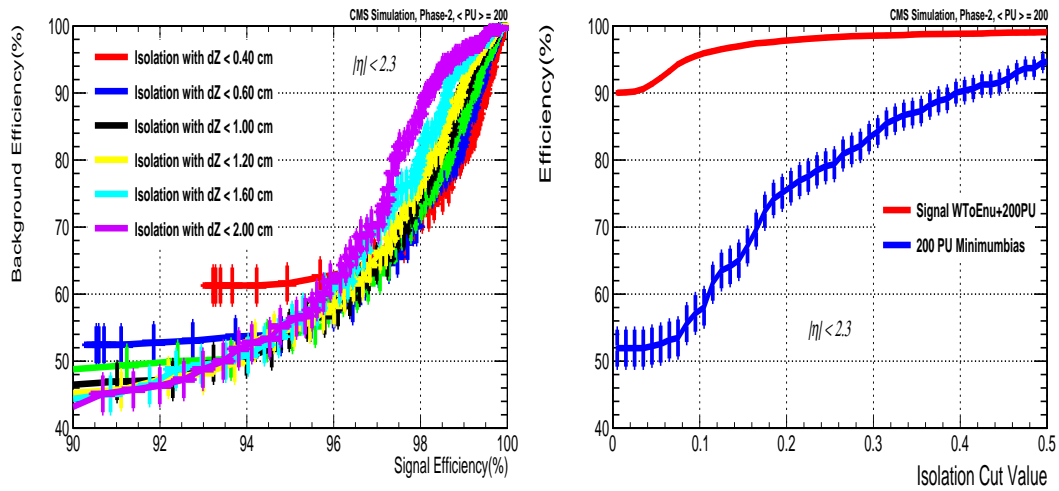


Figure 5.24: The isolation performance in terms of signal and background efficiencies for ΔZ at 200 pile up (left) and variation of signal and background efficiencies as a function of isolation cut (right) are shown.

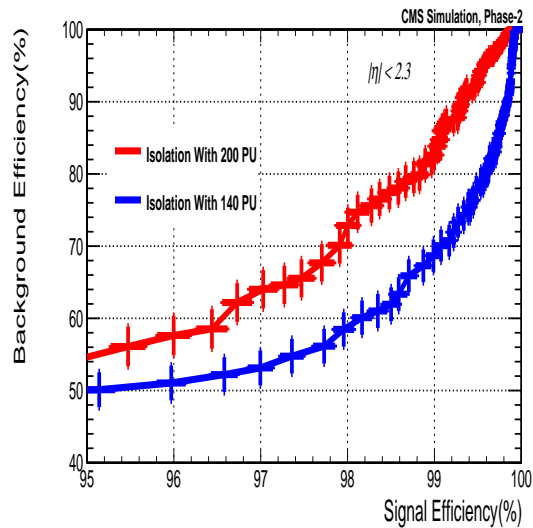


Figure 5.25: Comparison of isolation performance between 140 and 200 pile up scenarios are shown.

5.4.7 Efficiency and Rate Reduction with Electron Track Matching

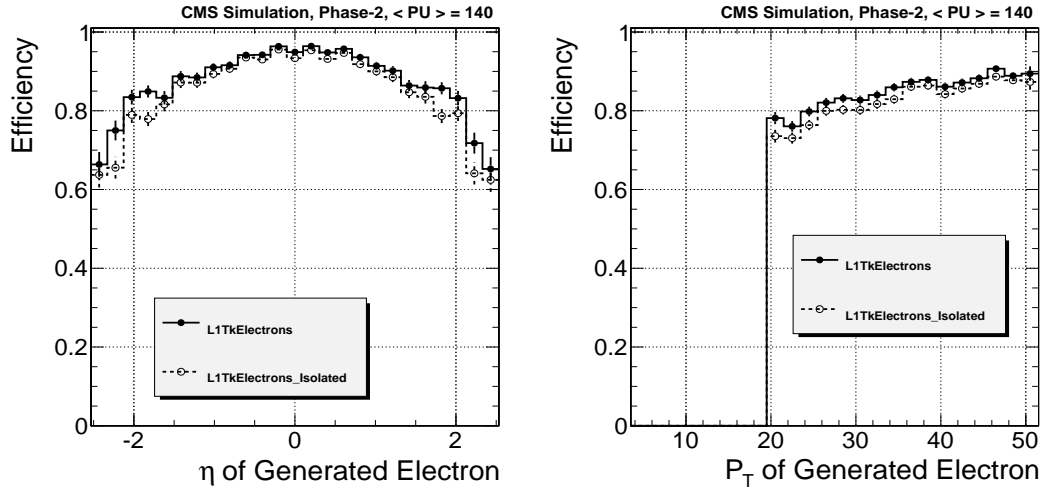


Figure 5.26: The track matching efficiency as a function of η (left plot) and transverse momentum (right plot) of the generated electron. The solid and empty symbols represent efficiencies for non-isolated and isolated tracks respectively.

In Figure 5.26 (left), the efficiency to find a L1EGamma object matched with L1 track (L1TkElectron), is shown as a function of the generated electron η . As can be seen in the barrel region $|\eta| < 1.1$, the efficiency is $> 90\%$ with respect to the generated electron and it drops beyond $|\eta| > 1.1$. In the right plot the efficiency is shown as a function of the transverse momentum of the generated electron. The efficiency drops slightly (2-3%) once track-based isolation is imposed.

Figure 5.27 presents the performance of track matching with L1EGamma object in terms of rate (left) and rate reduction factor at 20 GeV E_T threshold (right). It is visible from the plots that the reduction power of the matching algorithm is significant and a factor 10 is achieved when the track based isolation is imposed.

In Table 5.1, the performance of matching stubs and tracks with L1EGamma object

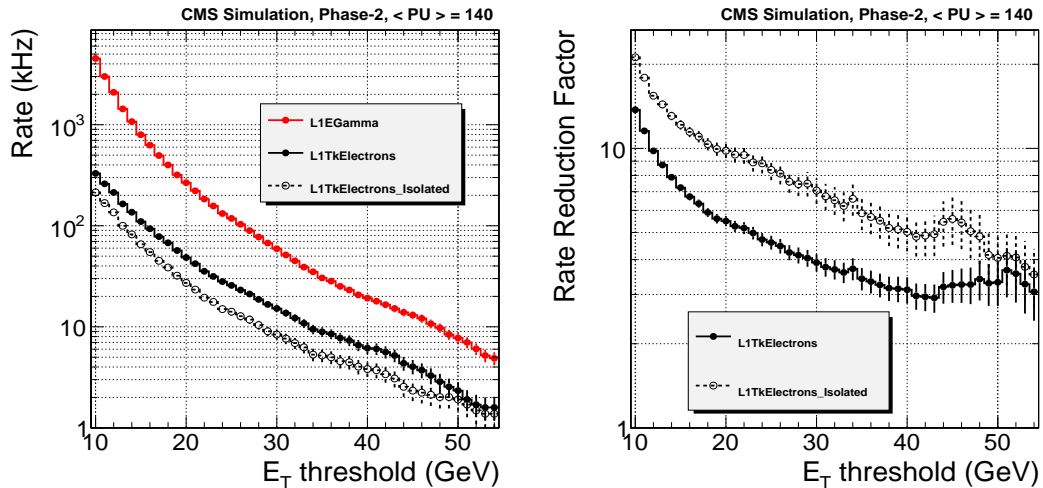


Figure 5.27: Rates (left plot) of L1EGamma trigger with different matching conditions as a function of transverse energy measured in the calorimeter. The solid symbols represent L1EGamma object matched with tracks and the empty symbols represent the matching with isolated tracks. In the right plot the rate reduction factors for these two cases with respect to the bare Level 1 electron are shown as a function of transverse energy measured at the calorimeter.

is summarized in terms of rate and rate reduction factor at 20 GeV E_T threshold. A rate reduction factor of 9.8 has been achieved for the *L1TkElectron_IsoTk* object with respect to the L1EGamma rate at 20 GeV E_T threshold, which was one of the primary goals of this study. The *L1TkStubElectron_IsoTk* object shows powerful performance in terms of rate reduction in the barrel region ($\eta < 1.1$), but is not quite efficient once the endcap is included. All these results are documented in the CMS Detector Note [2].

5.5 Alternative Scenario

The results reported in the previous section are part of the Technical Proposal for Phase-II upgrade of the CMS detector. In defining the scope and extent of these upgrades, the

Type	Rate in kHz @ 20 GeV	Rate Reduction factor @ 20 GeV
L1EG	266.6 (149.3)	
L1TkStubElectron	79.7 (22.8)	3.3(6.5)
L1TkStubElectron_IsoTk	65.2 (14.1)	4.1(10.6)
L1TkElectron	48.5 (20.8)	5.5(7.2)
L1TkElectron_IsoTk	27.2 (9.3)	9.8(16.0)

Table 5.1: Rate of the L1EGamma object is compared with and without matching with L1 tracker objects. First two rows represent the matching of L1EGamma object to the stub-doublets and the last two rows represent the matching with L1 tracks. The Rate Reduction factors in the last column, show the improvement that can be achieved after matching. The numbers inside the bracket correspond to the performance in the barrel region $|\eta| < 1.1$ only.

design choices were made based on considerations of both performance and cost. From the outer tracker design point of view two separate scenarios have been considered for performance studies:

- fewer outer tracker modules, implemented by using a tilted configuration,
- the removal of a layer in the outer tracker.

5.5.1 Performance with Tilted Tracker Design

Tilting modules in the outer part of the tracking system slightly degrades the z-resolution of online track reconstruction. On the other hand a reduction of the material budget leads to a moderate improvement in the offline momentum resolution. A design of outer track layouts with tilted modules are illustrated in Figure 5.28. Events with the default reference geometry for Technical Proposal has been used to emulate the effect of tilted tracker design, i.e to have a degraded z-resolution compared to the reference geometry. In Figure 5.29 (left) a comparison of track-electron matching efficiency is presented

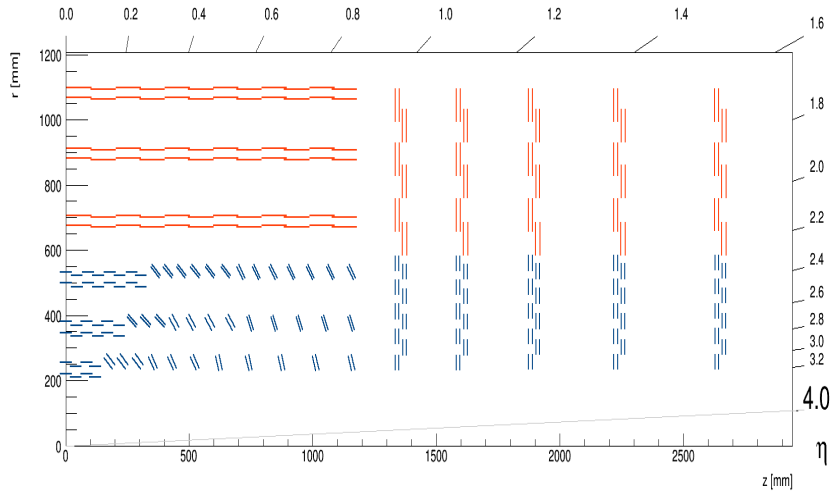


Figure 5.28: r-z view of the proposed BE5D layouts with tilted modules.

using the default (i.e tracks with reference outer tracker design) and degraded tracks for both 140 and 200 pile-up conditions. A similar set of plots are shown on the right side of Figure 5.29 where the track-based isolation requirement is also applied. No visible effect in efficiency is observed with the z-resolution degraded tracks in any of the pile-up conditions.

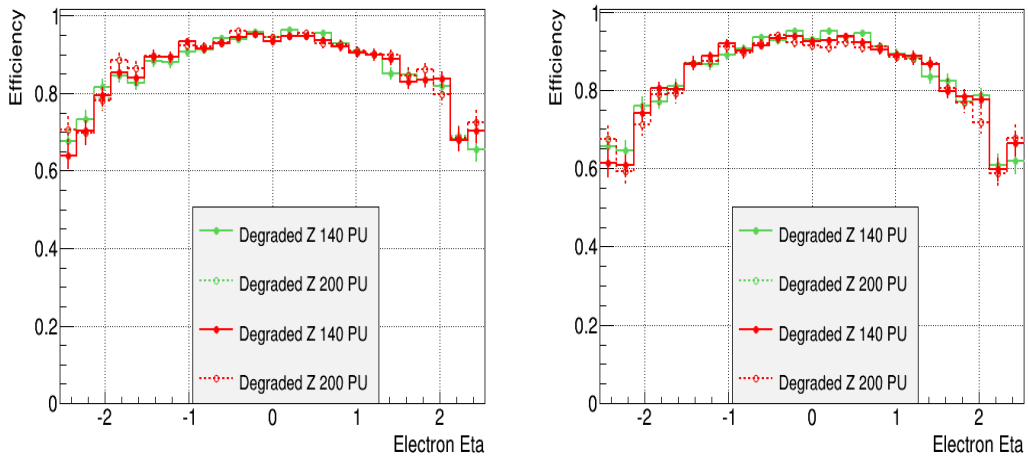


Figure 5.29: Effect of z-resolution degradation on efficiency at 140 and 200 PU

Figure 5.30 shows the performance plots for rates

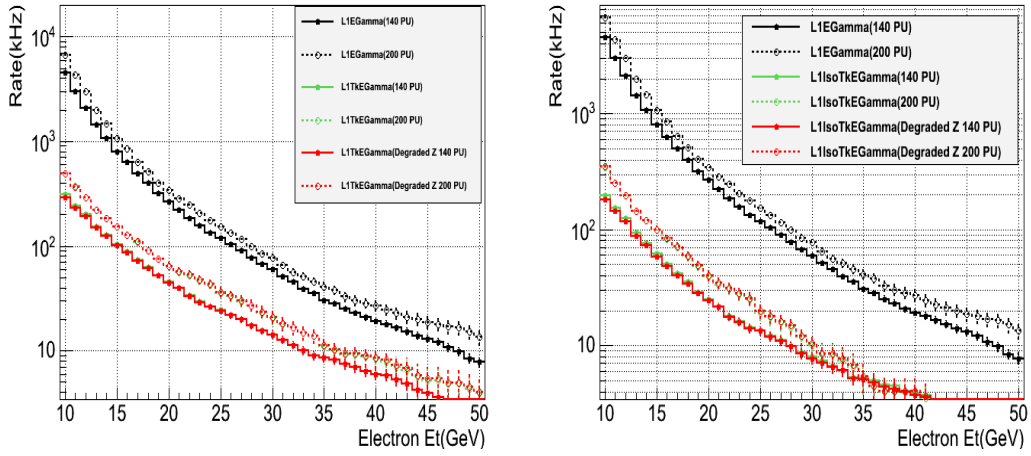


Figure 5.30: Effect of z-resolution degradation on rate at 140 and 200 PU for L1TrkEGamma (left) and L1IsoTrkEGamma (right) objects.

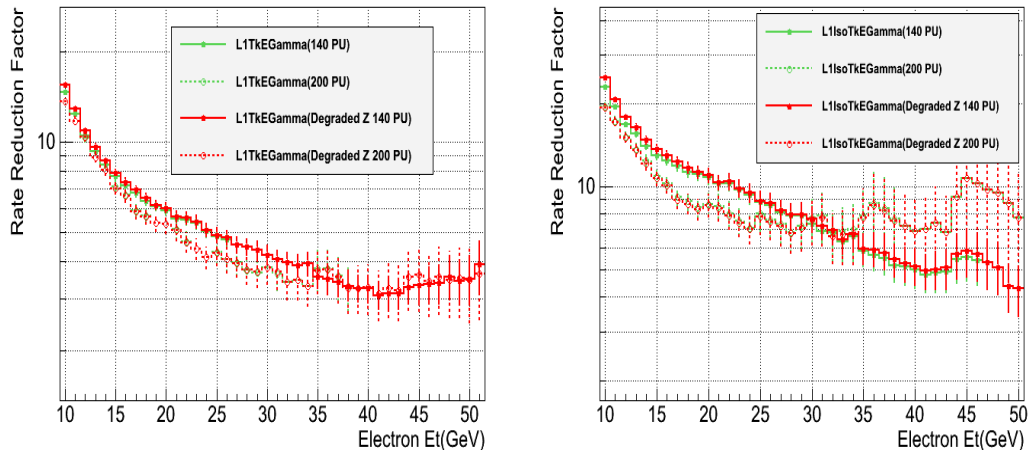


Figure 5.31: Effect of z-resolution degradation on rate reduction at 140 and 200 PU for L1TrkEGamma (left) and L1IsoTrkEGamma (right) objects.

5.5.2 Performance with 5 Layer Outer Tracker

In the descope scenario the other proposed outer tracker design has a reduced number of layers. To simplify the performance studies, layer 4 of the outer tracker has been removed

without changing the other layer configuration. Layer 4 is chosen because it minimizes the impact on track reconstruction performance. Now, for L1 track finding only the outer tracker hits are used, the absence of a layer induces inefficiency in track reconstruction. It is expected to have a visible impact on the track-electron matching performance in 5 layer configuration. A set of high level performance plots are presented below to compare the performance. No re-optimization has been done to make the L1 track-electron candidate and track based isolation variable with the 5 layer sample, rather the same working point presented in Technical Proposal has been used. In Figure 5.32 the efficiency of track-electron matching is compared between the default and 5 layer descoped scenario (left). The plot on the right in Figure 5.32 shows a similar comparison but also includes isolation. As can be seen from these plots, the efficiency for track-electron matching is slightly affected in the 5 layer configuration for the same selection.

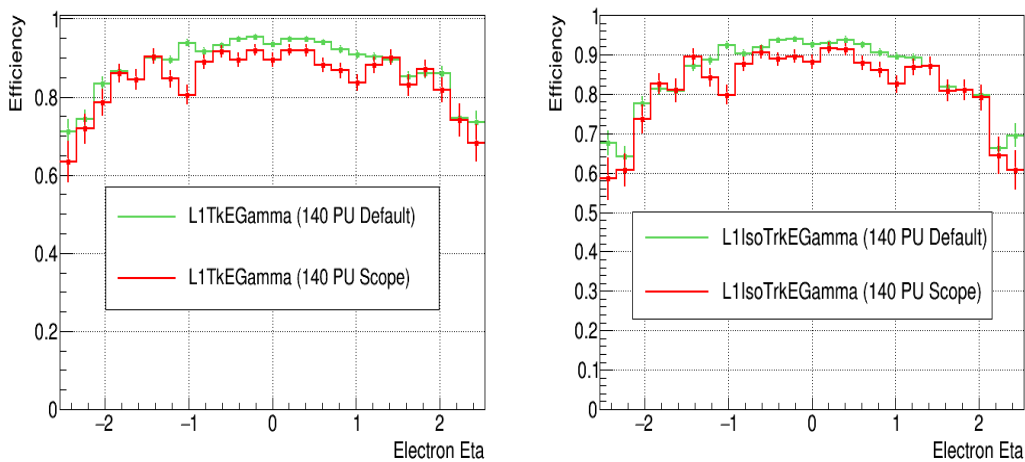


Figure 5.32: Effect of one missing layer on efficiency of L1TrkEGamma (left) and L1IsoTrkEGamma (right) at 140 PU

Figure 5.33 shows a comparison between the default and 5 layer descoped option only for the isolation selection. There is no visible difference in efficiency between the two cases. Figure 5.34 left and right plots show the rates corresponding to track-electron

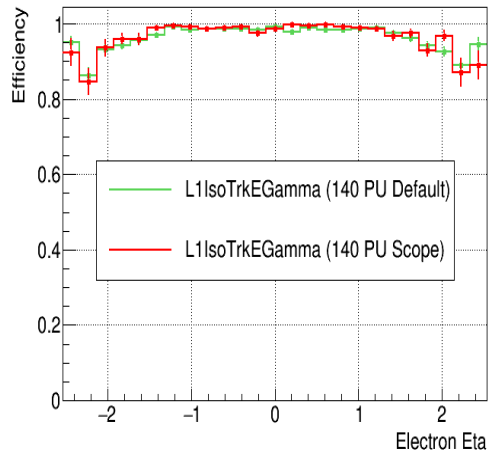


Figure 5.33: Effect of one missing layer on isolation performance only at 140 PU

matched and isolated objects respectively. Since the track-electron matching efficiency in Figure 5.32 (left) is higher for default reference geometry, it is expected to have a higher rate for this object. Electron calo rates labeled as L1EGamma show some discrepancies at a higher transverse energy threshold and it is understood to be an effect coming from the pile-up recycling of 5 layer minimum bias sample, which is not present in the default reference sample. Since the missing 4th layer effectively reduces the material

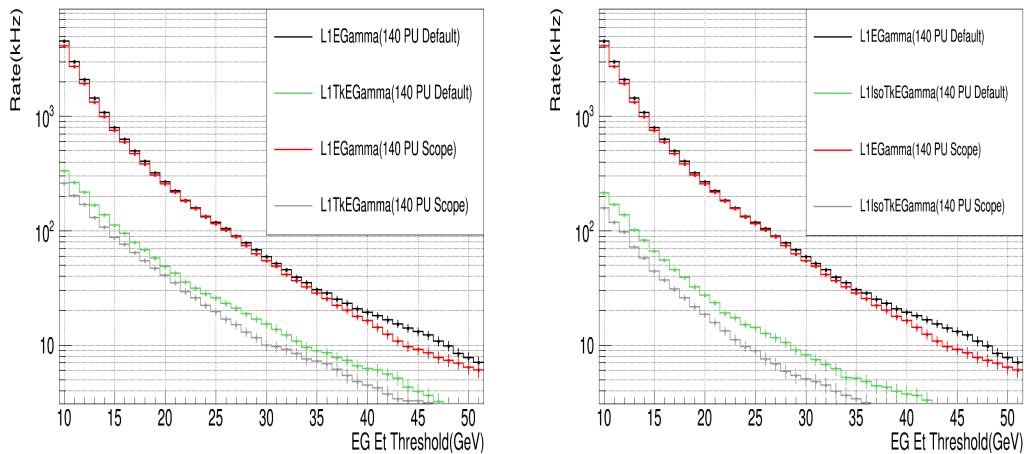


Figure 5.34: Effect of one missing layer on rates of L1TrkEGamma (left) and L1IsoTrkEGamma (right) at 140 PU.

budget in the central η region the rates were checked separately for the central and endcap region to spot any possible differences, as shown in Figure 5.35. Rates below 10 kHz are statistically weak to conclude any possible feature. Figure 5.36 shows similar

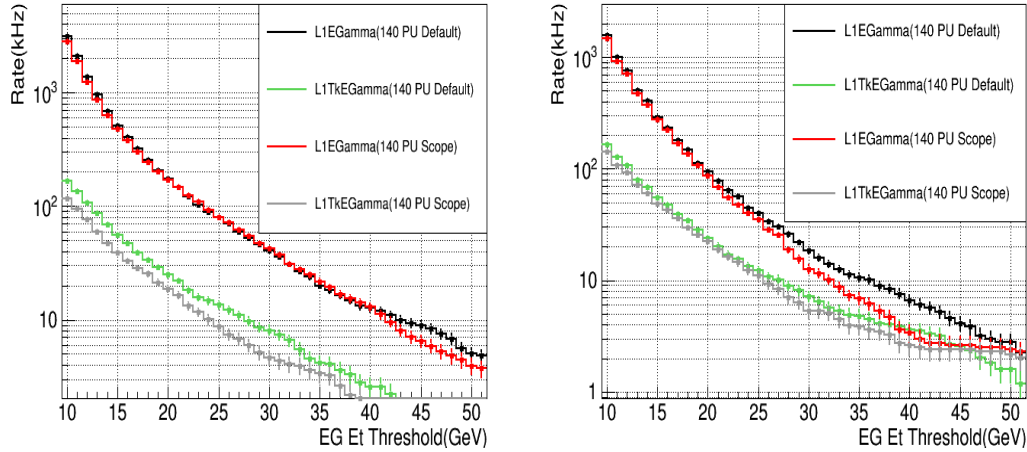


Figure 5.35: L1TrkEGamma rate comparison for 5 layer configuration at 140 PU in central (left) and endcap (right) pseudorapidity.

rate comparison for isolated candidates in split η region. Rate reduction factors are

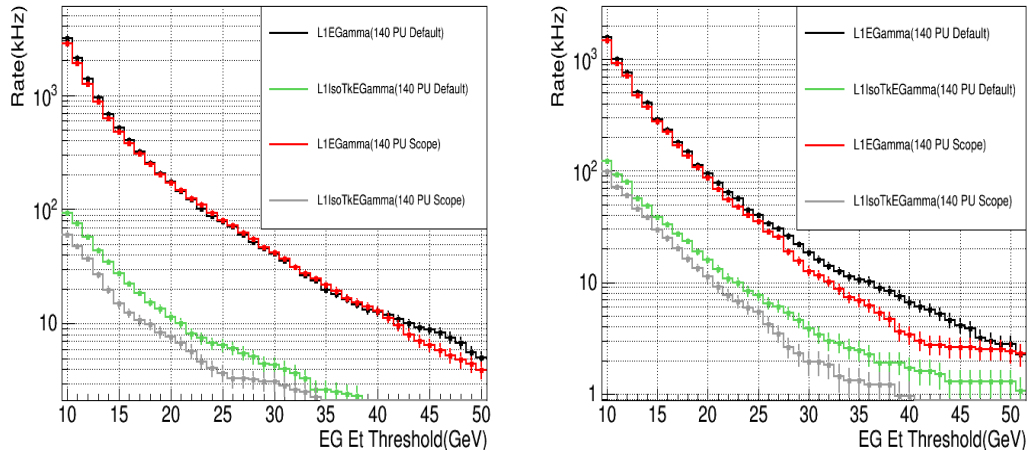


Figure 5.36: L1IsoTrkEGamma rate comparison for 5 layer configuration at 140 PU in central (left) and endcap (right) pseudorapidity.

plotted as a function of the transverse energy threshold in Figure 5.37. L1TrkEGamma

candidates for 5 layer set-up shows a higher rate reduction factor since it has lower efficiency to start with. So it is not a fair comparison and things look pretty much consistent. But L1IsoTrkEGamma shows slightly better performance for 5 layer set-up and it is attributed to the statistical discrepancy only.

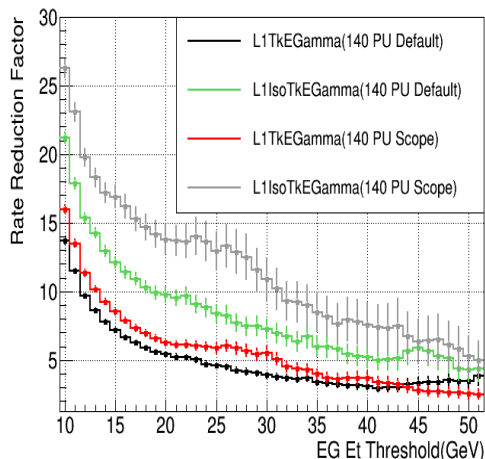


Figure 5.37: Rate Reduction factor at 20 GeV transverse energy threshold comparing 5 layer configuration with the reference geometry.

Bibliography

- [1] “Technical Proposal for the Phase-II Upgrade of the CMS”, CMS-TDR-15-02
- [2] “Use of tracking in the CMS L1 trigger for the phase-2 upgrade”, CMS DN-14-002
- [3] Laura Fields, Nicola Pozzobon, Anders Ryd, Emmanuele Salvati, “Simulations Studies of Stacked Track Trigger Modules”, CMS Detector Note CMS DN-2012/003

Associative Memory based Tracking at Level 1 Trigger

6.1 Introduction

As already has been discussed in the previous chapter, the planned Phase-II upgrade [1] of the CMS detector foresees a major development on the trigger system to counter the unprecedented instantaneous luminosity expected in p-p collisions during HL-LHC. The proposed new tracker will be designed upfront to have the added capability of on-detector tracking which is expected to make track reconstruction at L1 a reality. In the previous chapter, the prospect of using track-trigger for electrons at L1 is dicussed where it is shown that once calorimeter electrons are combined with L1 tracks, electron rates

are reduced significantly at the same transverse energy threshold. The purpose of this chapter is to present one of the proposed track reconstruction methods in L1.

Currently, there are a number of different approaches that are being considered for tracking at L1, namely

- *Tracklet-based tracking*: This is a traditional approach for track reconstruction. The algorithm and performance of this approach have been discussed in the previous chapter where the electron track trigger algorithm was designed using the tracklet based tracks.
- *Associative Memory based tracking*: In this approach tracking works in two stages. Firstly, Associative Memory (AM) based pattern matching removes the unwanted hits (stubs) and then a fitting method is run on the filtered hits (stubs) to reconstruct tracks. Current chapter deals with the AM based tracking at L1.

The above approaches should be able to work in real-time on electronic components, e.g. FPGAs (Field Programmable Gate Arrays). This will impose very tight constraints on the available algorithms for pattern recognition and track fitting. Figure 6.1 shows the CMS data flow for the L1 track trigger. During Phase-II, it is expected to have an average L1 latency of $\sim 10 \mu s$. Stubs will be transmitted by the front-end drivers to the L1 tracking system which is supposed to produce L1 tracks within a latency of $5 \mu s$. Once the tracks are reconstructed, L1 information from other sub-detectors are combined to produce the overall L1 trigger decision which eventually initiates the High Level Trigger (HLT) sequence.

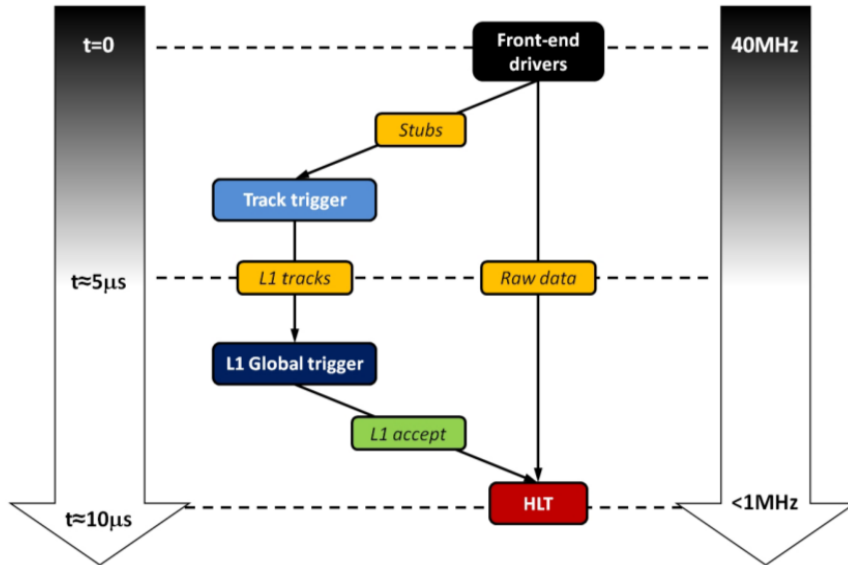


Figure 6.1: CMS data flow for L1 track trigger

6.2 Associative Memory based Pattern Recognition

In this section the concept and performance of the software emulation of the AM based **Pattern Recognition (PR)** technique is discussed [2-4]. Pattern Recognition only activates the matched patterns with hits (stubs) that are correlated and compatible with a single track. This way, a much reduced set of hits (stubs) are available for fitting within the stipulated time constraint. A **Principal Component Analysis (PCA)** based fitting technique has been adopted as a baseline choice. In the present work, the floating point and integer based fixed point emulation of PCA algorithm have been studied.

It is known that the expected stub rate with 140 pile-up will be quite high and it is practically not possible to perform pattern recognition for the entire detector by a single PR unit. The task of pattern recognition in the entire outer tracker is split into

48 sectors, 6 in η direction and 8 in ϕ direction. In Figure 6.2 the upper half of the r-z view of the outer tracker detector is shown with the 6 η divisions.

For each η sector there are 8 ϕ slices. There are three kind of sectors (towers),

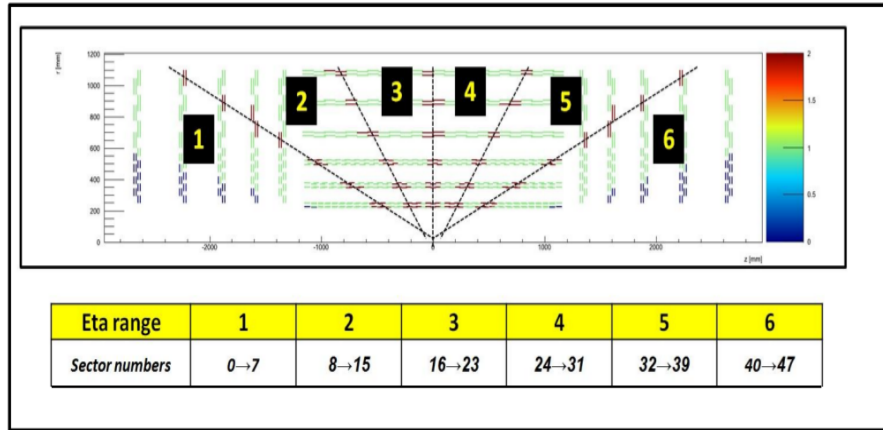


Figure 6.2: Sector definition of the outer tracker detector

- Barrel Towers: Sectors 16-31. Cover barrel layers only.
- Hybrid Towers: Sectors 8-15 & 32-39. These towers have both barrel and disc type layers. The number of layers crossed by a charged track also depends on the η direction.
- Endcap Towers: Sectors 0-7 & 40-47. These type of towers only have disc layers.

Associative memories offer a linear solution to the pattern recognition problem, which is very relevant in HL-LHC conditions. Use of associative memories to perform a fast pattern recognition at the trigger level was first presented in [2]. The basic principle is sketched in Figure 6.3. The idea is to compare the hits (stubs) of the tracker with the bank of patterns pre-stored in associative memory chips. The patterns could be

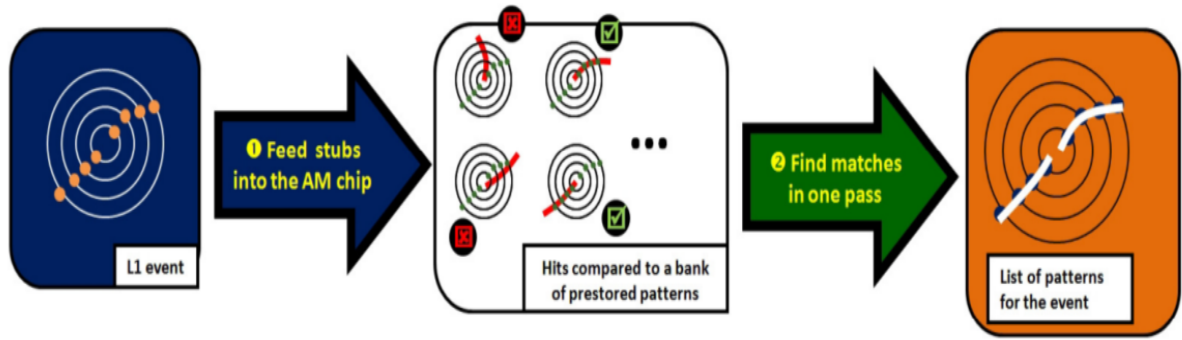


Figure 6.3: A schematic view of the associative memory based pattern recognition

seen as low-granularity tracks, defined once for all using Monte Carlo events. Banks are supposed to contain all the possible tracks occurring in the detector. Each of the 48 towers has its own optimized pattern bank. There are several parameters which have to be tuned to optimize the banks. A good pattern bank should be small, efficient and have a high filtering power. Figure 6.4 shows the filtering power of a typical AM based pattern recognition step with respect to the original hits (stubs) in the $r - \phi$ view.

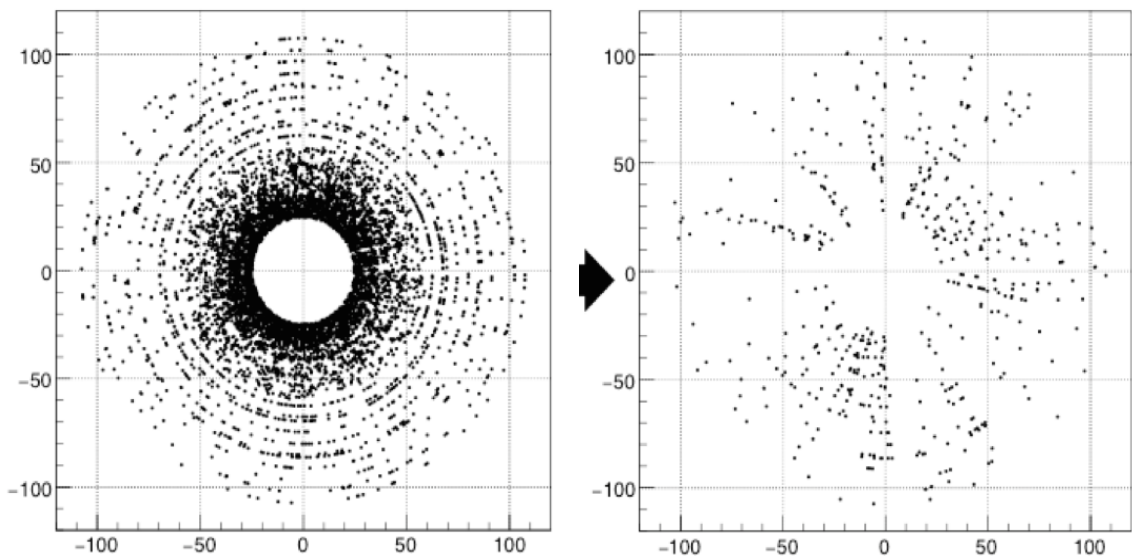


Figure 6.4: Filtering power of AM-based pattern recognition technique. It shows the tracker hits (stubs) in the $r - \phi$ view before (right) and after (left) the pattern recognition step.

6.3 Principal Component Analysis Track Fitter

The problem of fitting the filtered hits (stubs) coming out of the pattern recognition stage is split into two sub-problems to reduce the complexity of the electronics to be used.

- Plane $r - z$: There are a total of 12 coordinate hits (r_i, z_i) corresponding to 6 stubs, where i refers to the individual stubs. The two parameters that are needed to be determined in this plane are z_0 , the z-vertex position and η , the pseudo-rapidity of the fitted track.
- Plane $r - \phi$: Similarly, in this plane as well there are 12 coordinates $(r_i - \phi_i)$ corresponding to 6 stubs referred by i . In this plane the charge over pt ($\frac{c}{p_T}$) and the ϕ values of the tracks are required to be estimated.

There exists a linear relationship between the stub coordinates and the corresponding track parameters (p_i) , e.g.

$$p_i \sim \sum_j A_{ij} x_j + q_i, \quad (6.1)$$

where i stands for the track parameters ($i = 1, 2$) and j represents the 12 stub coordinates. A_{ij} and q_i are constants valid in a sector and x_j are the input stub coordinates.

The multiplicative constant A_{ij} can be expressed as,

$$A_{ij} = \sum_m V_{jm}^{-1} (\langle x_m p_i \rangle - \langle x_m \rangle \langle p_i \rangle), \quad (6.2)$$

where m runs over the number of stub coordinates and the covariance matrix V_{jm} is obtained as,

$$V_{jm} = (\langle x_j x_m \rangle - \langle x_j \rangle \langle x_m \rangle) \quad (6.3)$$

The values of the constant A_{ij} can be plugged into the following equation to estimate the q_i constants,

$$q_i = \langle p_i \rangle - \sum_j A_{ij} \langle x_j \rangle, \quad (6.4)$$

where the averages are taken over the training muons.

From the covariance matrix it is possible to evaluate a quality parameter that in the limit of the validity of the linear approximation is distributed as a χ^2 and can be calculated as,

$$\chi^2 = \sum_{i,j=0}^N (x_i - \langle x_i \rangle) V_{ij}^{-1} (x_j - \langle x_j \rangle) \quad (6.5)$$

A full sector covers quite a large detector region where the linear approximation does not hold to give good parameter resolution. So for each sector, constants are produced in several bins of parameter values. In the $r - \phi$ plane constants are produced in 7 pt bins ranging from pt (3, 200) GeV/c and separately for both the charges, while in $r - z$ plane there are 20 bins in η . Constants are generated assuming muon tracks with their known parameter values and stub coordinates. This is the training part of the fitting procedure. Once the set of constants are there, stub coordinates are passed through Eq. 6.1 to have the best expected value of the track parameters. ATLAS adopted a similar technique for their **Fast Tracker** [2].

PCA based track parameter resolutions are estimated for a barrel sector (Sector 18) using floating point emulation (C++ based algorithm) and are shown in the following distributions. Figure 6.5 shows the resolutions for two parameters, $Cot(\theta)$ and z vertex,

in the $r - z$ plane as a function of the η bins. Resolution values are extremely powerful and ranges between 0.0023 - 0.0024 for $Cot(\theta)$ i.e., η and 0.8 - 0.9 mm for z-vertex.

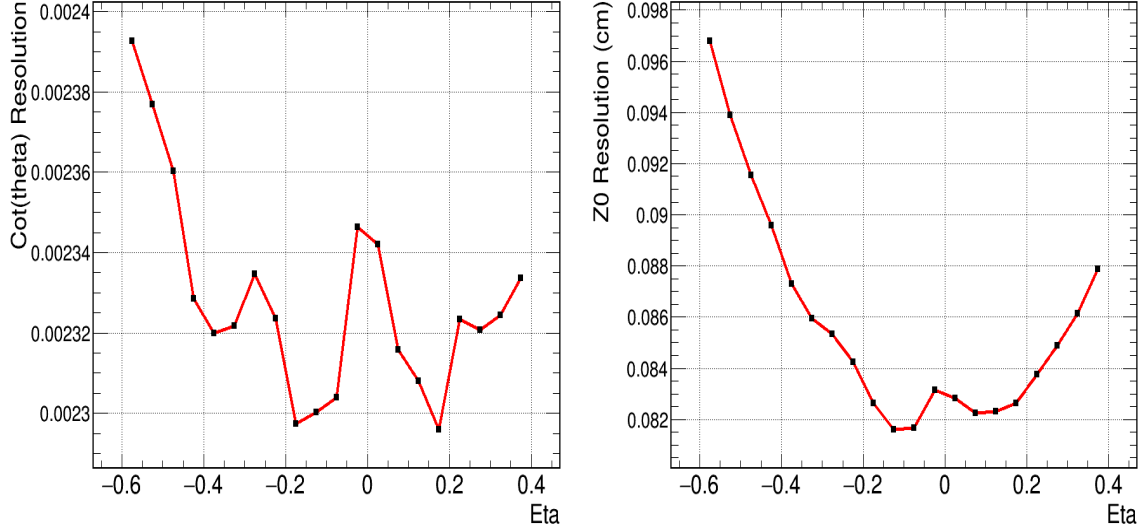


Figure 6.5: Parameter resolutions in $r - z$ plane for $Cot(\theta)$ and Z vertex.

Figure 6.6 presents the resolutions for two parameters, ϕ and $\frac{C}{p_T}$, in the $r - \phi$ plane as a function of the p_T bins. As expected, for the higher p_T bins ϕ resolution reaches a plateau at ~ 0.2 mrad. Relative $\frac{C}{p_T}$ resolution varies between 0.9 - 3.7 % as function of the p_T bins and shows a degraded performance in the higher p_T bins.

PCA based track fitting method is extremely efficient and fast. Figure 6.7 illustrates the efficiency of the fitting algorithm as function of η and ϕ of the muons with $p_T > 10$ GeV/c. As can be seen, the efficiency is $\sim 99\%$ and does not depend on the η and ϕ positions.

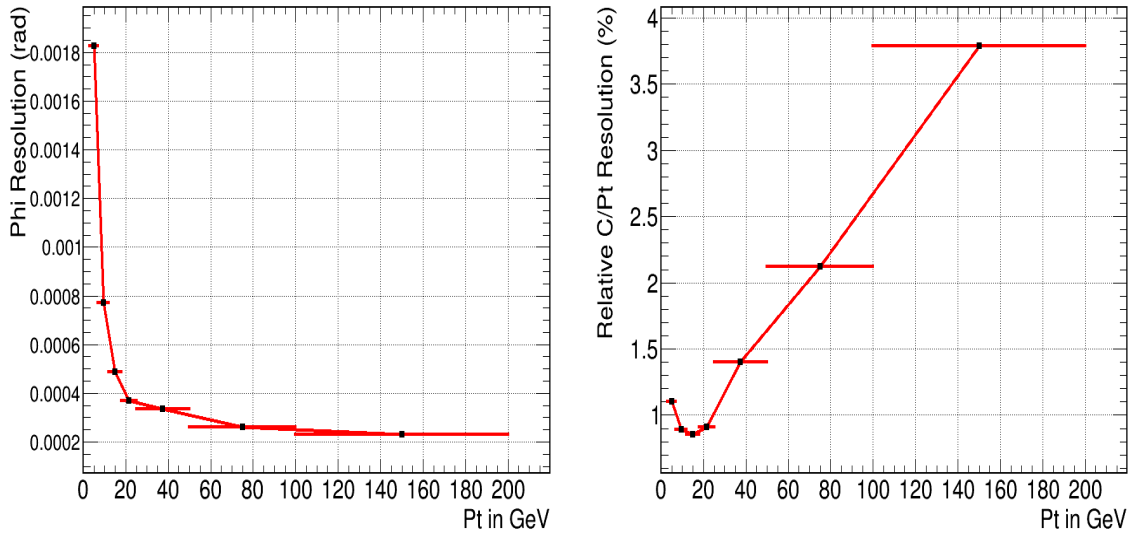


Figure 6.6: Parameter resolutions in $r - \phi$ plane for ϕ and $\frac{C}{p_T}$.

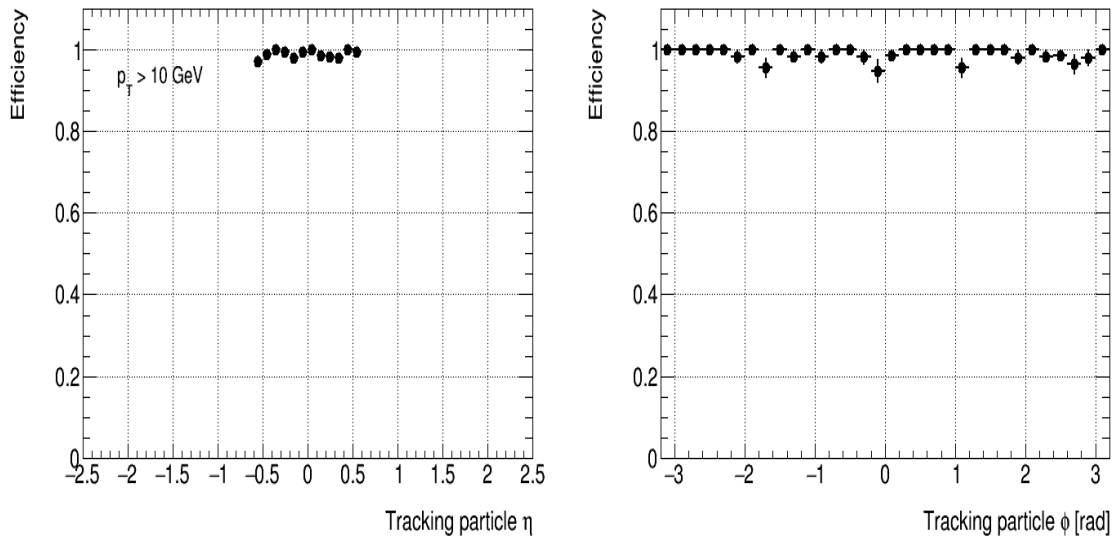


Figure 6.7: PCA Track fitter efficiency for the barrel sectors as a function of η (left) and ϕ (right).

6.3.1 Integer based algorithm

In the floating point emulation of the fitting algorithm, parameter types are assumed as **double** where each parameter consumes 64 bits of memory. The PCA based algorithm is supposed to be integrated on a fast processing hardware, e.g FPGAs that does not support double precision to reduce memory usage. An **integer** based fixed point representation of the PCA algorithm was found to be necessary to reduce the memory usage and fit within the FPGA limit.

Digital Signal Processing (DSP) functions in FPGA work best when multiplications are performed in 25×18 bit size. In Eq. 6.1, the multiplicative constants A_{ij} are assigned 18 bits and stub coordinates are represented by 25 bits. The q_i constants are also represented in 25 bits. A plain **double** to **int** data type conversion does not work and needed to be multiplied by a scale factor to make the integers non-zero. These scale factors are determined by examining the parameter ranges in the particular bin which has been considered to produce the constants. The goal is to emulate the PCA based fitting algorithm using these integer based fixed point representation and try to retain the same performance as of the floating point algorithm.

Figure 6.8 shows the resolution for $Cot(\theta)$ and z vertex in the $r-z$ plane as a function of the η bins for the integer based fixed point algorithm, and have been compared with the corresponding floating point results. The agreement between the two approaches can be seen to be very close.

Along with the resolution, it is also necessary to check whether the fit has introduced any bias on the parameter values. The mean of the difference between the fitted and

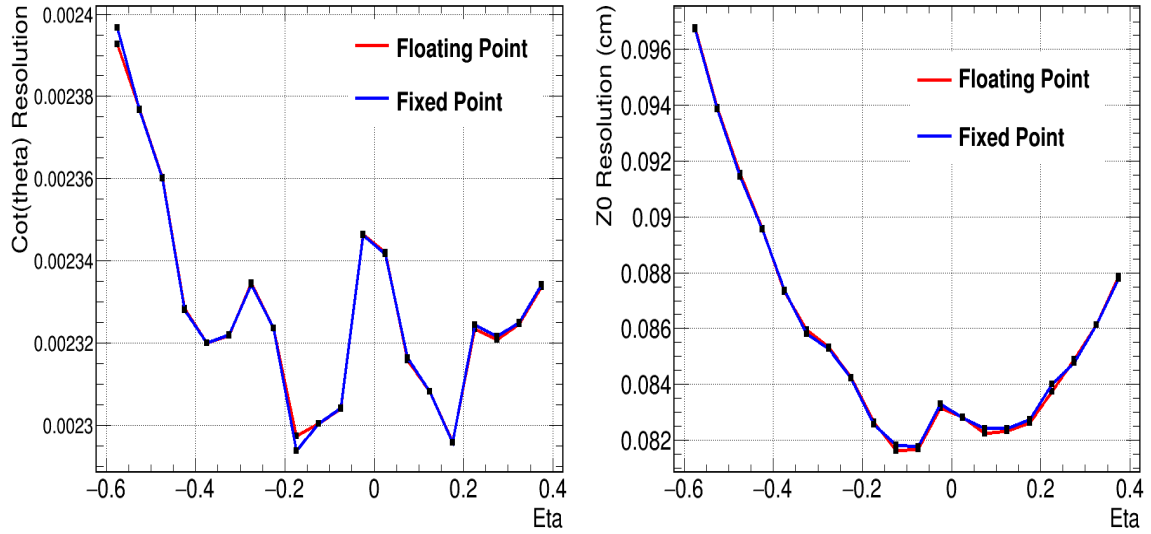


Figure 6.8: Comparison of parameter resolution in $r - z$ plane for $Cot(\theta)$ and Z vertex using the fixed and floating point representations.

true parameters is taken as bias for each bin. Figure 6.9 shows the bias distributions for the two parameters in $r - z$ plane. Bias values are extremely small and no further correction is needed.

Similarly, Figure 6.10 compares the resolution values for the two parameters in $r - \phi$ plane and here also they agree extremely well.

Figure 6.11 presents the bias values for ϕ and $\frac{C}{p_T}$ for fixed and floating point algorithms. Though there are some trends in the distribution, bias values are small and can be safely ignored.

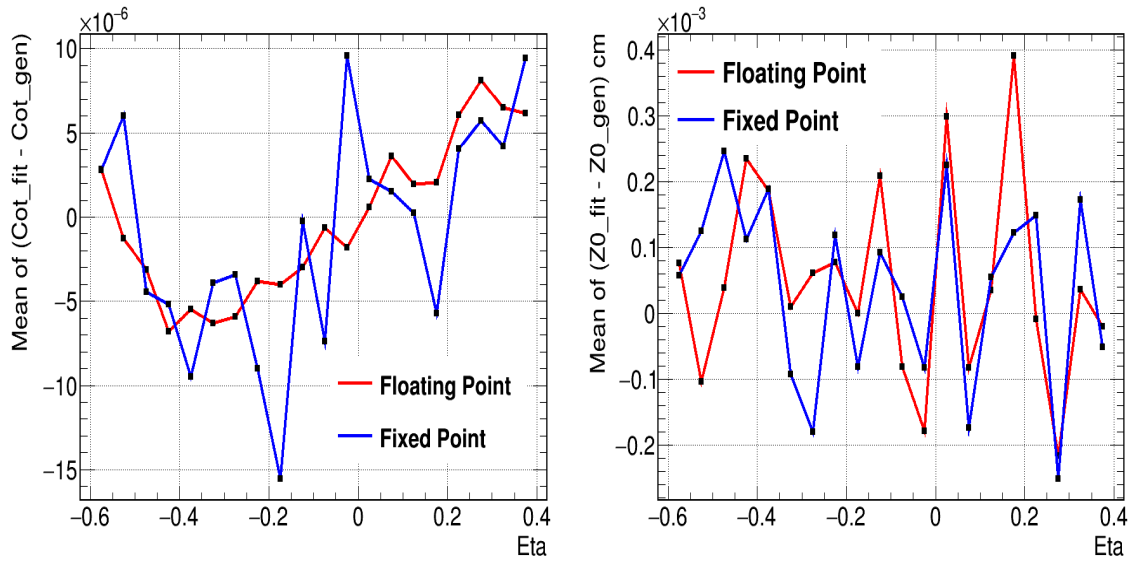


Figure 6.9: Comparison of parameter bias in $r - z$ plane for $Cot(\theta)$ and Z vertex using the fixed and floating point representation.

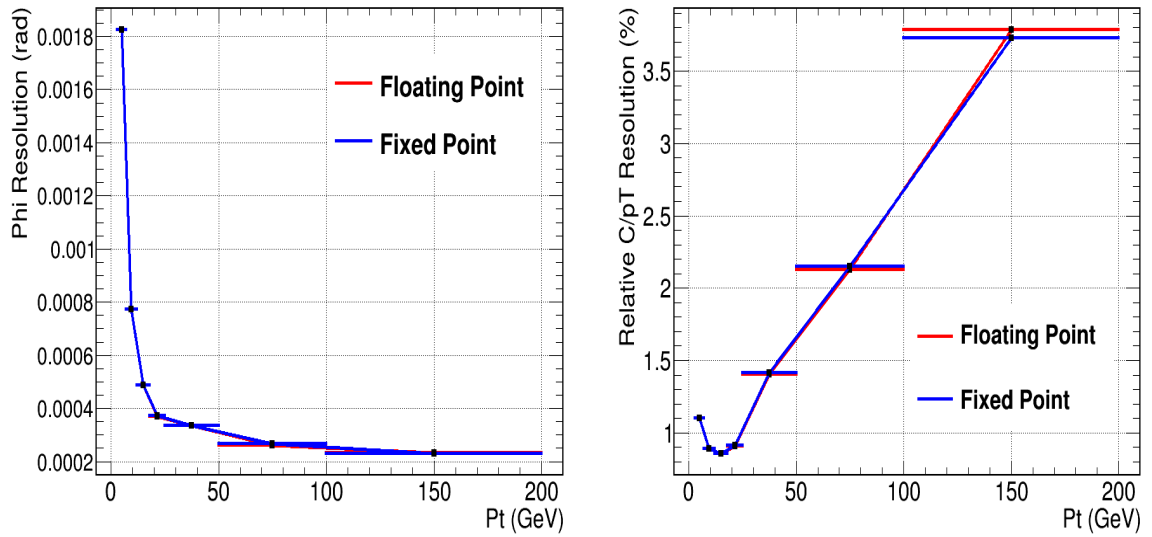


Figure 6.10: Parameter resolution in $r - \phi$ plane for ϕ and $\frac{C}{p_T}$. Resolution values are compared between the fixed and floating point representations of the PCA based track fitter.

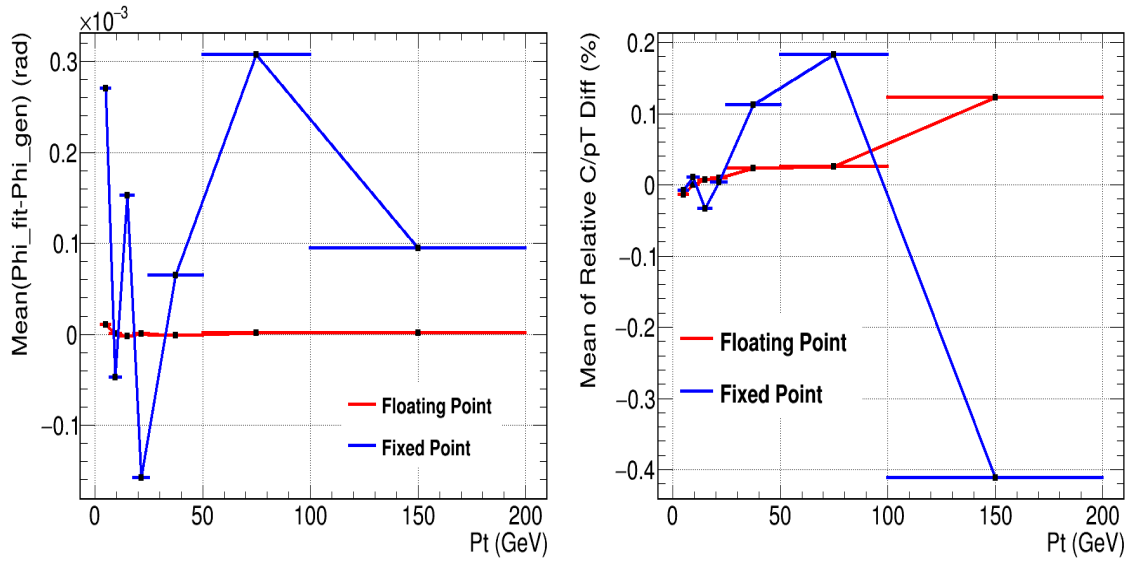


Figure 6.11: Parameter bias in $r - \phi$ plane for ϕ and $\frac{C}{p_T}$, comparing the fixed and floating point algorithms.

Bibliography

- [1] CMS collaboration, “Technical Proposal for the Phase-II Upgrade of the CMS”, CERN-LHCC-2015-10
- [2] ATLAS collaboration, “Fast TracKer (FTK) Technical Design Report” - CERN-LHCC-2013-007 - 2013
- [3] A. Annovi et. al. - “A new Variable Resolution Associative Memory for High Energy Physics” - ATL-UPGRADE-PROC-2011-004 (2011)
- [4] S. Viret et. al. - “Emulation of a track reconstruction system based on associative memories”, CMS Detector Note, DN-2015-025

Conclusion and Scope

A search for the SM Higgs boson has been carried out, using 7, 8 & 13 TeV data collected by the CMS detector, in the associated production mode where the Higgs boson is produced along with a W boson and decays to a pair of τ leptons, and W boson decays to a highly energetic μ . Two different analyses are performed,

- $WH \rightarrow \mu\tau_h\tau_h$: In this channel the associated W boson decays to a μ and both the τ leptons from the Higgs boson decay hadronically (τ_h), giving rise to one μ and two opposite sign τ_h in the final state. The Higgs mass is reconstructed by the two τ_h candidates. This analysis is performed using data corresponding to integrated luminosity of 5, 19.5 and 2.1 fb^{-1} at $\sqrt{s} = 7, 8$ and 13 TeV proton-proton collisions respectively. The final state is dominated by mis-identified or fake

background events. A novel data-driven fake rate technique has been developed and fake background is estimated by a $Jet \rightarrow \tau_h$ fake rate method. No excess in event yield has been observed over the predicted background and a confidence limit is set on the SM Higgs cross section. The expected limit at $125 \text{ GeV}/c^2$ for the combined 7 & 8 TeV analyses is $12 \times \text{SM}$. Evidently, more data is needed to increase sensitivity of the channel. The observed limit is compatible both with SM Higgs and background only (no Higgs) hypotheses. At $\sqrt{s} = 13 \text{ TeV}$, the cross section of the WH process should increase by a factor of ~ 1.8 with respect to $\sqrt{s} = 7 \text{ TeV}$ and the expected limit at $125 \text{ GeV}/c^2$ extracted from 2.1 fb^{-1} data at 13 TeV is roughly equivalent to the 7 TeV results.

- $WH \rightarrow \mu\mu\tau_h$: In this channel, one of the τ leptons from the $H \rightarrow \tau\tau$ mode decays to a μ . Though $H \rightarrow \tau\tau \rightarrow \mu\tau_h$ branching ratio is much smaller than that of $H \rightarrow \tau\tau \rightarrow \tau_h\tau_h$, the presence of two muons in the final state increases the event yield since reconstruction efficiency of μ in CMS is much higher than τ_h . The visible mass of the Higgs boson is reconstructed by the sub-leading μ and the τ_h candidate in the final state. This analysis has been performed using the 2.1 fb^{-1} integrated luminosity at $\sqrt{s} = 13 \text{ TeV}$. Like the other analyses discussed above, the final state is dominated by fake background events which is estimated using a $Jet \rightarrow \mu$ data-driven fake rate technique. It was a natural choice to extend the analysis in this semi-leptonic channel to improve the overall sensitivity and coverage of the search. The expected limit at $125 \text{ GeV}/c^2$ is $\sim 20 \times \text{SM}$ for $\sqrt{s} = 13 \text{ TeV}$ data, which is very similar to what has been seen using the 5.0 fb^{-1} of $\sqrt{s} = 7 \text{ TeV}$ data. Clearly, more data is needed to improve sensitivity of the channel.

Both the analysis channels are dominated by fake background events in the final state, where one or more particles are mis-identified as real particle. The data-driven

fake estimation technique developed for the analyses complements each other. In the process of performing the analyses, several other studies like measuring the muon trigger, identification and isolation efficiencies are performed. Studies have also been performed on tau isolation to mitigate the pile-up effect using Monte Carlo events of different pile-up and bunch crossing scenarios. With more data, it is expected to show some hint of the SM Higgs particle to establish the fermionic coupling in associated production mode. In future dedicated studies can be performed to identify the property of the boson and its resemblance with the SM Higgs.

CMS is also preparing for several upgrades to meet its physics goals for future LHC running. The LHC is scheduled for a luminosity upgrade (High Luminosity LHC, HL-LHC) during 2022 and expected to deliver an instantaneous luminosity of $5 \times 10^{34} \text{ cm}^{-2} \text{ s}^{-1}$ which is ~ 5 times higher than the current value. To meet the challenges posed by the HL-LHC, several sub-detector components of the CMS detector will be upgraded. In this context, a trigger algorithm for electrons has been designed including the tracker information at Level-1 to reduce the enormous event rate expected during HL-LHC. This will enable CMS to retain similar physics performance at the low mass range even at the high luminosity environment. The analysis has been carried out in two different ways, by using the stub information and tracklet based track information. Once the matched object is found a L1Track based isolation variable is exploited, which performs way better than a L1Calo based isolation. The results obtained justify the usefulness of a L1 Track Trigger for electron and are described in the **Phase II Technical Proposal**. Performance of the algorithm has also been studied for couple of other outer tracker geometries which are a modified version of the proposed baseline design.

This study can be further extended by exploiting the crystal level calorimeter object which promises a finer position resolution to understand whether it is possible to achieve

a better performance than the tower level object. It is also possible to carry out the analysis using tracks reconstructed by some other methods that are available now.

The thesis also presents a study of track reconstruction at Level 1 using the Associative Memory based pattern recognition. AM-based tracking is expected to play a major role for the Phase-II upgrade of the CMS detector. An emulation of a Principal Component Analysis induced track fitting algorithm has been performed for floating and fixed point representations. The response of the fitter does not degrade for integer based fixed point representation which is supposed to be implemented on FPGA hardware.